Laser-assisted spectroscopy of Au and Na isotopes at ISOLDE

Robert Dale Harding

Doctor of Philosophy

University of York

Physics

August 2019

Abstract

Lasers are a powerful spectroscopic tool that have been exploited for decades to elucidate information about nuclear structure. Presented in this work are two different complementary laser interaction studies. The first is a combined laser spectroscopy and α-decay study of odd-odd isotopes ^{180,182}Au, while the second highlights the recent developments at ISOLDE's new laser polarisation beamline, culminating in the most precise deduction of the magnetic moments of $^{26-31}$Na to date.

The investigation of laser-ionized odd-odd isotopes ^{180,182}Au was performed using the Resonant Ionisation Laser Ion Source, Windmill and ISOLTRAP Multi-Reflection Time-of-Flight Mass Spectrometer. A complex fine structure α-decay pattern of ^{180}Au was deduced providing an insight into the low-lying levels in the daughter nucleus ^{176}Ir. The α-decay branching ratio of $b_{\alpha}(^{180}$Au$) = 0.58(10)$ % has also been derived, permitting calculation of the reduced α-decay widths and determining the degree of hindrance of respective α-decay branches. From complementary measurements of the hyperfine structure, magnetic moments of $\mu_I(^{180}$Au$) = $ -0.83(7) μ_N and $\mu_I(^{182}$Au$) = $ +1.68(5) μ_N were deduced. Based on the observed hyperfine structure pattern, a preferred ground state spin $I(^{180}$Au$^g) = (1^+)$ is proposed, and the assignment of $I(^{182}$Au$^g) = 2^+$ in this work, is consistent with previous studies.

The magnetic moment of ^{26}Na, has been determined for the first time with parts-per-million precision, which is a hundred-fold improvement over the usual precision achievable for such short-lived nuclei. This achievement was possible by applying the ultrasensitive β-detected Nuclear Magnetic Resonance technique to a liquid-state sample at the laser polarization beamline. This result, combined with data from the literature, has further improved the uncertainty of the magnetic moments of $^{27-31}$Na to the dozen ppm level. Extending this approach to other isotopic chains would enlarge the palette of β-NMR nuclei to a variety of new isotopes across the nuclear chart.

Contents

List of Figures

List of Tables

Acknowledgements

There are many, many people who I have had the privilege to work, study and hangout with in my journey to complete this PhD. Although I'm in debt to all of you, there are some people who deserve a special mention.

To start with I want to express my insurmountable gratitude to my supervisors Andrei and Magda. Andrei, for your patience, guidance and for giving me the opportunity to travel to so many parts of the world through conferences and graduate schools. Your work ethic and apparent immunity to jet lag in order to respond to my emails wherever you are in the world, has been inspiring and supportive throughout this whole experience. Magda, for giving me so much responsibility and creative freedom to use my ideas to improve VITO for the many future experiments to come! Without you I would never have had the opportunity to spend almost my entire PhD in Geneva, which has done so much to expand my professional and personal horizons in ways I never imagined.

I want to thank the VITO local group, in particular Wouter who not only proof read part of this work for me but has been invaluable with his advice, puns and times in the lab where we literally bent and broke the beamline into shape. Frank for showing me so many different practical skills, and being a great first postdoc. I hope you use the new English slang I taught you responsibly in the future! Lina, for all your positivity and willingness to get things done. Abhi and Phil for being the greatest masters students we could of hoped for, I learned as much from teaching you as (hopefully) you guys did from me. Jared, for possibly being the most kind and reliable person at ISOLDE, I wish you the best of luck in the future. Mark, whom I shared many nightshifts with beamtuning, for giving up so much of your time to make VITO the great success that it is. Victoria, Freddy, Tassos, Kasia and Karolina for all of your help with our experiments.

In the wider ISOLDE community I would like thank Shane, Cory, Adam, Chris, Greg for great times we've had working and relaxing together. Tom for being truly fantastic first

Back home in England, Charles, Emily, Will(s) and Kirstie for being great friends when I've sporadically come back to visit and for coming out to see me in Geneva (even though you were all dying of flu). Elliot, for being a rock in the storm that is my life. Em, Mel, Kieran, Joe and Conor for continuing to make Guildford home for me.

And finally I would like to thank my family. My parents Moira and Ian for their unconditional support and providing the PhD essentials like coffee, food and roof over my head during the end of my PhD, so that I could worry about the physics. My brother Jamie and sister Nicola for travelling around Switzerland with me, and for being supportive throughout. Last but not least, both of my dogs Samson and Sophie for their lifelong emotional support.

I fear there are many names I haven't managed to mention here and for that I apologise. Thank you everyone for your support, this has been a long and difficult journey but also, undeniable fun!

RDH

Declaration of Authorship

I declare that this thesis is a presentation of original work and I am the sole author. This work has not previously been presented for an award at this, or any other, University. All sources are acknowledged as References.

1 Introduction

Understanding the structure evolution of the ground and isomeric states of nuclei very far from stability is one of the challenges faced by current experimental and theoretical efforts. Historically, the neutron-deficient lead region has been one of the richest playgrounds for a variety of nuclear structure phenomena, the shape coexistence and presence of deformed intruder states at low excitation energies being just some of the examples [1, 2, 3, 4, 5, 6, 7, 8]. Since the pivotal 1972 discovery of shape staggering and abrupt changes in the ground-state mean-square charge radii ($\delta\langle r^2 \rangle$) of the light mercury isotopes [9, 10, 11, 12], extensive experimental charge radii data collected in this region provide vital benchmarks for testing the predictive power of various theoretical approaches, see some of the recent examples in [13, 14, 8].

Laser spectroscopy has proven itself a powerful tool with which to investigate the properties of ground and isomeric states of long chains of isotopes in this region. The value of the information elucidated cannot be understated, where from studying an isotopes hyperfine structure, it is possible to measure the nuclear spin (I), magnetic moment (μ_I), the spectroscopic quadrupole moment (Q_s), $\delta\langle r^2 \rangle$ and the nuclear quadrupole deformation (β_2). Furthermore, α, β and γ-ray decay spectroscopy studies performed in parallel can provide a wealth of information about the excited states in nuclei and further insight into the complicated competing nuclear configurations.

Measurements of an isotopes hyperfine structure and the nuclear properties derived from it, are influenced by the Bohr-Weisskopf (BW) effect. The effect is caused by the

finite distribution of magnetic currents within a nucleus of finite size, leading to the so called hyperfine anomaly [15]. The effect is small in light nuclei, but can reach several % in heavier ones $\approx$ Z = 80 [16], limiting the precision of magnetic moments. Laser-polarised β-NMR provides a more precise, independent way of measuring nuclear g_I factors which, when combined with conventional laser spectroscopy, can provide an accurate determination of the BW effect. In addition, it can assist in the sensitive determination of both magnetic moments and electric quadrupole moments, devoid of the influence from the BW effect.

The benefit of laser-polarised β-NMR as a complementary tool to conventional laser spectroscopy is evident. Furthermore, the development of a dedicated beamline for polarising nuclei with lasers, opens up further opportunities to incorporate laser-polarised β-NMR, among other techniques coupled with a polarised nuclear species, into multi-disciplinary fields such as biochemistry and material sciences [17, 18, 19, 20, 21]. In this thesis, the results from a combined laser and α-decay spectroscopy study of neutron deficient ^{180,182}Au are presented in Sec. 5, highlighting the benefit of interplaying two different spectroscopy techniques to elucidate information about nuclear structure. In Sec. 6 the results from the recent developments at the new laser polarisation beamline, referred to in this text as VITO (Versatile Ion-polarised Techniques Online) at ISOLDE are shown, along with the most precise derivation of the magnetic moments of the $^{26-31}$Na to date. This displays the potential of using the laser-polarised β-NMR technique as a complementary tool for future investigations into deformed nuclei.

1.1 Previous investigations of the neutron deficient gold isotopes

Since the early 1980's, the neutron-deficient gold isotopes ($Z =79$) have played an important role in studies of shape coexistence in the neutron-deficient lead region, by demonstrating further examples of abrupt changes in the ground-state mean-square charge radii [22, 23, 24, 25]. In particular based on isotope shift measurements, a sudden change to strongly deformed shapes was observed for the ground states of $^{183\text{-}186}$Au (N=104-106), in respect of weakly-deformed ^{187}Au and heavier gold isotopes, see Fig. 1.1. The quadrupole moment measurements of the long-lived ground and isomeric states in ^{184}Au, being the lightest gold isotope for which the quadrupole moment was measured so far, provided direct evidence of their prolate deformation [26]. This deformation jump was interpreted as being due to the change from the spherical $\pi 3s_{1/2}/\pi 2d_{3/2}$ orbitals responsible for the ground states of the heavier isotopes, to prolate deformed $\pi 3/2^-[532]$ and/or $\pi 1/2^-[541]$ Nilsson states of the $h_{9/2}$ parentage by approaching the mid-shell at N=104 [27, 26, 28].

The ground state properties and low energy excitation scheme of the odd-odd Au nucleus ^{182}Au, has previously been investigated via low temperature orientation [30] and by a β^+/EC experiment at ISOLDE [31]. In the first study, ^{182}Hg nuclei were implanted into iron foils, soldered onto a low temperature cold finger. The foil, cooled to mK temperatures, polarises the implanted nuclei. γ-ray anisotropy was observed as function of time, from which the nuclear g factor was be extracted based on an assumption of the nuclear spin (see Tab. 3 in [30]). The initial results preferred a $I = 3$ assignment, with $\mu(^{182}\text{Au}) = 1.65(15)\mu_N$, although they did not rule out the possibility of $I = 2, 4$ assignment. The latter study investigated the low energy excitation structure through γ-γ and β-γ coincidence measurements from the β decay of ^{182}Hg. Their results proposed the ground state was likely $I = 2^+$, with a suggested configuration of $\pi 3/2^-[532] (\pi h9/2) \otimes \nu 1/2^-[521]$.
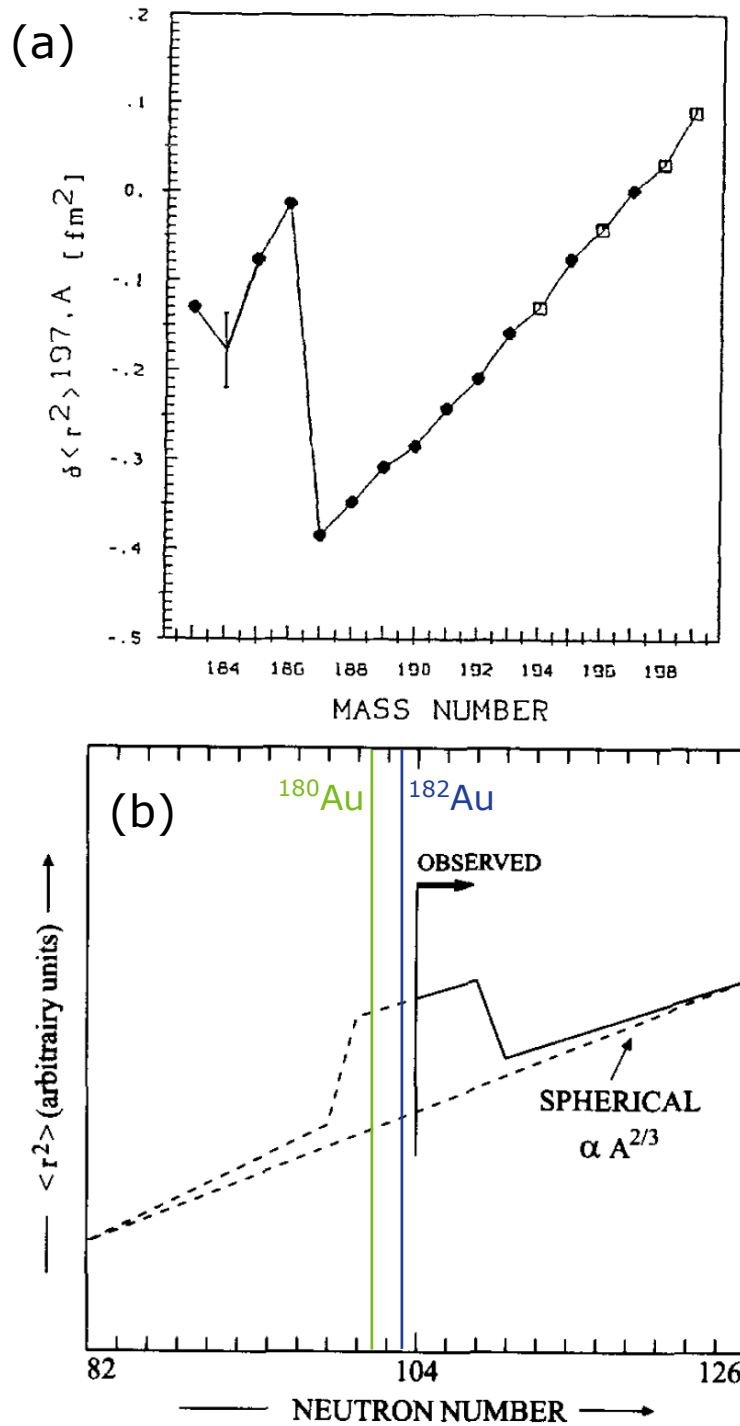
FIGURE 1.1: Previous studies of the $\delta\langle r^2 \rangle$ in the Au isotopic chain. (a) The previously published experimental data, image taken from [24]. (b) predicted behaviour of the gold charge radii, image taken from [29].

Previous investigations of ^{180}Au have been more limited. The low energy excitation structure has been probed via α-decay from ^{184}Tl [32] and the α decay of ^{180}Au has also been studied to a limited degree [33, 34]. As shown in [32], all α decay from ^{184}Tl are hindered, indicating a different underlying structure between the mother and daughter nuclei. The results from a fusion evaporation experiment [33], only deduced a single α-decay line for ^{180}Au. An α decay branching ratio was also derived, although the formula used to calculate the ratio was deemed to be incorrect from a private communication with the authors of the study. The results from [34] improved on the previous study, indicating the presence of at least seven α-decay lines from ^{180}Au, but only three α decays were placed directly into a partial decay scheme (see Fig. 10 in [34]). However, no evidence of the single α-decay line from [33] was observed. The study also proposed that none of these α decays directly fed the ground state in ^{176}Ir.

Following the advances in the decay-tagged in-source laser spectroscopy technique [35], a dedicated campaign to measure the ground and isomeric state properties of the neutron-deficient gold isotopes has been recently undertaken by our collaboration at the CERN-ISOLDE facility. This two-pronged experimental approach could provide a wealth of information. On the one hand, the magnetic dipole and electric quadrupole moments of nuclei, and changes in the mean-squared charge radii may be extracted from measurements of hyperfine structure (hfs) and isotope shifts (IS). On the other hand, the evolution of nuclear structure may be tracked by observing the α- and β-decay properties, which provides further information on the underlying configurations. Together, these two complementary techniques deliver a comprehensive method for studying the properties of ground and isomeric states. The first results from this campaign have been presented in [36], where spins and magnetic moments of the ground states in ^{177,179}Au were deduced for the first time. In Sec. 5 the results from a combined α-decay and laser spectroscopy study of odd-odd isotopes ^{180,182}Au (N=101,103) is presented, which are located at the expected end of the region of large ground-state deformation in the neutron-deficient gold nuclei, see Fig. 1.1.

1.2 Motivation for the development of a new laser polarisation beamline

The knowledge of magnetic dipole moments of atomic nuclei is a crucial ingredient to understand the nuclear force binding protons and neutrons together. In particular, their sensitivity to the single-particle nature of valence nucleons [37, 38] provides insight into the mechanisms behind the nuclear structure phenomena emerging in unstable nuclei. To these belongs the formation of "halo" structures in light nuclei, [39, 40] or the disappearance of canonical shell closures for neutrons/protons [41] and appearance of new closures [42], manifested by new "magic" numbers.

Furthermore, precise nuclear magnetic moments are very important for the analysis of local electronic, atomic and molecular environments investigated via Nuclear Magnetic Resonance (NMR). In NMR the resonance frequency is proportional to the product of the magnetic moment of the nucleus and the external magnetic field. However, the electrons of neighbouring atoms shield the nucleus, adding a perturbation to the external magnetic field as seen by the nuclear ensemble. This effect is on the order of parts-per-million (ppm), and thus to distinguish between different electronic environments (e.g. revealing the location of an atom within a molecule) the magnetic moment of the nucleus inside the atom of interest should be known with a similar precision. Whilst the magnetic moments of most stable and many long-lived nuclei are known to within a ppm [43], this is not yet the case for short-lived ones. Achieving such precision for short-lived nuclei has become important in light of recent worldwide efforts to perform the first biochemical studies with ultra-sensitive β-detected NMR (β-NMR) [44, 45, 46, 47]. This approach offers an increase in NMR sensitivity of up to ten orders of magnitude, due to the gain in nuclear spin polarization (close to 100%) and the observation of resonances in the asymmetry of β decay from short-lived probe nuclei [17].

β-NMR addresses the largest limitation of conventional NMR, namely the low sensitivity, which is of particular relevance when recording signals from metal ions. Nuclei of many metals give very weak NMR signals due to their small concentration within biological samples and often unfavourable NMR properties (small magnetic moment, spin $> 1/2$ and large quadrupole moment). However, the ultra-high sensitivity of β-NMR can provide insight into many new topics within chemistry and biology. For example, β-NMR on sodium and potassium can help investigate the formation and stability of G-quadruplex DNA structures [45], see Fig. 1.2. Furthermore, β-NMR on zinc, one of the most difficult elements to study with conventional NMR, would open up new research avenues to investigate its interaction with many metalloproteins [48]. But for this research to be possible, the magnetic moments of the probe nuclei used in these studies have to be known with ppm precision, an improvement of two to three orders of magnitude on current measurements.
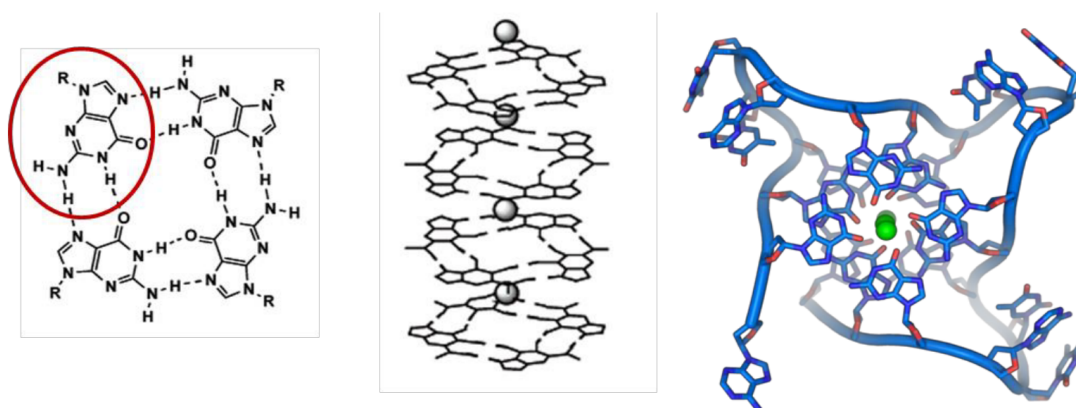
FIGURE 1.2: Schematic of a G-quadruplex. Left: top view of 4 guanine bases forming a G-quadruplex. Middle: side view of alkali-metal cations bound inside G-quadruplex channels. Right: top view of cations interacting with guanine bases with DNA backbone around them. Image taken from [45].

One of the two main techniques used to determine the magnetic moments of radioactive nuclei is the high-resolution optical spectroscopy [49, 50, 51], which leads to a relative precision around 10^{-3}. It relies on the interaction between nuclear moments and the electromagnetic fields produced by atomic electrons and is reflected in the hyperfine structure of a selected atomic transition. The resulting precision is determined by the size of the hyperfine splitting and width of the resonances, as well as by the small corrections due to the BW effect and electric charge inside the nucleus (Breit–Crawford–Rosenthal–Schawlow effect), see [15] and the references therein.

The other approach relies on the detection of β particles or γ rays emitted anisotropically by radioactive nuclei placed inside an external magnetic field. One such technique is β-detected NMR, which takes advantage of the asymmetry in the emission of β particles along and against the nuclear spin direction and the decrease in asymmetry when a nuclear magnetic resonance takes place.

Previously, β-NMR studies have only been performed in solid-state host materials, due to their compatibility with the vacuum environment of radioactive-ion beam facilities. However, the relative widths of β-NMR resonances from such samples are in the 10^{-4} range, which limits the precision of measured magnetic moments to a similar order of magnitude. To be competitive with conventional NMR, the precision should be at least at the ppm level. In Sec. 6, the first magnetic moments of several short-lived isotopes of sodium are determined with ppm precision, by means of β-NMR in a liquid-state host. This novel approach could be extended further to isotopes of different chemical elements, widening the palette of nuclei available for β-NMR studies in biochemistry.

2 Fundamental Nuclear Structure

2.1 Nuclear Models

This chapter introduces the spherical liquid drop model, the nuclear shell model, nuclear deformation and the Nilsson model. It is then followed by a brief introduction to the experimental properties observed in α-decay and γ-ray spectroscopy.

2.1.1 The spherical Liquid drop model

The Liquid Drop Model (LDM) is a macroscopic approach to describe properties of the nucleus. The model treats the nucleus as an incompressible, spherical drop of high density nuclear fluid with a radius described by:

$$R_{sph} = R_0 A^{\frac{1}{3}} \tag{2.1}$$

where A is the total number of nucleons and R_0 is ≈ 1.2 fm, determined from electron scattering experiments [52]. The LDM led to the development of the semi-empirical expression for binding energy (BE):

$$BE = a_v A - a_s A^{\frac{2}{3}} - a_c \frac{Z(Z-1)}{A^{\frac{1}{3}}} - a_{sym} \frac{(A-2Z)^2}{A} + \delta(A,Z) \tag{2.2}$$

where Z is the number of protons, N is the number of neutrons and A is the mass number ($A = Z + N$). The formula encompasses five terms; the first term is the volume term, accounting for the binding energy as a result of the nuclear force, the attractive interaction between nucleons that binds them together. The second is the surface term, reducing the binding energy due to nucleons at the nuclear surface being in contact with fewer nucleons than those in the interior of the nucleus. The third term, the Coulomb term, reduces the binding energy due to the repulsive nature of the electrostatic interaction between protons. The fourth term is the symmetry term, reflecting the effect of the Pauli exclusion principle. Within the nucleus, no two identical fermions can occupy the same state. Therefore, nuclei with a large imbalance between protons and neutrons become less energetically favourable, reducing the binding energy. The final term, called the pairing term, relates to the gain in binding energy from the pairing of alike nucleons. The term is frequently expressed as $\delta(A,Z) = a_P A^{-3/4}$ where a_P is 0 for odd A nuclei, negative for odd-odd nuclei and positive for even-even nuclei. The five parameters are extracted from the fitting of experimental data.

While this model is extremely successful in its description of the global trends of nuclear binding energies, it fails to to account for the diffuse surface of the nucleus. The droplet model (DM) is a further modification off the LDM, which includes separate density distributions for protons and neutrons [53]. This variation in nuclear density allows features such as surface diffuseness instead of the sharp cutoff at the nuclear surface as described by the LDM. From the DM, further bulk nuclear properties can be predicted such as the isotope shift between elements and charge radii of a nucleus. Being empirical models, both the LDM and DM do not account for the shell-effect properties observed in nuclei. The latter is done in the so-called "shell model".

2.1.2   The spherical shell model

The shell model attempts to describe the shell-like structure observed in nuclei. Shell closures appears at the so-called "magic" numbers of protons and neutrons of 2, 8, 20, 28, 50, 82 and 126 for neutrons. The shell-like behaviour is evident from the acute decrease in proton and neutron separation energies in nuclei with a single nucleon outside a closed shell. Furthermore, the energies of the first excited state in magic nuclei are prominently larger than those of non-magic nuclei.

The underlying assumption of the shell model is that the nucleons move in spherical central potential, generated by the nucleons themselves. The choice of the potential is crucial as it defines the relative spacing of the nuclear levels. As a first approximation, the infinite spherical well is a suitable candidate for a potential. Here, the degeneracy of each level with orbital angular momentum l (the number of nucleons that can be placed into each level) is $2(2l + 1)$. This accurately reproduces the first magic numbers 2, 8 and 20, but fails to predict the larger numbers. However, the infinite spherical well potential does not accurately reflect the expected shape of the nuclear potential, as it has a sharp edge at the boundary of the potential and requires an infinite amount of energy to remove a nucleon from the nucleus.

Another potential that would seem a suitable candidate is the 3-dimensional simple harmonic oscillator. Here, the energy eigenvalues can be written as $E_{nl} = (2n + l - 1/2)\hbar w$, where the lowest value of $n = 1$. The degeneracy of these states is characterized by $\Delta l = -2\Delta n$, thus for example, the energies of particles in the 2s and 1d orbits are degenerate. However, a simple harmonic oscillator doesn't quite reflect the behaviour of the nuclear potential, in that the potential increases in strength with a particles radial distance from the centre. A more realistic potential takes the form of a Woods-Saxon:

$$V_C(r) = \frac{-V_0}{1 + exp(\frac{r - r_{sph}}{a})} \qquad (2.3)$$
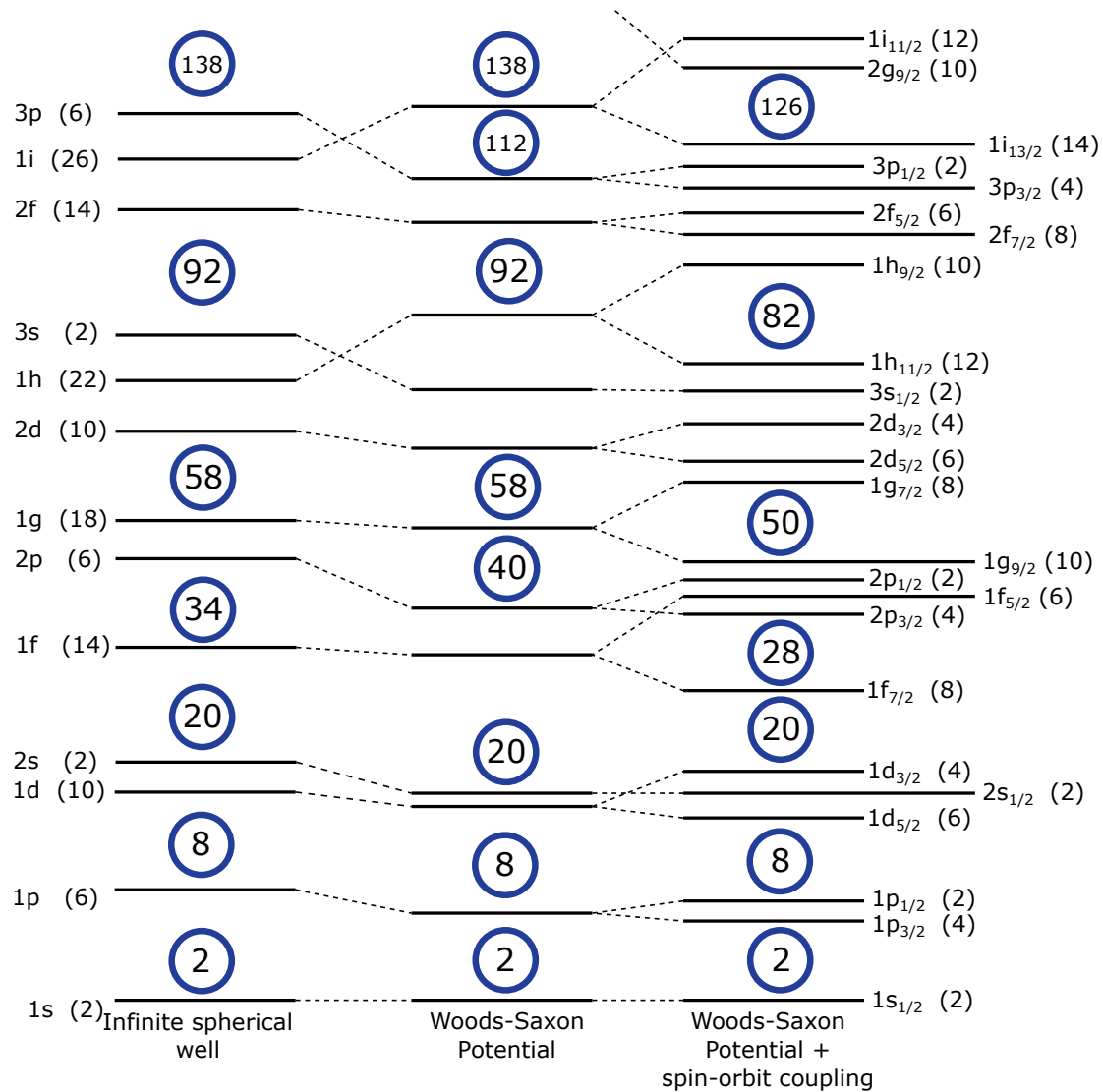
FIGURE 2.1: Left: The energy levels of an infinite square well potential. Centre: The energy levels calculated using a Woods-Saxon potential. Right: Woods-Saxon potential with a spin-orbit term, reproducing the observed magic numbers.

where $V_0 \approx 50$ MeV, r_{sph} is the radius of the nucleus as given in Eqn. 2.1, a is the thickness of the nuclear skin and r is the radial distance from the centre of the nucleus. The resulting energy levels are shown alongside those of the infinite square well in Fig. 2.1, and is seen to remove the l degeneracy of major shells. However, the magic numbers above 20 do not yet emerge.

In order to fully reproduce the nuclear shell structure, the spin-orbit interaction needs be included as first proposed by Mayer, Haxel, Suess and Jensen [54]. This term takes the form:

$$V_{so}(r) = V_{ls}(l \cdot s) r_0^2 \frac{1}{r} \frac{dV_C(r)}{dr} \tag{2.4}$$

where V_{ls} is the strength of the interaction, $s = \frac{1}{2}$ is the intrinsic spin of a nucleon and r is the distance from the centre of the potential. The interaction causes each state with $l > 0$ to split, each labelled with a new quantum number j, where $j = l \pm s$. States with $j = l + s$ decrease in energy relative to the unperturbed l level while the opposite occurs for states with $j = l - s$. The separation between the split states increases with l, and each energy level is denoted by nl_j, see Fig 2.1. These shifts reorder the nuclear levels, reproducing the observed magic numbers. The shell model possesses great predictive power, dictating that only a single, unpaired nucleon determines the ground state properties of an odd-A nucleus. As such a valence nucleon that occupies the state nl_j, will precept a nuclear ground state of spin j and parity $(-1)^l$. In odd-odd cases, such as the nuclei discussed in thesis, the ground state properties are a vector sum of the valence proton and neutron j momenta, with the parity given by $(-1)^{(l_1 + l_2)}$.

2.1.3 The deformed shell model

The spherical shell model, while exemplary in its description of closed-shell magic nuclei, fails to accurately reproduce the properties of deformed nuclei (spins, masses and non-zero electric quadrupole moments). The most prevalent form of deformation is quadrupole in nature [53]. The magnitude of quadrupole deformation is described by the quadrupole deformation parameter, β_2, given by:

$$\beta_2 = \frac{4}{3}\sqrt{\frac{\pi}{5}}\frac{\Delta R}{r_{sph}} \tag{2.5}$$

where ΔR is the difference between the two axes of the deformed nucleus, and r_{sph} is as defined in Eqn. 2.1. When β_2 is > 0, the nucleus becomes elongated along the symmetry axis, described as a prolate spheroid. Conversely, when β_2 is < 0 the nucleus is compressed along the symmetry axis to form an oblate spheroid. Fig. 2.2 shows a pictorial description of these geometries.

The deformed shell model, commonly referred to as the Nilsson model [55], is useful at interpreting the ground-state properties of deformed nuclei. The model assumes a quadrupole perpetuation to the shell model's spherical potential. Thus, a nucleon experiences a different potential according to its alignment with the deformed core. The total angular momentum j is no longer a good quantum number, and instead we consider the projection of j onto the symmetry axis, K. This breaks the $2j + 1$ degeneracy of spherical nuclear states.

The Nilsson orbitals are denoted by a new set of quantum numbers, $K^\pi[Nn_z\Lambda]$, where π is the parity of the state, N is the principal quantum number denoting the oscillator shell from which the state originates, n_z is the number of wavefunction nodes along the symmetry axis and Λ is the component of orbital angular momentum along the symmetry axis.

The magnitude and direction of the resulting energy shift of a state is dependent on the
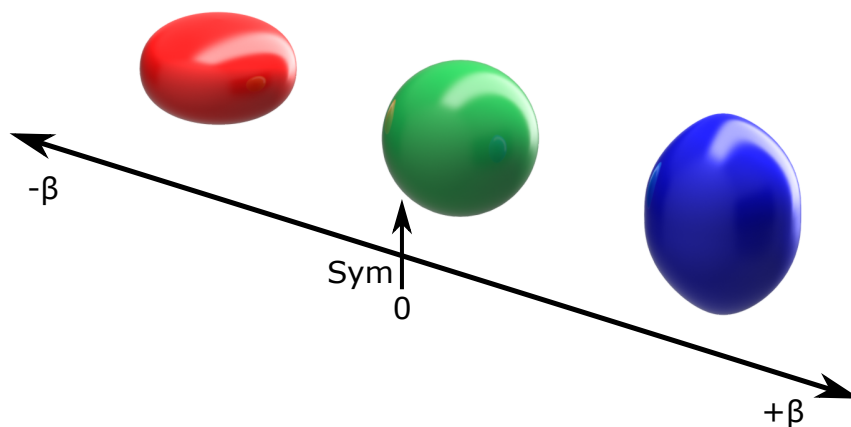
FIGURE 2.2: Schematic representation of spheroidal geometries as a function of the quadrupole deformation parameter, β_2. The symmetry axis is indicated in the vertical plane.

orientation of the orbit relative to the deformed core of the nucleus. Orbits lying closer to the bulk of the nucleus, have an increased overlap with the deformed core, resulting in a stronger interaction. Thus, nucleons that occupy these orbitals will be more tightly bound, reducing the energy of the Nilsson state. Conversely, the opposite is true for particles that occupy states with a reduced overlap with the core which become less tightly bound, resulting in an increase in energy of the Nilsson state.

From these ideas, the Nilsson diagrams for protons and neutrons are constructed, which predict the orbital occupied by valence nucleons in the deformed approach. An example of a diagram relating to gold nuclei presented within this work is shown in Fig. 5.13 in Sec. 5.

2.1.4 Shape Coexistence

Low energy shape coexistence is a phenomenon where distinct, contrasting nuclear shapes appear at similar excitation energies. Shape coexistence occurs from the interplay between two opposing effects: the stabilising effect of closed shells, causing the nucleus to retain a spherical shape, and the residual interaction between protons and neutrons which drives the nucleus to a deformed configuration. Initially thought only to exist in isolated regions of the nuclear chart, the most recent review of the topic proposes its existence in all but the lightest nuclei, see Fig. 8 in [6].

The nuclei in neutron deficient lead region have been shown to exbibit a prolific evidence of shape coexistence. A notable example is the change in the charge radii of neighbouring isotopes of mercury commencing from $A < 186$. Here, the ground states of the even-A isotopes maintain the "normal" weakly-deformed trend, as compared to the strongly deformed $I^{\pi} = 1/2$ ground-state configuration of the odd-A isotopes, see Fig. 1 in [8]. Furthermore, a $13/2^{+}$ isomer in ^{185}Hg adopts a similar weak deformation as the even isotopes, indicating a candidate for shape coexistence.

A similar effect has also been observed in the charge radii of the neutron deficient gold isotopes with $A < 187$. As noted in Sec. 1, at $A = 186$ there is an abrupt change from the weakly oblate trend in the charge radii indicating the onset of strong deformation, see Fig.1.1(a). Unlike the mercury isotopes the gold remains strongly deformed as the neutron number decreases. Our collaboration has now extended data as far as ^{176}Au. These data will be presented elsewhere, while this thesis only deals with the isotopes ^{182,180}Au.

To try to describe the experimental observations, theoretical calculations such as those in the AMEDEE database [56], can provide a valuable insight. Shown in Fig. 2.3 are the results of potential energy surface calculations for $^{180-188}$Au as function of the deformation parameter β_2. These are calculated using the Hartree-Fock-Bogoliubov method based on D1S Gogny effective nucleon-nucleon interaction [56]. This is a self-consistent mean
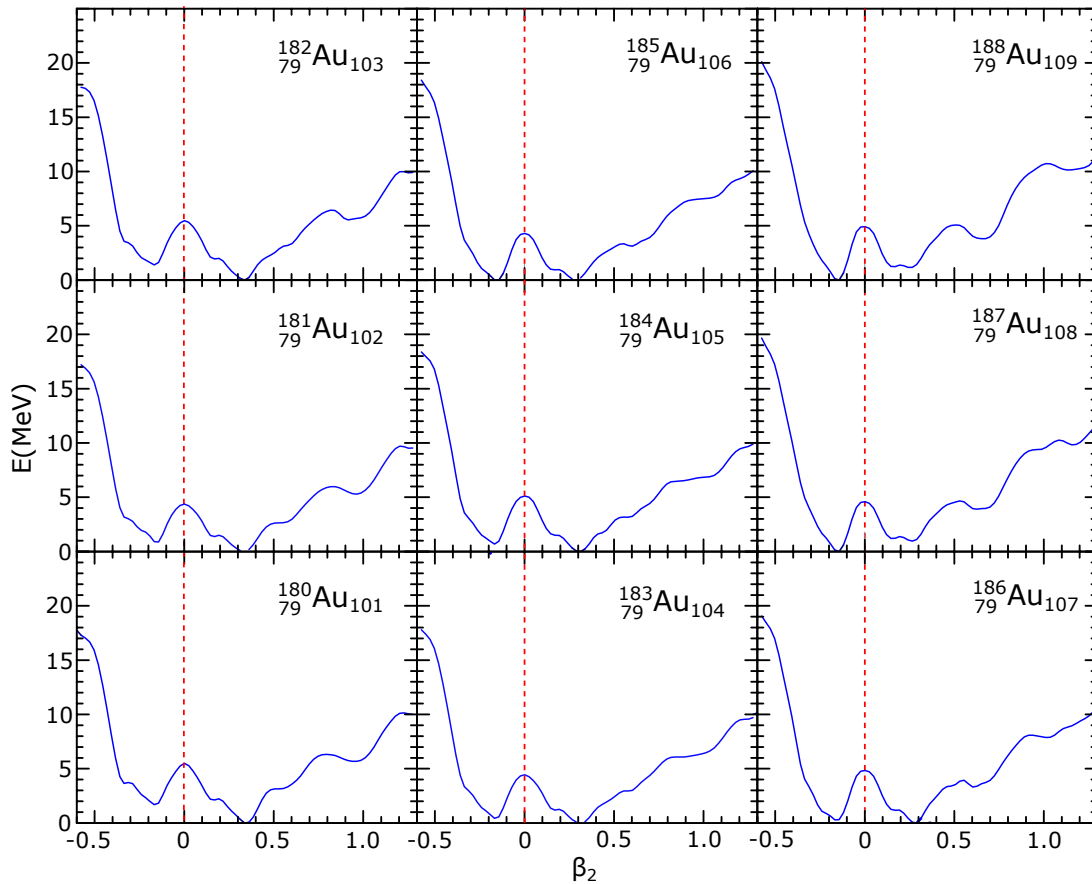
FIGURE 2.3: Potential energy surfaces of the ground states of $^{180-188}$Au as function of quadrupole deformation β_2. Figures are adapted from [56].

field method, using the gogny force which includes terms for a central finite range force, density, zero range spin-orbit interaction and coulomb interaction for neutrons and protons

(more information can be found in [57]). Two competing minima, one with a prolate configuration at $\beta_2 \approx 0.35$ and the other one with an oblate at $\beta_2 \approx$ -0.15 are seen across the isotopic chain. In the heavier isotopes, ^{188,187}Au, the weakly oblate configuration dominates, in contrast to the lighter isotopes where the prolate configuration has the lowest energy. The potential barrier in the middle of this potential energy surface prevents the two states from mixing, resulting in two distinct geometries observed in the experimental data.

2.1.5 Proton intruder states

Intruder states arise from the quadrupole-quadrupole interaction between valence protons and neutrons. The strength of the interaction increases with the number of valence nucleons, and reaches a maximum at the centre point between two magic shells where the number of valence nucleons is greatest. Given a sufficient number of valence protons and neutrons (potentially from particle-hole excitations across a shell closure), the interaction creates deformed intruder states. These intruder states lower in energy with number of neutrons, dominating over spherical shell effects towards the neutron mid shell.

In context of the gold nuclei the systematics of the $1h_{9/2}$, $1h_{11/2}$, $3s_{1/2}$ and $2d_{3/2}$ proton configurations of the odd-A isotopes, are shown in Fig. 2.4. A parabolic trend is observed in the $1h_{9/2}$ intruder configuration becoming the ground state configuration at ^{185}Au, with a minimum centred on the $N = 104$ midshell, halfway between the $N = 126$ and $N = 82$ magic numbers. This lends further evidence for continued strong deformation in the ground states of ^{182,180}Au, likely built on such an intruder state.
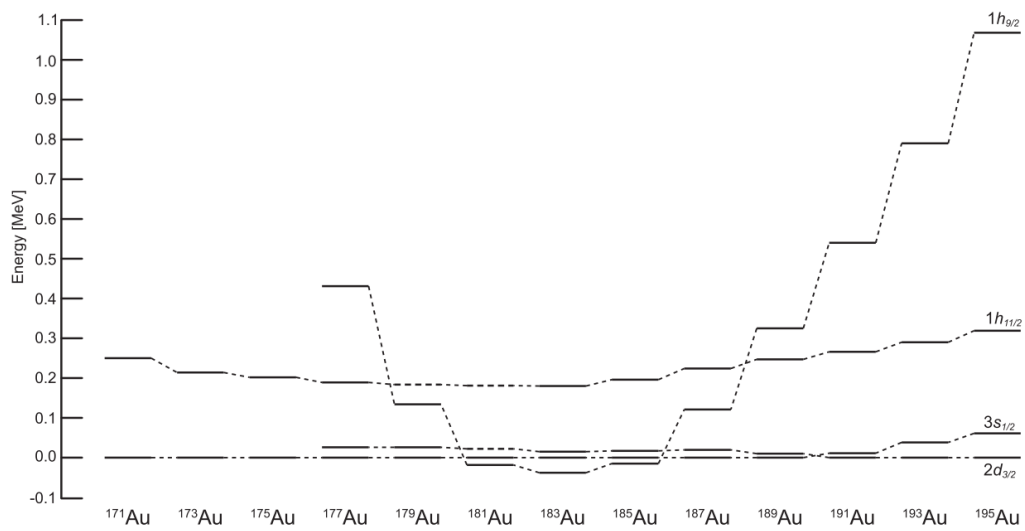
FIGURE 2.4: Systematics of the $3s_{1/2}$, $2d_{3/2}$, $1h_{11/2}$ and $1h_{9/2}$ proton configurations in neutron-deficient odd-Au isotopes, image taken from [58].

2.2   Probing nuclear structure through radioactive decay

2.2.1   Alpha Decay

Alpha decay is a quantum tunnelling process whereby a pre-formed α particle, a tightly bound $^4_2$He nucleus, is moving in an attractive potential well representing the nuclear force, with a width equal to the nuclear radius. At the edge of the nuclear radius exists a potential barrier comprised of a Coulomb and centrifugal term (see B in Fig. 2.5). As the α particle moves within the well it approaches the barrier with frequency v, with a non-zero probability of quantum tunnelling through represented by P. These two factors give rise to the decay constant $\lambda = vP$. Although it has not been shown that α particles are pre-formed within the nucleus, they appear to behave as described above.

Alpha emission is compelled by the repulsive Coulomb interaction between protons, which scales with Z^2, overcoming the nuclear binding interaction that increases with A. As such, the process is prevalent in neutron deficient heavy nuclei where $52 < Z < 117$ and $53 < N < 177$. The α particle is a very stable and tightly bound structure with a large binding energy of 28.3 MeV [59]. Due to its low mass and high binding energy, the particle is energetically favoured for emission by a number of nuclei. The mechanism for α decay is given by:

$$^A_Z X_N \ \rightarrow \ ^{A-4}_{Z-2} X'_{N-2} + \ ^4_2 He \tag{2.6}$$

with the total energy released through the process, known as the Q_α, given by:

$$\begin{aligned} Q_\alpha &= (m_X - m_{X'} - m_\alpha)c^2 \\ &= E_\alpha + E_{X'} \end{aligned} \tag{2.7}$$

Here, m_X is the mass of the parent nucleus, $m_{X'}$ the mass of the daughter and m_α the mass

of the α particle. Alpha decay occurs spontaneously when $Q_\alpha > 0$ and can be expressed in terms of kinetic energy where, E_α and $E_{X'}$ are the kinetic energies of the α particle and daughter nucleus, respectively. The energy released by the process is shared between the recoiling daughter nucleus and the α particle, thus the relationship between Q_α and the kinetic energy of the α particle can be expressed as:

$$
\begin{aligned}
Q_\alpha &= E_\alpha \left(\frac{m_X}{m_{X'}} \right) \\
&= E_\alpha \left(\frac{A}{A-4} \right)
\end{aligned}
\tag{2.8}
$$

where A is the mass number of the parent nucleus. The tunnelling process of α decay has a strong Q_α dependence, leading to a preference of population of low energy excited states or ground state in the daughter nucleus. Excited states in the daughter nucleus can be populated via α decay, referred to as fine structure (f.s.) α decay. Observations of f.s. α decay can reveal a wealth of information about the low energy excitation structure, such as the energies and parities of excited states. Frequently f.s. α decay is followed by the emission of prompt γ rays, which when measured can help in building a detailed spectroscopic picture of the nucleus.

The angular momentum of the emitted α particle, L_α, ranges from $|I_i - I_f|$ to $|I_i + I_f|$, when a nucleus decays from an initial state with angular momentum I_i to a final state of I_f. The total spin of a $^4_2$He nucleus is 0, so only orbital angular momentum is carried away by the emitted particle. The parity change associated with α decay is $(-1)^{L_\alpha}$, which leads to a selection rule: if there is a parity change between the initial and final states L_α must be odd. Conversely, if the parities of the two states are the same, L_α must be even.

The observables from an α decay experiment consist of E_α, the intensity I_α, branching ratio α and the decay half life $T_{1/2}$. Using the approach as described by Rasmussen in [60] a measure of the α particle formation probability within a nucleus, referred to as the
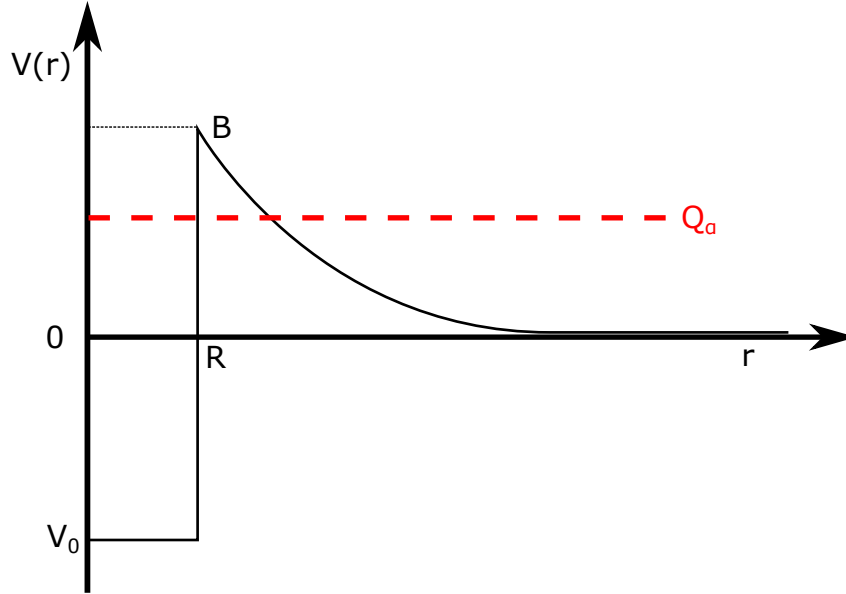
FIGURE 2.5: A schematic of an α particle in a one-dimensional square well potential, tunnelling through a potential barrier that is the sum of a Coulomb and centrifugal term.

reduced α-decay-width (δ_α^2), of a specific α-decay branch can be calculated by:

$$\delta_\alpha^2 = \frac{hln(2)I_\alpha b_\alpha}{T_{1/2}100P} \tag{2.9}$$

where h is Plancks constant, P is the penetration through a potential barrier composed of Coloumb and centrifugal terms and δ_α^2 is usually expressed in keV. The δ_α^2 is extremely sensitive to changes in spin/parity between the initial and final states belonging of the α decay process and is therefore a useful tool to evaluate the structure of excited states in daughter nuclei within the heavy region of the nuclear chart.

To compare the relative hindrance of different α decays, one defines the hindrance factor (HF_α):

$$HF_\alpha = \frac{\delta_{\alpha 1}^2}{\delta_{\alpha 2}^2} \qquad (2.10)$$

where $\delta_{\alpha 1}^2$ belongs to the strongest component of the fine structure or unhindered decay, and $\delta_{\alpha 2}^2$ to that of the α decay under study.

2.2.2 Beta Decay

Beta decay is a three body process by which a nucleus decays via conversion of a nucleon from a neutron (proton) into a proton (neutron). The decay process is described by the following mechanisms:

$$\begin{aligned}
\beta^- &: \; {}^A_Z X_N \rightarrow {}^A_{Z+1} X'_{N-1} + e^- + \bar{v} \\
\beta^+ &: \; {}^A_Z X_N \rightarrow {}^A_{Z-1} X'_{N+1} + e^+ + v \qquad (2.11) \\
\varepsilon &: \; {}^A_Z X_N + e^- \rightarrow {}^A_{Z-1} X'_{N+1} + v
\end{aligned}$$
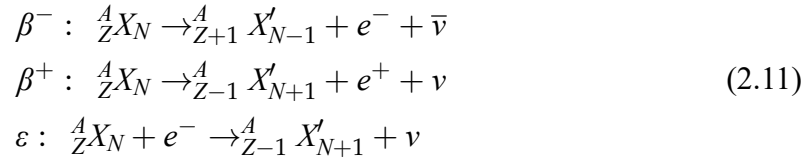
The β^- and β^+ processes involve the emission of an electron (e^-) and an electron anti-neutrino ($\bar{v}$) or a positron (e^+) in conjunction with an electron neutrino (v), respectively. The energies of the emitted β particles have a continuous distribution, due to the energy released in the decay process being shared between the daughter nucleus, β particle and electron neutrino.

Electron capture is a process during which an atomic electron is captured by the nucleus, usually from one of the inner atomic shells due to the increased wave function overlap of these electrons with the nuclear wave function. Following a capture, an electron occupying a higher lying orbital will de-excite to fill the vacancy of the inner atomic shell and emit a characteristic X-ray, with an energy dependent on the initial and final orbits of

the de-exciting electron. Such X-rays are denoted according to the shell from which the captured electron has originated (i.e K, L, M etc.),

A number of spin/parity selection rules also apply to β decay:

$$I_i = I_f + L_\beta + \vec{S_\beta}$$
$$\pi_P = \pi_D(-1)^{L_\beta}$$

(2.12)

where L_β is the change in spin due to the orbital angular momentum carried away by the β particle and electron neutrino and S_β is the coupled intrinsic spin of the neutrino and β particle, a vector quantity. As each of the aforementioned particles are fermions, they possess an intrinsic spin of $S_e = S_v = 1/2$. S_β can be equal to 0 or 1 depending on whether the coupling between the spins of the two particles is antiparallel or parallel.

2.2.3 Gamma Decay

Gamma decay occurs when an excited nucleus decays via emission of a photon, known as a γ ray. Unlike α and β decay, no changes occur to the number of neutrons or protons in the nucleus. Typical γ ray energies range from 0.1 to 10 MeV. The energy of the emitted photon, E_γ is defined as:

$$E_\gamma = E_i - E_f - T_X$$

(2.13)

where $E_{i,f}$ denote the energies of the nucleus' initial and final states, and T_X is the recoil kinetic energy imparted to the nucleus in order to conserve linear momentum. The recoil energy is defined as:

$$T_X = \frac{p_X^2}{2m_X} = \frac{p_\gamma^2}{2m_X} = \frac{E_\gamma^2}{2m_X c^2}$$

(2.14)

where p_X and p_γ are the momenta of recoiling nucleus and γ ray, m_X is the mass of the nucleus and c is the speed of light. One can immediately see that the rest-mass energies of the nuclei are far greater than the energy of a typical γ ray, such that T_X is often negligible.

The photons emitted during γ decay come in two forms, electric (E) and magnetic (M), with a multipole order of 2^L. They also follow a set of spin and parity selection rules:

$$|I_i - I_f| \leq L \leq I_i + I_f$$
$$\pi(ML) = (-1)^{L+1} \quad or \quad \pi(EL) = (-1)^L$$
(2.15)

where L is the angular momentum carried away by the γ ray. Single γ-ray decay is impossible when the spins of the initial and final states are both equal to 0. However transitions between these states, known as E0 transitions, can occur via other processes, such as internal conversion.

2.2.4 Internal Conversion

Internal conversion is an electromagnetic process competing directly with γ decay. A nucleus can de-excite with some probability by ejecting an atomic electron. The total kinetic energy of the electron is equal to the energy of a γ-ray transition, less the binding energy of the shell from which it is emitted. Therefore, unlike the electrons emitted through β decay, conversion electrons have discrete energies:

$$T_e(\Lambda) = E_\gamma - E_B(\Lambda)$$
(2.16)

where $T_e(\Lambda)$ denotes the kinetic energy of the conversion electron, E_γ is the γ-ray transition energy and $E_B(\Lambda)$ denotes the binding energy of the conversion electron shell. Λ indicates the shell of origin of the conversion electron (K,L,M etc.). Therefore internal conversion only occurs when $E_\gamma > E_B(\Lambda)$ and is accompanied by a characteristic x-ray, produced by an outer shell electron de-exciting to fill the vacancy left by the emitted electron.

The multipolarity of an electromagnetic transition can be deduced from an experimentally measured conversion coefficient which can be used to make spin and parity assignments for excited states. By measuring the number of characteristic x-rays or conversion electrons, it is possible to determine the conversion coefficient of electrons from a specific shell, $\alpha_c(\Lambda)$ by:

$$\alpha_c(\Lambda) = \frac{I_{ce}(\Lambda)}{I_\gamma} \tag{2.17}$$

where $I_{\gamma,ce}$ are the intensities of the γ ray and associated conversion electron, respectively. The total conversion coefficient, α_{tot}, is therefore the sum of the conversion coefficients from each electron shell:

$$\alpha_{tot} = \alpha_c(K) + \alpha_c(L) + \alpha_c(M) + ... \tag{2.18}$$

3 Laser Spectroscopy based techniques

In the present chapter, the various methods of measuring a hyperfine structure (hfs) through laser spectroscopy will be described. In addition, the chapter will also provide a description of laser-polarised β-NMR spectroscopy and how this technique can be used to ascertain information about nuclear structure.

3.1 Hyperfine structure

If both the atomic spin, J, and the nuclear spin, I, are greater than zero then an atomic level will split into hyperfine levels (see Fig. 3.6). The coupling of these two spins can be identified by a new quantum number, F, such that:

$$F = I + J \tag{3.1}$$

where F is the total spin of a hyperfine level. Transitions between hyperfine states obey the selection rule $\Delta F = 0, \pm 1$, however transitions between two states where F = 0 is forbidden.

The energy perturbation of a hyperfine level induced by splitting is given by:

$$\Delta E = A\frac{K}{2} + B\frac{3K(K+1) - 4I(I+1)J(J+1)}{8I(2I-1)J(2J-1)} \tag{3.2}$$

where K is given by:

$$K = F(F+1) - I(I+1) - J(J+1) \tag{3.3}$$

and A and B are the hyperfine parameters, defined as:

$$A = \frac{\mu_I B_e(0)}{IJ} \tag{3.4}$$

$$B = eQ_s \left\langle \frac{\delta^2 V_e}{\delta z^2} \right\rangle \tag{3.5}$$

The first term of Eqn. 3.2 accounts for the interaction of the magnetic dipole moment of the nucleus, μ_I, with the magnetic field produced by the electrons at the site of the nucleus, $B_e(0)$. The second term relates to the nuclear spectroscopic quadrupole moment, Q_s, interacting with the average electric field gradient $\left\langle \frac{\delta^2 V_e}{\delta z^2} \right\rangle$ produced by the electrons, which only contributes when both $I, J > 1/2$.

The frequency of a transition between two atomic levels is given by:

$$\gamma = v + \Delta E_u - \Delta E_l \tag{3.6}$$

where v denotes the centroid frequency, equivalent to γ if $I = 0$ and $\Delta E_{u,l}$ is the energy shift due to the hyperfine interaction of the upper state "u" and lower state "l" as described in Eqn. 3.2. The corresponding $A_{u,l}$, $B_{u,l}$ and v can be extracted from a measurement of a hfs using a χ^2 fit. Hence a measurement of a hfs is a powerful technique for extracting information about the structure of the atomic nucleus, (μ_I, Q_s, I) in a chemical-model independent way. Even without $B_e(0)$ and $\left\langle \frac{\delta^2 V_e}{\delta z^2} \right\rangle$, nuclear moments can be calculated based on reference isotopes of the same element with known properties. The following ratios are

obtained:

$$\mu = \mu_{ref} \frac{IA}{I_{ref}A_{ref}} \tag{3.7}$$

$$Q_s = Q_{s,ref} \frac{B}{B_{ref}} \tag{3.8}$$

where the A and B coefficients can come from either the upper or lower hyperfine state.

Equation 3.4 and therefore Eqn. 3.7 both assume a pointlike nucleus. However, a nucleus of finite size will have a distribution of charge and magnetization over the nuclear volume. Electron orbitals with a large overlap with the nucleus are influenced by these distributions, leading to a deviation in the extracted A factor. Two parameters, ε_{BW} and ε_{BR}, were introduced to account for effects of the magnetization and charge distribution. These are known as the Bohr-Weisskopf Hyperfine Anomamly (HFA) [16], and the Breit-Rosenthal (BR) HFA [61], respectively. A modification to Eqn. 3.4 is made to include these effects such that:

$$A = A_{pt}(1 + \varepsilon_{BW})(1 + \varepsilon_{BR}) \tag{3.9}$$

where A_{pt} is the A factor of a point-like nucleus and ε_{BW}, ε_{BR} are HFA corrections as defined above. Both ε_{BW} and ε_{BR} are small compared to unity. One can therefore redefine Eqn. 3.7 as:

$$\mu = \mu_{ref} \frac{IA}{I_{ref}A_{ref}} (1 + \Delta) \tag{3.10}$$

where $\Delta = (\varepsilon_{BW,ref} - \varepsilon_{BW}) + (\varepsilon_{BR,ref} - \varepsilon_{BR})$ and *ref* indicates a reference isotope with a known or negligible HFA. For heavy atoms, ε_{BR} is expected to be negligible compared to the ε_{BW}. Of particular relevance, this has been shown to be the case within the gold isotopic chain [62]. Thus the contribution from ε_{BR} is usually neglected. In general the HFA is on

the order of 1% [63], and if unknown it is treated as a contribution to the error . As the ratio of the A_u / A_l should be constant for all isotopes of a given element, any deviation from this trend can indicate the presence of an appreciable hyperfine anomaly in at least one of the two states [49].

3.2   Laser Spectroscopy techniques

In this thesis, lasers are employed extensively to study nuclear structure via two methods. The first entails using resonant ionisation spectroscopy, performed within ISOLDE's hot cavity ion source, to extract information about the hfs of the ground states of ^{180,182}Au. The process also provides a unique isotope selectivity to assist in decay spectroscopy studies of the above nuclei. The second method exploits lasers in a collinear geometry with an accelerated ion beam, to polarise ^{26,27}Na into desired atomic states. This is used in order to perform β-Nuclear Magnetic Resonance (β-NMR). Both techniques will be described in detail here.

3.2.1   In-source laser spectroscopy

The in-source laser ionisation spectroscopy technique provides a highly efficient and selective method to extract nuclei for study. Laser beams are directed into the ion source, where they interact with the reaction product atomic nuclei produced by the ion source. An atom is ionised through multiple resonant step interactions with the lasers, with the resulting ion extracted by an electric potential. Ionisation occurs after the final step through one of multiple mechanisms, see Fig. 3.1. A valence electron is promoted to a higher lying energy level and subsequently removed by one of three processes: excitation to a Rydberg

level whereby ionisation is achieved through field or collisional ionisation, Fig 3.1(a), non-resonant excitation into the continuum above the ionisation potential, Fig 3.1(b), or resonant excitation to an auto-ionising state, Fig 3.1(c).

For the gold nuclei discussed in this thesis, a three step excitation scheme was used with the final step populating an auto-ionising state [64]. The exact excitation scheme is shown in Fig. 5.10 within Sec. 5.5.
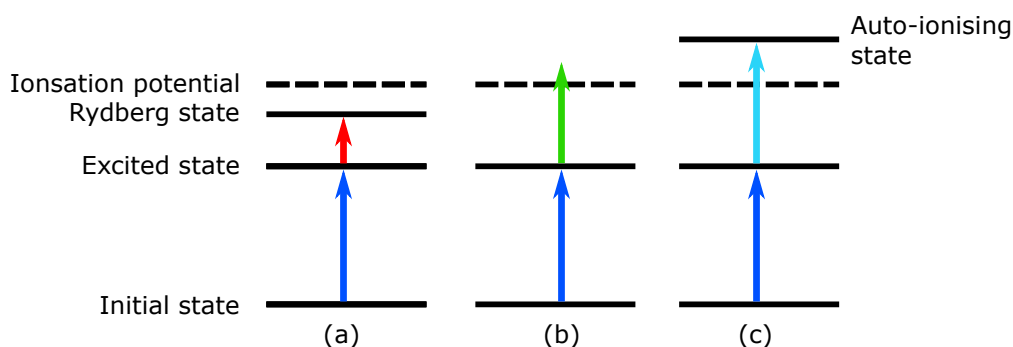
FIGURE 3.1: Schematic of the possible methods of ionisation using the resonance-ionisation process.

As the resonance transitions are unique to each isotope (even each isomer), only the nuclei under investigation are ionised by the lasers, providing the high degree of selectivity. For the decay spectroscopy studies of many nuclei, this can be used to enhance the production of an isotope [65], in some cases by several orders of magnitude. However, this can also be exploited to perform laser spectroscopy on nuclei directly within the ion source. If one of the resonance lasers is scanned over a frequency range, the hfs of the transition can be probed for all isotopes simultaneously. A variety of the techniques exist for tagging the produced nuclei in order to extract the hfs of each isotope, that are discussed in later in this chapter.

The primary drawback of the in-source spectroscopy technique is the limit on the obtainable resolution. By performing spectroscopy on an atomic ensemble inside a hot cavity, there is a significant mass dependent Doppler broadening. Typical hot cavity temperatures are of ≈ 2000 K resulting in line widths ranging from 1-10 GHz. This broadening completely obscures the hfs of medium and light isotopes [66].

However, in heavier nuclei, there is a larger separation of the features within an isotope's hfs and a reduced Doppler broadening due to a larger mass. Therefore, it is possible to obtain hyperfine A factors and isotopes shifts, necessary for charge radii measurements and the deduction of magnetic moments. In some cases it is also possible to extract quadrupole moments from measured B factors, albeit with large uncertainties [8].

3.2.2 Collinear laser spectroscopy

In contrast to in-source laser spectroscopy, collinear laser spectroscopy exploits the reduced Doppler shift achieved by the collinear overlap of the laser with an accelerated ion beam. Since the energy spread, ΔE, of ions extracted from an ISOLDE ion source:

$$\Delta E = \delta \left(\frac{1}{2}mv^2 \right) = mv\delta v \tag{3.11}$$

remains constant under acceleration, an increase in velocity (v) will reduce the longitudinal velocity spread (δv) and therefore the Doppler broadened width. At online facilities, the typical energy spread of produced ion beams is on the order of $\Delta E < 1eV$. At ISOLDE (in the low energy hall) beams can be accelerated up to 60 kV, reducing the Doppler broadened width of hyperfine transitions by 3-4 orders of magnitude, close to the natural linewidth of a hyperfine transition. This is sufficient to perform high resolution laser spectroscopy.

The frequency of the laser beam perceived by the accelerated particles will be Doppler shifted with regards to the frequency measured in the lab-frame v_L by:

$$v = v_l \frac{\sqrt{1 - \beta^2}}{1 \pm \beta} \tag{3.12}$$

where v is the frequency in the rest frame of the accelerated beam, and

$$\beta = \sqrt{1 + \frac{m^2 c^4}{(eV + mc^2)^2}} \approx \sqrt{\frac{2eV}{mc^2} - \frac{3e^2 V^2}{m^2 c^4}} \tag{3.13}$$

where m is the mass of isotope under study and V is the acceleration voltage. The propagation direction of the laser beam relative to the ion beam is indicated by the $\pm$ in Eqn. 3.12, where collinear geometry is $(-)$ and anti-collinear is $(+)$.

Two methods of scanning across a hfs become evident from Eqns. 3.12 and 3.13. In one method, the frequency of the laser can be varied in a set range, as done with in-source laser spectroscopy. Alternatively, the laser is kept at a fixed frequency while the ion beam is Doppler shifted into resonance with the laser by scanning the ions' acceleration voltage and thus their kinetic energy. The second method is beneficial as it is significantly easier to stabilise the laser to a specific frequency, than vary it over a frequency range. To adjust the acceleration voltage, a set of electrodes are placed before the detection region to adjust the velocity of the incoming beam. However, any misalignment of these electrodes with each other or with a non axially aligned ion beam leads to steering or focusing effects in the ion beam, reducing the sensitivity of the experiment.

3.2.3 Detection Methods

Photons

Fluorescence photon detection is the most common technique coupled with collinear laser spectroscopy. When in resonance with the laser beam, the atoms (or ions) are excited from a lower state into an upper (excited) state. Decay from the excited state occurs through the emission of a photon, and their detection is achieved with a photo-multiplier tube (PMT). The hfs is extracted by measuring the photon detection rate as a function of the laser frequency (or scanning voltage).
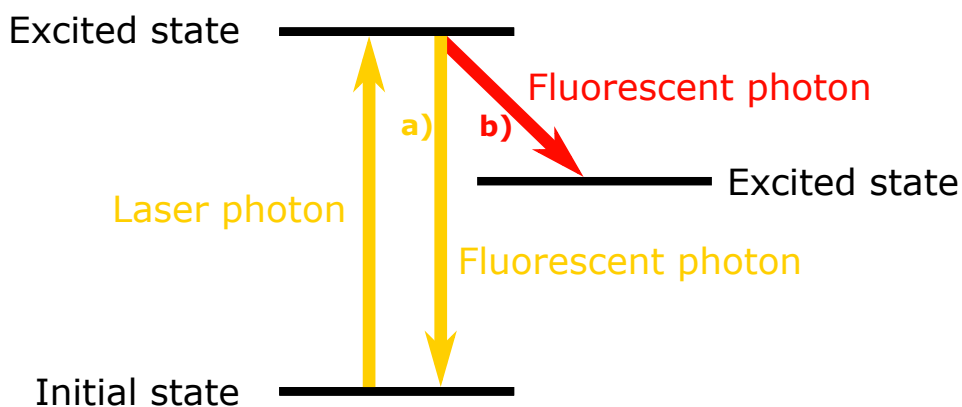
FIGURE 3.2: Schematic of laser fluorescence detection. The possible decay paths of the photon from the excited state induced by the laser will follow (a) or (b).

Frequently, the fluorescent photons have the same wavelength as the laser light, as shown by (a) of Fig. 3.2. In this case, as an atom (ion) passes through the PMT detection region, it can undergo many excitation-/emission cycles, increasing the resonance detection

efficiency [49]. However, the PMT will also be susceptible to the detection of any scattered laser light, creating a large photon background. One method for reducing scattered laser light detection is to observe photons from an alternative decay path [(b) in Fig. 3.2] involving photons of a different wavelength. With a significant enough difference in wavelength, filters placed in front of the PMT can suppress the count rate from the scattered laser light.

In studies where it is desirable to perform spectroscopy on neutral atoms, the ion beam will need to be neutralised. The ion beam is passed through an alkaline vapour, usually of sodium or potassium, where it will neutralise through the pickup of a valence electron from the vapour. For an incident ion beam X^+ passing through a neutral vapour Y, this charge-exchange reaction is described by:

$$X^+ + Y \rightarrow X + Y^+ + \delta E \tag{3.14}$$

where δE is the difference between the ionisation potential of the two elements. A detailed description of the process is found within Ref. [67]. In asymmetric charge exchange the atomic ground state isn't populated directly, and instead the population is spread over one or more higher lying atomic states. If some of these states are meta-stable, it is possible to perform laser spectroscopy directly from such a state.

The primary disadvantage of fluorescence detection arises from the relatively low quantum efficiency of PMTs. Furthermore, in order to reduce scattered laser light PMTs are positioned at distances that provide a low solid angle coverage. This reduces the detection efficiency, requiring some thousand ions for a single detected photon. In addition, ions and atoms can also exhibit fluorescence after collisions with rest-gas molecules in the interaction region, thus increasing the photon background.

However, methods exist to overcome some of these problems and improve the signal-to-background ratio. Scattered laser light can be suppressed by pulsing the laser, overlapping it in time with a synchronised bunched ion beam, and reducing data acquisition time

to the time window when the ions (atoms) pass through the detection region [68]. The recently introduced ion-coolers/bunchers have had a profound effect, reducing the energy spread of the beam to further improve the achievable resolution whilst also bunching the beam in time with the laser to reduce background. At the COLLAPS setup within the ISOLDE facility, this has been shown to reduce background rates by up to four orders of magnitude [69], with the hfs probed using ion rates as small as $150\ s^{-1}$ [70]. The same technique has also been used at the VITO beamline during studies of ^{35}Ar [19].

Ions

For in-source laser spectroscopy, fluorescence photons are emitted inside the ion source cavity, where no PMTs can be mounted. However as the lasers ionise the beam the first type of detection consists of counting ions as function of laser frequency. If the ion current from the ion source is sufficient, this is measured using a simple Faraday cup as is frequently done using the RILIS setup at ISOLDE. For beams with a low ion current, a multi-channel plate (MCP) can be used.

For the weakest beams, further beam separation techniques are usually required. Because in-source laser spectroscopy is only elementally selective, mass separation is required to remove contaminant isotopes of the same element. This is usually achieved using a dipole magnet, two such devices exist at ISOLDE see Sec. 4.2.2. Furthermore, isotopes of other elements can potentially undergo ionisation through other processes e.g. surface ionisation. If their mass is close to that of the isotope under investigation, these isobars can remain present in the beam in spite of separation with a dipole magnet.

One way to improve the mass resolving power, is to couple in-source laser spectroscopy with a further mass separator, such as the ISOLTRAP MR-ToF MS and/or Penning trap at ISOLDE [71]. For example the mass resolving power of the HRS at ISOLDE is quoted at $\approx$ 2000-5000 while the MR-ToF MS is capable of $\approx 2\mathrm{x}10^5$, see Sec. 4.1 for more details.

The cost for this dramatic increase in beam purity is the time required to complete further separation. For the isotopes ^{180,182}Au reported in this thesis, the MR-ToF MS coupled with an MCP was used to measure the hfs.

High resolution collinear laser spectroscopy has also been combined with the sensitivity of ion counting at the CRIS experiment within ISOLDE. Here, an incident ion beam is neutralised in a charge exchange cell, followed by an ion deflector to remove any remaining ions from the beam path. The neutral beam traverses into a very-high-vacuum interaction region, where a set of synchronised pulsed lasers ionise the isotope of interest in the neutral beam. The product ions are deflected into an MCP counter, where the resulting ion rate is monitored, as one of the lasers is scanned in discrete steps through a frequency range [72]. The technique is highly selective, can be used to study nuclei with very low yields, has been coupled with nuclear decay spectroscopy and has been shown to be very successful in advancing the field of laser spectroscopy [73, 74, 75].

Alpha/Gamma-Decay tagging

In addition to photon emission and ion counting, isotope identification can be achieved by examining the unique fingerprint of a nucleus' radioactive decay. The ion beam produced by in-source laser spectroscopy, can be transported to a decay spectroscopy station equipped with detectors for measuring α particles, β particles and γ-ray decays. By "tagging" on a particular decay radiation, a hfs can be measured by the decay count rate for a range of laser frequencies. For example, in the neutron deficient lead region, many nuclei decay through α-particle emission, which have a greater detection efficiency than fluorescence photons (up to 34 % at the Windmill decay station as described in Sec. 4.3). In addition to the extracted hfs, a wealth of information can be gained from studying the decay radiation of the produced isotope that is recorded in parallel, i.e α-decay transition energies, α-decay branching ratios, half-lives and transition intensities. If also coupled with γ-ray
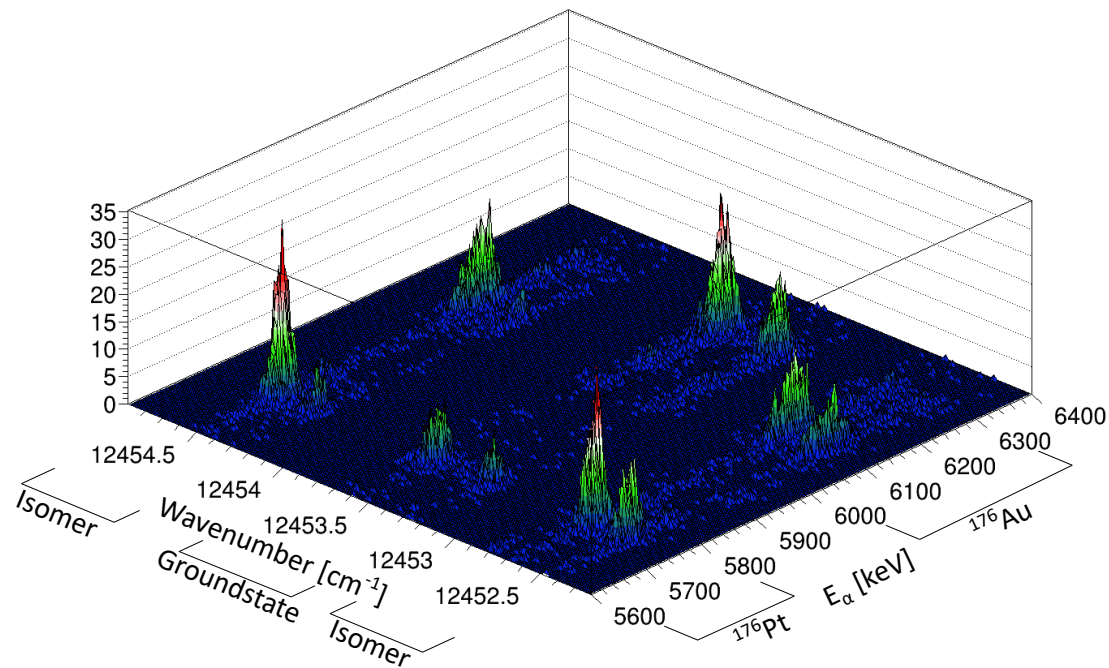
FIGURE 3.3: Surface plot of the α decay energy measured using the Windmill Decay station vs laser wavenumber recorded at the time an α particle was detected for ^{176}Au. Three distinct hfs structures are visible, two belong to an isomer and one to the ground state. ^{176}Pt, the β-decay daughter of ^{176}Au, is also present at the same frequency due to the short halflife of ^{176}Au.

detectors, α-γ and γ-γ coincidences can reveal the low energy nuclear structure of daughter isotopes following α decay. Finally, sample transport mechanisms can be exploited to move long-lived daughter products away from the implantation position using either tape transport or a rotating sample wheel. The removal of daughter products can reduce deadtime at the implantation position by removal of unwanted daughter nuclei. The gold isotopes presented in this thesis were studied via this technique, using the Windmill decay station, described in detail within Sec. 4.

The radiation tagging technique is not just restricted to α decay. If a γ-ray decay from an excited state in the daughter nucleus is prompt, the hfs of the parent can be measured by gating on the γ-ray energy. The same technique can also be applied to metastable nuclear isomers that decay via γ radiation. The limitations of the γ-decay tagging arises from the reduced detection efficiency as compared to particle decay methods. To reduce dead time, the detectors are usually placed at a greater distance from the implantation point compared to α-particle detectors, decreasing the solid angle coverage and detection efficiency. Furthermore, in studies with many daughter nuclei, the background rate from daughter/granddaughter nuclei γ-rays emitted is considerable, as γ-ray radiation is harder to attenuate through shielding or by use of a transport system to remove nuclei from the implantation position.

Beta-decay asymmetry

Unlike photons and α particles, the energy of radiation from β decay is a continuous spectrum, thus is typically not suitable for the energy tagging method. However, a hfs can be observed by combining β decay with nuclear polarisation techniques. Due to the parity violation of the weak interaction [76], β decay from an ensemble of spin-polarised nuclei is anisotropic with respect to the axis of polarisation, with an angular distribution given by:

$$W_\beta(\theta) = 1 + A_\beta \frac{v}{c} P_\mathrm{I}\, cos\theta \tag{3.15}$$

Here, W_β is the probability of emission at angle θ, A_β is the asymmetry parameter, θ is the angle between the β particles direction of emission and the polarisation axis, v is the velocity of the β particle and P_I is the degree of nuclear polarisation. For β particles of several MeV, as is the case for sodium nuclei presented later in this work, v/c is ≈ 1. The

asymmetry factor, α_β, for an allowed β transition is determined by:

$$
\begin{aligned}
&-1 \text{ for } \Delta I = -1 \\
&\frac{I_i}{I_i+1} \text{ for } \Delta I = +1 \\
&\frac{-1}{I_i+1} \text{ for } \Delta I = 0 \quad \text{(Gamow-Teller transition)} \\
&0 \text{ for } \Delta I = 0 \quad \text{(Fermi transition)}
\end{aligned}
\tag{3.16}
$$

where ΔI is $I_f - I_i$, with I_i being the spin of the parent nucleus, and I_f the spin of the daughter state fed by β decay. If enough information exists about β decay to the excited states in the daughter, i.e spins and relative β branching to each level, the asymmetry parameter, A_β, can be determined by weighting the asymmetry factors from all of the levels involved.

In this thesis β decay asymmetry studies were undertaken using isotopes of ^{26,27}Na. Using data from [77] and [78], $a_\beta(^{26,27}$Na$)$ was deduced to be -0.92(2) and -0.89(4), respectively. The theoretical β-decay asymmetry distribution can be calculated using Eqn. 3.15 if the degree of nuclear polarisation is known. At VITO, optical pumping simulations have shown that a theoretical nuclear polarisation of $\approx 60\%$ for ^{26}Na and $\approx 66\%$ for ^{27}Na should be achievable [18]. Using the above parameters, the predicted sum angular distributions of β decay from ^{26,27}Na are shown in Fig. 3.4.

To observe β decay over several half-lives, the polarised beam is usually embedded into a crystal host. The host is located inside a strong magnetic field, which acts to decouple the nuclear spin I from the atomic spin J. Polarised atoms/ions embedded into a crystal will interact with the atoms of the host material, decreasing the overall polarisation with time, see Sec. 3.3.3. By decoupling I and J the loss of polarisation due interactions with the environment is reduced. The gradual loss of polarisation is referred to as the longitudinal or spin-lattice relaxation and is characterised by a time constant T_1. As a result, $W_\beta(\theta)$
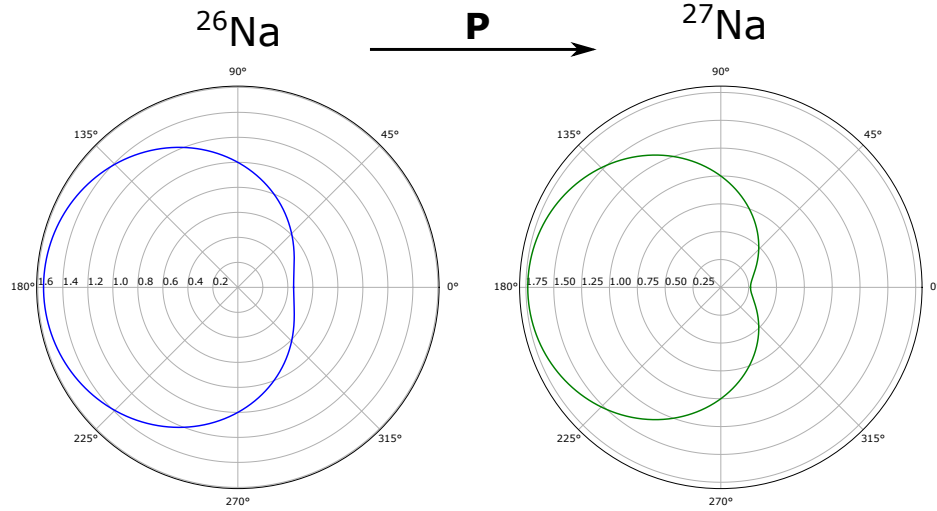
FIGURE 3.4: Sum angular distribution of β particles from allowed transition for both ^{26}Na (left) and ^{27}Na (right) for the expected achievable polarisation at the VITO beamline. The expected polarisations are $\approx 60\%$ for ^{26}Na and $\approx 66\%$ for ^{27}Na, with the polarisation axis is indicated by P.

decreases in time according to:

$$W_\beta(\theta, t) = 1 + a_\beta \frac{v}{c} P_\text{I} \, cos\theta \cdot e^{-t/T_1} \tag{3.17}$$

For cubic crystals such as NaF used as a host for isotopes of ^{26,27}Na, $T_1 \approx 40$ s and as such is much longer than the decay half-life $\approx$ 0.3-1.1 s, thus it is ignored in these studies [20].

The β-decay asymmetry measured experimentally is defined as:

$$A_{exp}(\theta_1, \theta_2) = \frac{N_\beta(\theta_1) - N_\beta(\theta_2)}{N_\beta(\theta_1) + N_\beta(\theta_2)} \tag{3.18}$$

where $N_\beta(\theta)$ is the number of β counts at angle θ in a given time interval. As is shown

in Fig. 3.4, the greatest asymmetry is observed at 0 and 180 degrees to the polarisation axis/decoupling field thus, detectors are usually placed at these angles. A_{exp} will also depend on the opening angle 2α of the detectors and will gradually decrease with increasing α. We can connect A_{exp} to the degree of polarisation using [20] :

$$A_{exp}(0,\pi) = a_\beta \frac{v}{c} P_I \frac{sin\alpha}{\alpha} \approx \frac{1}{2} a_\beta \frac{v}{c} P_I (1 + cos\alpha) \tag{3.19}$$

Here the polarisation relaxation in the material into which the beam is implanted is neglected.

3.3 β-NMR using laser-polarised nuclei

3.3.1 Nuclear Magnetic Resonance

Conventional Nuclear Magnetic Resonance (NMR) is a powerful tool which exploits the magnetic characteristics of the nucleus in order to study the physical and chemical properties of atoms or molecular structures. Any nucleus with a non-zero spin, I, has a magnetic dipole moment. Furthermore, any nuclei with $(I > 1/2)$ possesses a non-zero quadrupole moment. Both of these nuclear properties will interact with local magnetic fields and electric field gradients. Inside a strong external magnetic field we can express the total Hamiltonian of the nucleus as:

$$H = H_0 + H_M \tag{3.20}$$

where H_0 is the unperturbed Hamiltonian of the nucleus and H_M is the perturbation due to the magnetic field. For a static magnetic field, B_0, oriented along the z-axis, H_M is described as:

$$H_M = -\mu_I \cdot B_0 = -g_I \mu_N I \cdot B_0 = -g_I \mu_N I_z B_0 \tag{3.21}$$

where μ_N is the Bohr magneton and g_I is the nuclear g-factor, $g_I = \frac{\mu_I}{I \mu_N}$. This causes a nuclear state with spin I to split into $2I + 1$ sublevels within the range $I_z = m_I = -I, ..., I - 1, I$, giving rise to the Zeeman effect. These states have an equidistant splitting in energy, where the shift in energy between neighbouring states can be expressed as:

$$E(m_I) - E(m_I + 1) = |g_I| \mu_N B_0 \tag{3.22}$$

The energy splitting of the sublevels can be visualised by picturing two vectors representing B_0 and the magnetic dipole moment. Each m_I state represents a quantised, different angle in between these two vectors, see Fig. 3.5. To minimise the energy of the system,

the magnetic dipole moment will tend to align with the magnetic field, with the relevant direction determined by the sign of the magnetic moment. In thermal equilibrium, the population probability of each is state is given by the Boltzmann distribution:

$$p_i = \frac{e^{-E(m_I)/kT}}{\Sigma_{m_I} e^{-E(m_I)/kT}} \tag{3.23}$$

The resulting inbalance in the distribution of the nuclear population corresponds to a macroscopic alignment of the nuclear spins, thus polarisation. In conventional NMR with fields up to ≈ 10 T, polarisation is on the order of 1 part-per-million (ppm) [79].
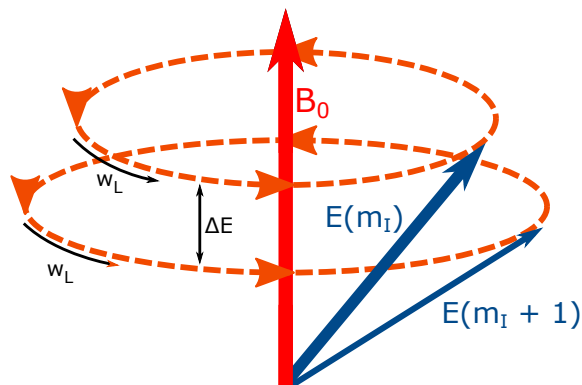
FIGURE 3.5: Diagram of Larmor precession of a nucleus with $\mu_I > 0$ around the axis of an externally applied magnetic field B_0. The magnetic dipole will precess around with a frequency ν_L, with lower energy states E(m_I) being more (closely) aligned the field axis. The thickness of the arrows E(m_I) and E($m_I + 1$) represent their relative populations given by the Boltzmann distribution.

The angular momentum of the nuclear state gives rise to discretized projections on B_0. This can be visualised as the precession of the magnetic dipole moment around B_0 with a

frequency v_L, also known as the Larmor frequency, expressed as:

$$v_L = g_I \mu_N B_0 \tag{3.24}$$

which depends on the strength of the magnetic field, and the nuclear magnetic moment. If we irradiate the nuclei within B_0 with a perpendicular electromagnetic wave of a frequency equal to the Larmor precession, we observe the resonance condition where the photon energy corresponds to the Zeeman splitting such that:

$$\Delta E = |g_I| \mu_N B_0 = w_L \hbar \tag{3.25}$$

Therefore, by scanning the frequency of the irradiating electromagnetic wave, or by adjusting the B_0 field, an absorption and corresponding transversal electromagnetic wave emission is observed when the resonance condition is fulfilled. The irradiation electromagnetic wave is created by a coil in a plane orthogonal to B_0, often acting as the pickup induction coil in pulsed NMR. In continuous wave NMR two coils are required, one to administer the radio wave and the other to act as the pickup coil. From Eqn. 3.25, knowing the precise magnetic field and Larmor frequency can be used to derive g_I, and thus if the spin of a nucleus has been measured, provide an accurate determination of the magnetic dipole moment.

3.3.2 Optical Pumping

The quality of the measured hfs or NMR resonances from β-decay asymmetry is heavily dependent on the polarisation of the nuclear ensemble. The polarisation provided by the magnetic field in conventional NMR (usually on the order of 10^{-6}) is not sufficient to study the small number of atoms typically produced at radioactive ion beam facilities. To increase the nuclear polarisation numerous techniques exist, such as nuclear reactions with
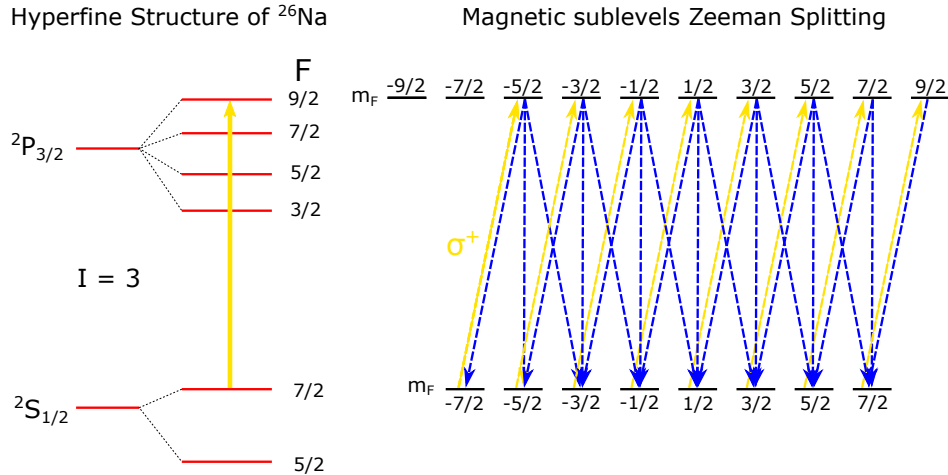
FIGURE 3.6: Atomic spin polarization via optical pumping with σ^+ light on the example of $F = 7/2$ $\rightarrow F = 9/2$ component of the D2 line in ^{26}Na. σ^+ circularly polarized light induces transitions with $\Delta m_F = + 1$. Because the de-excitation can take place for $\Delta m_F = -1$, 0 or +1, after several excitation-decay cycles the lower state with $m_F = + F$ will be the most populated state and the atomic spin will be polarized.

a selected recoil angle, capture of thermally polarised neutrons, low temperature nuclear orientation or by interaction with circularly polarised laser light. The latter method, referred to as optical pumping, is used at the VITO beamline and has been shown to produce a high degree of polarisation [19, 20].

During optical pumping, a beam of atoms/ions is irradiated by circularly polarised laser light which induces transitions between the m_F magnetic sub-states of the hfs lower and upper level, see Fig. 3.6. Upon interaction, an electron is excited to a state with $\Delta m_F = +1$ for σ^+ ($\Delta m_F = -1$ for σ^-). After excitation, photon decay occurs anisotropically with either $\Delta m_F = -1$, 0 or +1. The laser will interact with the atoms/ions multiple times, gradually

pushing the population to states corresponding to the highest m_F for σ^+ or lowest m_F for σ^-. Through the hyperfine interaction, polarisation of atom/ion m_F leads to a polarisation of the nucleus. The optical pumping scheme for ^{26}Na is shown in Fig. 3.6.

Depending on the transition chosen, the spontaneous emission from the upper state transpires to another state or hyperfine level of the lower hfs, provided the selection rule $\Delta F = 0$ or ± 1 is obeyed. One example in ^{26}Na is the $F = 7/2 \rightarrow 7/2$ transition, which could then decay to the 5/2 component of the ground state, see Fig. 3.6. These "dark states" do not interact with the laser again, limiting the degree on nuclear polarisation to less than 100 %. To overcome the loss of polarisation through dark state feeding, neighbouring hyperfine lines can also undergo optical pumping in a process known as multi-frequency pumping, which has been demonstrated at the VITO beamline in studies of ^{35}Ar [19].

3.3.3 Detection via β-decay asymmetry

Following polarisation, the ion/atom ensemble is confined in space usually by implanting the radioactive beam into a host crystal. On implantation the electron spins will lose their polarisation rapidly due to the interactions of their large magnetic moments within the crystal lattice, thus the nuclear spins need to be decoupled from those of the electron cloud. The static magnetic field is gradually increased in front of the stopping crystal to adiabatically move the ensemble from the Zeeman to the Paschen-Back regime, which splits the m_F states into their m_I and m_J sub-components, see Fig. 3.7.

The choice of the host for the polarised nuclei is also extremely important. If a nucleus has $I > 1/2$, it will possess a quadupole moment, which will interact with local electric field gradients, causing additional shifts in the hyperfine level structure. For the β-NMR studies at VITO, a sodium fluoride (NaF) crystal with a cubic lattice structure was used, such that if the nuclei were implanted onto substitutional lattice site, no static electric field
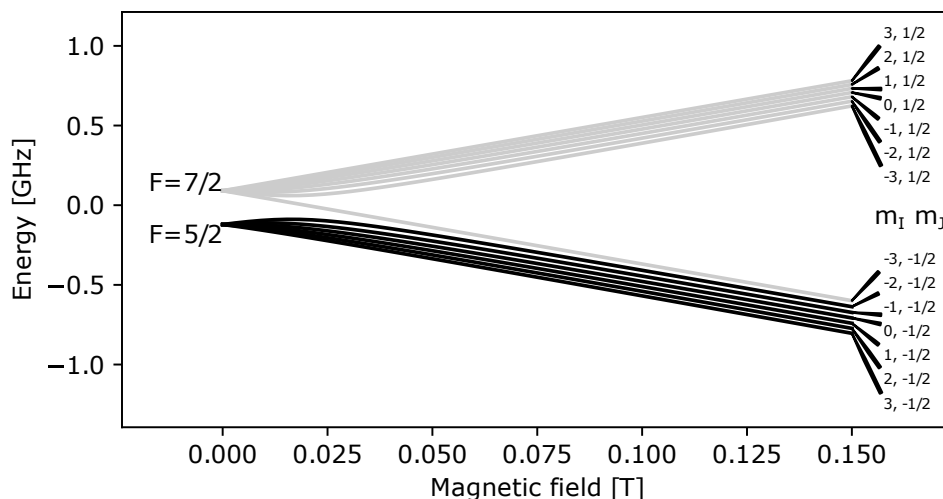
FIGURE 3.7: Behaviour of the hfs of ^{26}Na with increasing magnetic field.

gradient would be present. Therefore only the static magnetic field, B_0, contributes towards the energy level splitting and thus the resonance frequency position.

The decay of the implanted nuclei is observed using β-detectors in the axis of the magnetic field, on either side of the sample. The nuclei will decay with an experimental asymmetry proportional to the polarisation provided by optical pumping. When radio-frequency (RF) waves are applied in resonance, the energy absorption of the radiation will lead to a redistribution of the nuclear population from the polarised m_I state, to different m_I states, observed as destruction of the β-decay asymmetry. By recording the resonance frequency at which this happens, information about the probe nucleus, or implantation host can be gained. The primary advantages of observing a resonance via β-NMR as opposed to conventional NMR is the increase in sensitivity of up to 10 orders of magnitude [45]. The range of radioactive nuclei available can also be a great benefit if a suitable stable NMR sensitive isotope doesn't exist (i.e. with a large or 0 spin). The latter was the case for

studies involving ^{35}Ar.

Up until this point, β-NMR has been discussed as a tool for probing the properties of an implanted radioactive nucleus. However, nuclei with properties that are well known can be used to instead probe the implantation environment; one such example is implanting a probe into a molecular structure. Recall Eqn. 3.22, showing the energy difference between two m_I sub-states is dependent on the strength of the external magnetic field. If an atom is instead placed inside a molecule, it will share electron pairs to form a chemical bond. As this modifies the density of the electron cloud surrounding the nucleus, this in turn will "shield" or "de-shield" the nucleus from B_0 and therefore alter the NMR resonance frequency. This is known as chemical shift and is a small effect, typically on the order 1-100 ppm. There is great interest in using β-NMR to study inorganic chemistry and biology, motivating the construction of many new experiments world wide.

4 Application of Techniques at ISOLDE, CERN
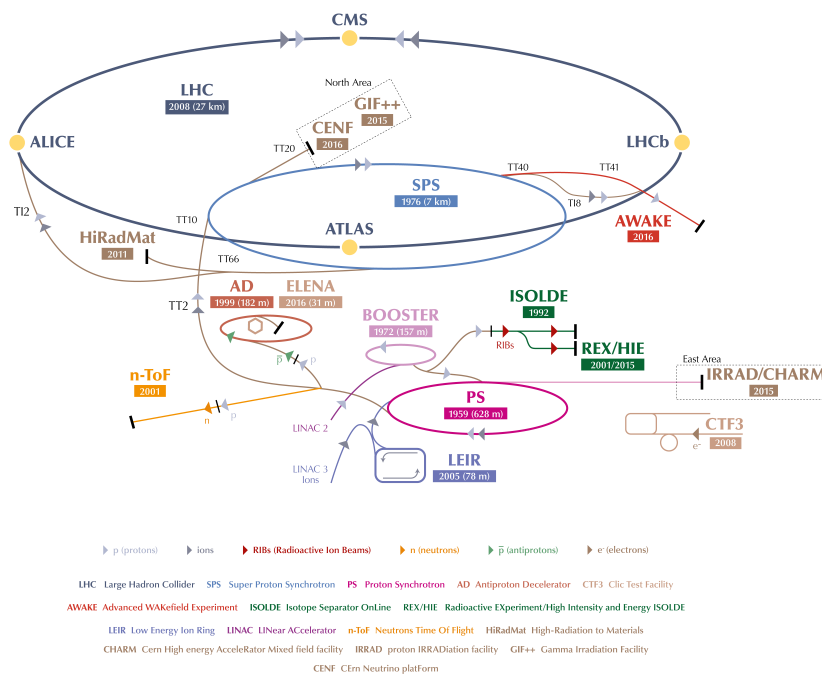
FIGURE 4.1: A schematic diagram of the CERN accelerator complex as of 2017, image taken from [80]. The ISOLDE nuclear physics facility and REX/HIE-ISOLDE are shown in green.

The results discussed in this thesis are from experiments performed at the Isotope Separator On-Line DEvice (ISOLDE) facility situated within the CERN accelerator complex in Geneva, Switzerland. The facility is located just after the Proton-Synchrotron Booster (PSB), as shown in Fig. 4.1.

4.1 ISOLDE
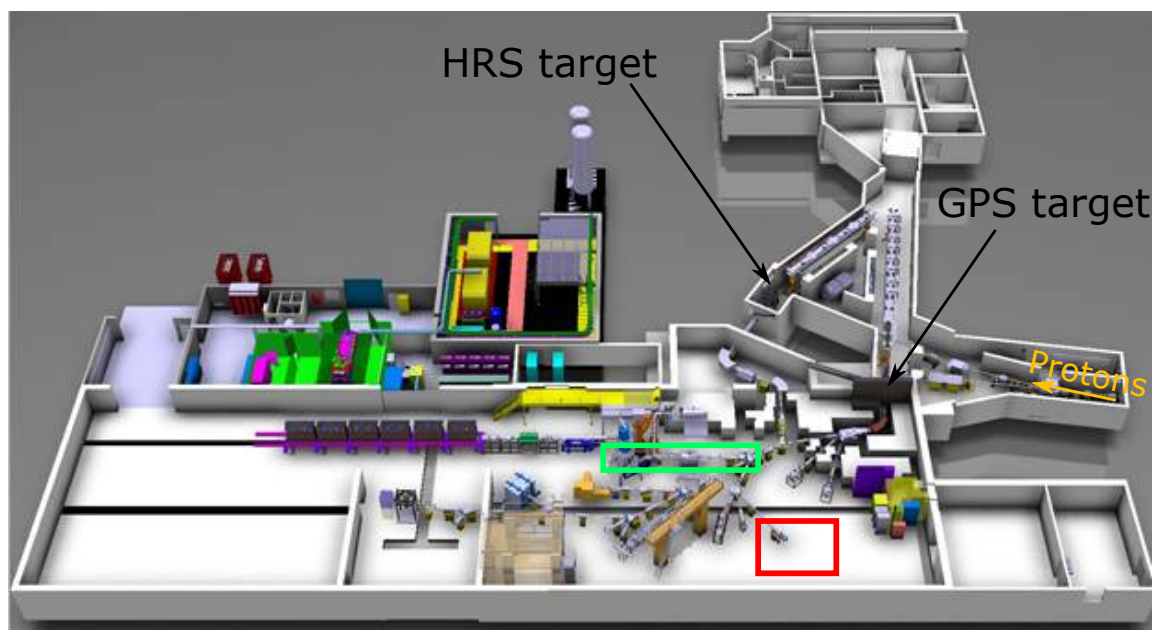
FIGURE 4.2: A schematic diagram of the ISOLDE Facility [81]. The location of the two target stations is indicated. Shown in red is the location of the Windmill decay station and in green is the VITO polarisation beamline

ISOLDE was initially proposed as an experimental facility attached to the 600 MeV Proton Synchro-Cyclotron (SC) at CERN in 1964 [82]. The first experiments began in 1967, with numerous upgrades to the facility starting with ISOLDE-II in 1974 to handle an

increase in beam intensity from the SC. In 1983, the collaboration commissioned a second separator to maximise the use of the available beam time [82], [83], ISOLDE-III. With the closure of the SC in 1990 the facility was moved to the PSB in 1992 to form its current configuration, ISOLDE-IV [84]. Fig 4.2 shows a 3D schematic of the lab.

The facility uses the Isotope Separation On-Line (ISOL) technique [85] in order to produce beams of radioactive ions. Thus far at ISOLDE, over 1300 different isotopes of 73 chemical elements have been produced [86],[87]. The Au and Na isotopes that are the focus of this work were produced via bombardment of a UC_x target with 1.4 GeV protons. The gold and sodium atoms were ionised through laser ionisation for the former and surface ionisation for the latter, after which extraction is performed via an electrostatic potential and followed by mass separation. The isotopically-pure beam is then delivered to one of the numerous detector stations based throughout ISOLDE. A more detailed discussion of the beam production process and detection stations used for this work, is provided in the following sections.

4.2 Beam production

The PSB delivers a 1.4 GeV proton beam, in bunches of 2.4 μs with a period of 1.2 s and an intensity of 3.1×10^{13} protons, providing an average beam current of 2.1 μA [85]. The pulses are arranged into a logical sequence called the "supercycle", which can contain between 30-40 proton pulses. These are distributed among the many different facilities at CERN. Normally, ISOLDE will receive up to ≈ 61 % of the proton pulses accelerated by the PSB [88].

At ISOLDE, the proton beam impinges on a 50 g/cm^2 thick UC_x target (although other target materials are frequently used [89]), producing a wide range of nuclei, primarily through spallation, fragmentation and fission reactions. The neutral recoil products, are stopped inside the target material. The products diffuse through the target and effuse to a

heated transfer line into a hot cavity, see Fig.4.3. Atoms with a low enough ionisation potential (such as sodium, 5.139076(2) eV [90]) can be ionised upon contact with the heated surfaces of the target, transfer line or hot cavity ion source (heated to T ≈ 2100 °C). Species with a higher ionisation potential require an alternative method of ionisation, such as the use of lasers, to selectively ionise the isotope of interest within the cavity.
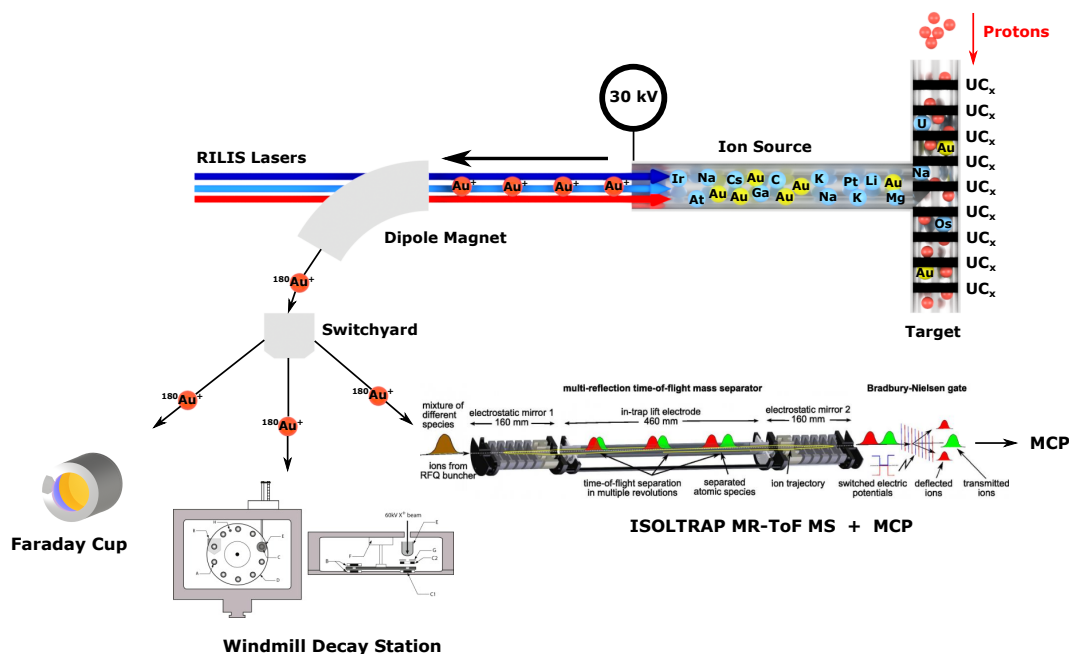
FIGURE 4.3: Schematic drawing of the in-source resonance ionisation spectroscopy setup for the experiment on gold ions. Protons are incident on a UC_x target (top right), with the neutral reaction product nuclei further ionised by lasers from RILIS. Mass separation is performed by a dipole magnet after which the beam is delivered to one of three spectroscopy setups, a Faraday cup, the Windmill decay station or the ISOLTRAP MR-ToF MS.

4.2.1 RILIS

For reaction products which are not easily surface ionised, the RILIS (Resonant Ionisation Laser Ion Source) can be employed to selectively ionise an element for study. This ion source functions by using step-wise resonant excitations of atomic transitions via wavelength tunable lasers, as described in Sec. 3.2.1. The atomic transitions are unique to each element, providing an enormous degree of selectivity. The lasers can be tuned in an optical range between 210-950 nm, with a typical ionisation efficiency ranging from 0.2-27 % depending on the element [91]. An atom can diffuse out of the hot cavity in less than 0.1 ms, so to increase ionisation efficiency the pulsed lasers have a repetition rate of $\approx$ 10 kHz.

The hardware of the RILIS system will be described briefly, more details of the RILIS layout for operation can be found in [92] and the references there in. The system consists of three dye lasers pumped by a single frequency doubled Nd:YAG laser, three tunable titanium:sapphire (Ti:Sa) lasers pumped by a further two Nd:YAG lasers with two additional Nd:YAG lasers on site available as spares to reduce downtime. Finally when required, there is a dedicated frequency doubled $Nd:LYO_4$ (providing up to 40 W output power at 532 nm) for further excitation and eventually - ionization of the atoms under study. This equipment allows the RILIS team to set-up multiple different experiments in parallel and reduces the time required to switch ionisation schemes between experiments [35].

The three step ionisation scheme used in the gold experiment is shown in Fig 5.10. If one of the lasers used in an ionisation scheme is scanned across the frequency range of a particular transition, the hfs can be observed by measuring the ionization photocurrent as a function of laser frequency. During the gold experiment, this was performed using the first step of the ionisation scheme. Ion tagging was performed using the Windmill (for ^{180}Au) and with the MR-ToF MS + MCP for both ^{182,180}Au.

HFS scanning procedure

During the hfs measurements of ^{182,180}Au, the first transition of the ionisation scheme was scanned using a laser that operates in narrowband (NB) mode. In this mode the linewidth of the laser is ≈ 1 GHz [35], comparable to the Doppler broadening of the atomic transitions of the heavy elements within the hot cavity ion source, see Sec.3.2.1. The remaining excitation steps of the ionisation scheme are performed by lasers operating in a fixed-frequency broadband (BB) mode. Here the typical laser linewidth is ≈ 10-20 GHz, covering the full range of the hfs of all isotopes of a given element. This ensures all isotopes are ionised with the same efficiency.

To scan the hfs, the frequency produced by the NB laser is changed in a series of discrete steps. The NB laser is tuned by adjusting two etalons in order to select the desired frequency [92]. Once the selected frequency is stabilised, the beamgate to the ISOLDE target is opened and the ion beam is delivered to either the Windmill decay station or MR-ToF MS, see Sec. 4.3.2 . The α decay rate within a certain energy range (for the Windmill) or the ion count rate (for the MR-ToF MS) is measured for a fixed time interval, after which the data acquisition is stopped and the beamgate closed. The laser is then re-tuned to the next frequency, while the wheel of the Windmill rotates providing a fresh foil for implantation. This process is repeated until the full hfs range has been scanned.

4.2.2 Mass Separation

After selective ionization, the ions are extracted from the hot cavity and accelerated up to 60 keV by an electrostatic potential, and mass separated by their mass-to-charge ratio. At ISOLDE there are two on-line mass separators, each with their own target station. The General Purpose Separator (GPS) consists of a single $70°$ magnet with a bending radius of 1.5 m and a mass resolving power of M/ΔM $\approx 2,400$ [85]. Inside the separator there are two pairs of movable electrostatic plates which provide the simultaneous production of

three different ion beams within $\pm$ 15 % of the central beams mass. These beams can then be diverted to either the GLM (General Low Mass) or GHM (General High Mass) beamlines for solid state studies, medical isotope collections or small experimental set-ups [93, 94, 95].

The High Resolution Separator (HRS) is comprised of one 90° and one 60° bending magnet, each with a bending radius of 1 m, which when combined have a mass resolving power of M/ΔM $\approx$ 2000-5000. With such a high resolving power only a single specific mass is produced and transported from the HRS. After the separator, the beam passes into the Radio Frequency Quadrupole Cooler Buncher (RFQ-CB, see below) to optionally bunch and cool the ions, essential for modern collinear geometry laser spectroscopy experiments. In the gold experiment the GPS was utilized, while for the sodium experiments the HRS was used, due to the requirement of the RFQ-CB for some measurements.

4.2.3 The Radio Frequency Quadrupole Cooler Buncher

Depending on the ion source used, ion beams from the source typically have an emittance of 10-30 π mm mrad and longitudinal energy spread of 5 eV at 60 keV [96]. While this is suitable for decay spectroscopy, many experiments benefit from improved emittance and a reduced beam energy spread. For example, in collinear laser spectroscopy this would increase the overlap of the incoming beam with the path of the laser [97]. Both separators would benefit from the installation of an Radio Frequency Quadrupole Cooler Buncher (RFQ-CB), but due to the layout of the facility, it was only possible for it to be installed after the HRS [96].

The RFQ-CB is a linear Paul trap with four segmented electrodes (see Fig. 4.4), which act to confine the ions along a central axis [97]. The trap is filled with a helium buffer gas at $\approx$ 0.1 mbar, cooling the injected ions through thermal collisions. Both the entrance and exit windows of the RFQ-CB contain a series of small apertures to permit differential pumping
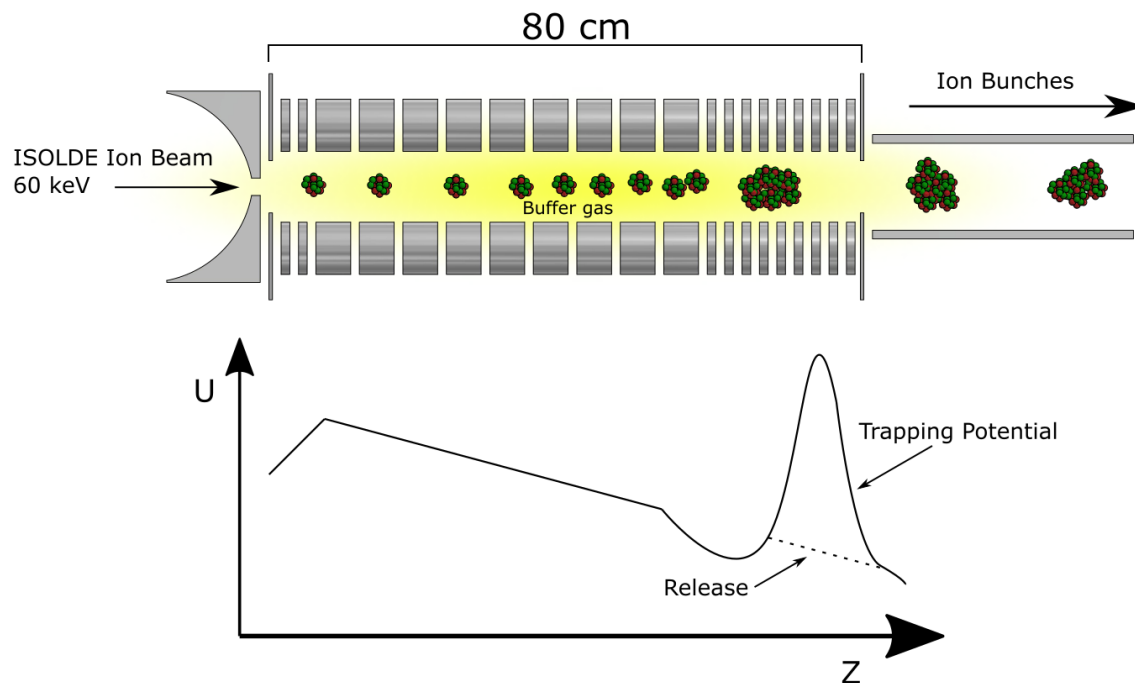
FIGURE 4.4: A Schematic diagram of the RFQ linear Paul trap

between the high vacuum of the separator/beamline and the helium environment of the trap. Over the length of the drift tube, the potential of the electrodes is gradually reduced by 1 V/cm, see Fig. 4.4. The potential across the end electrodes can be increased in order to create a potential well. Ions accumulate in the well, in effect bunching the beam. The amount of ions that can be contained within the region is limited by space charge effects, though up to 1×10^7 ions can be contained [97]. The potential on the end electrodes is then pulsed to release the ion bunch.

The RFQ-CB has been shown to have a transmission efficiency between 50-80 % depending on the mass of the isotope and ion source used [96]. By bunching the beam and coordinating it in temporal sequence with the laser, photon background from scattered laser

light has been suppressed at COLLAPS by a factor 4 x10^3 [98]. Bunching is used at VITO for polarisation relaxation measurements, which benefit from a rapid accumulation of radioactive sodium to observe the decay of the nuclear polarisation over time in different sample environments.

4.3   The Windmill Decay Station
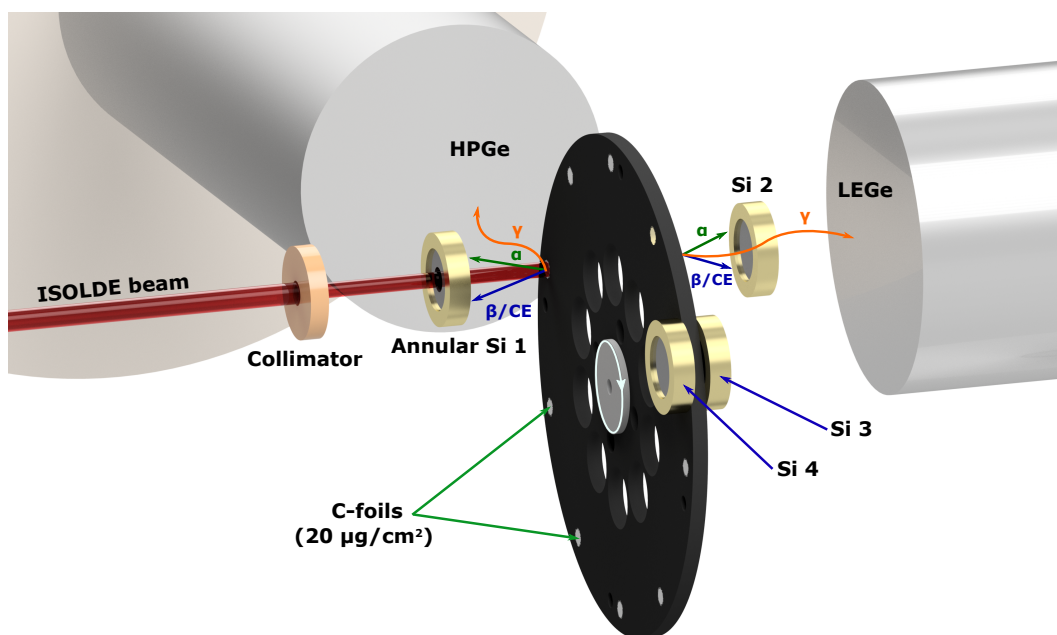
FIGURE 4.5: Schematic diagram of the Windmill setup. The beam from ISOLDE passes through hole in the annular silicon detector (Si1), and is implanted on one of 10 carbon foils. Si1 and Si2 are offset from the rotating wheel in the diagram for illustrative purposes only.

For the experiments involving the gold isotopes, the laser-ionised and mass separated beam was delivered to the so-called Windmill decay station. The beam passes through a central hole in an annular silicon detector (Si1) and is implanted into one of 10 carbon foils of 20 μg/cm^2 mounted on a rotatable wheel (see Fig. 4.5). A second surface-barrier silicon detector (Si2) is positioned 5 mm behind the implantation foil (see Fig. 4.5). The total detection efficiency for α particles was $\approx 34\%$. A second pair of surface-barrier silicon detectors (Si3 and Si4) are located four foil positions away from the implantation point,

to observe longer lived α decay from the daughter products of each gold isotope. For details of the silicon detector calibration procedure, see Sec. 5.1. A typical full width half maximum (FWHM) energy resolution of 25 keV and 30 keV was observed for α decays in the energy region 5-6 MeV for the annular silicon detector and surface-barrier silicon detectors, respectively. A ^{241}Am source was placed inside the Windmill for initial detector calibration.

A single crystal High-Purity Germanium detector with a thin beryllium window (LEGe), was placed outside the chamber behind the implantation point, along the axis of the beam. The typical energy resolution (FWHM) of the LEGe at 121.8 keV was 1.1 keV. A High-Purity Germanium detector with a typical energy resolution of 2.3 keV at 1178 keV was placed outside the Windmill chamber orthogonal to the implantation point. Both detectors were calibrated using sources of ^{152}Eu, ^{137}Cs, ^{133}Ba and ^{60}Co (see Sec. 5.1 for further details).

4.3.1 The Windmill Data acquisition system

As mentioned in Section 4.3, the wheel of the Windmill was rotated to remove longer lived decay products from the implantation point. The frequency of the rotation was normally tuned to a specific number of SC, which could be varied by the user depending on the production rate and half life of the isotope under study. This also provided a logical point to retune the laser frequency, required during hfs measurements.

For data collection, 8 Digital Gamma Finder (DGF) revision 4C, digital electronic modules from XIA were used [99]. Through four input channels, each module received and processed electronic signals and time stamped each event using an internal clock. Each event processed by a DGF was given a number of stamps which were used in the analysis of the data:
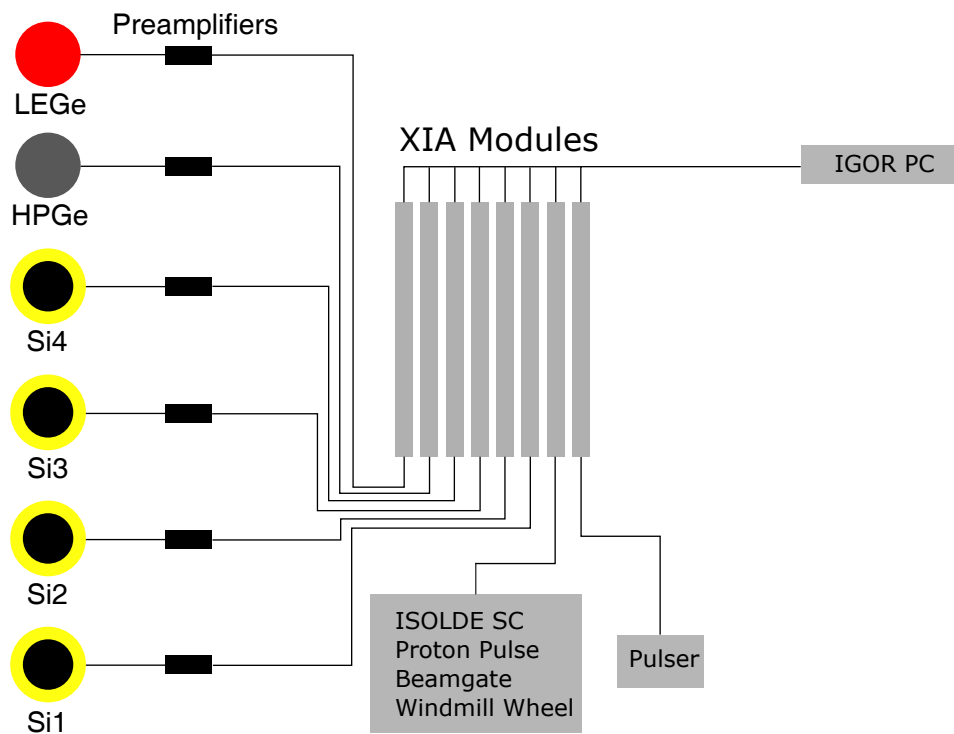
FIGURE 4.6: Schematic diagram of the Windmill DAQ setup.

- Identification stamp - informs the system in which channel and module the signal was received (i.e. an α decay registered in a Si detector)

- Time stamp - Gives the time an event was registered in the DGF with a precision of 25 ns.

- Energy stamp - proportional to the intensity of the electronic signal received by the DGF, the greater the signal the larger the energy of an event.

In total, eight modules were used in the gold experiment. The energy signals passed through preamplifiers before being sent on to one of the modules (see Fig. 4.6). Of the

two remaining cards one was devoted to a pulser at 100 Hz, used to monitor the total live time of each run. The final module was used to record signals from the clock logic in order to control and synchronise the recording of data with the rotation of the wheel. Remote control of these modules and their internal clocks was synchronised by a dedicated data acquisition computer using the IGOR software package written by wave metrics [100]. Data was written from the module buffers to the hardrive of the PC, synchronised using a logic gate in order to minimise dead time from the readouts.

4.3.2 The MR-ToF MS

The Windmill hfs technique is suitable for short-lived α-decaying isotopes, with a proven sensitivity of up to 0.01 ions/s. However the application of the technique is hampered in the case of long-lived isotopes when it is impractical to wait for the decay to occur. Furthermore, β-decaying isotopes or heavily contaminated beams are difficult to measure using the Windmill setup. In such cases, ISOLTRAP's Mult-Reflection Time-of-Flight Mass Separator (MR-ToF MS) was used. The device is sufficiently sensitive to measure ions rates as low as a few ions per minute [101]. A brief description of the MR-ToF MS is given below and a diagram is shown in Fig. 4.3. More details can be found in [102].

The ion beam from the GPS separator is electrostatically decelerated before it first enters ISOLTRAP's RFQ-CB [103], which cools and bunches the ions in the same fashion as the HRS RFQ-CB, described in Sec. 4.2.3. After bunching, the ions are injected with a beam energy of 3.2 keV into a 460 mm drift tube in the center of the MR-ToF device. Two electrostatic mirrors of a fixed potential and 160 mm in length, are positioned at either end of the tube. Each mirror has a central aperture through which the initial ion beam and mass separated beam enter and exit the device. The injection energy of the ions is sufficient to overcome the potential of the entrance electrostatic mirror, after which the kinetic energy of beam is lowered by reducing the potential of the drift tube. This confines

the ions between the two mirrors. The ions are reflected back and forth between the mirrors several thousand times, producing a flight path of several km. As all isobars are injected with the same kinetic energy, this produces a temporal separation due to the differences in mass of the nuclei injected into the device.

After a set revolution time, the potential of the drift tube is raised, increasing the kinetic energy of the ions sufficiently to bypass the exit electrostatic mirror (see Fig. 4.3). Upon exiting the device the ions pass through a Bradbury-Neilsen gate [103]. This is a high temporal resolution deflector separating the beam in time, deflecting the unwanted ions and transmitting the desired nuclei. The transmitted ions are counted using an multichannel plate (MCP). The device has mass resolving power of $\approx 2\text{x}10^5$, with the whole process taking ≈ 30 ms. The hfs of both ^{180,182}Au were studied using this device.

4.4 VITO - A new laser polarisation beamline
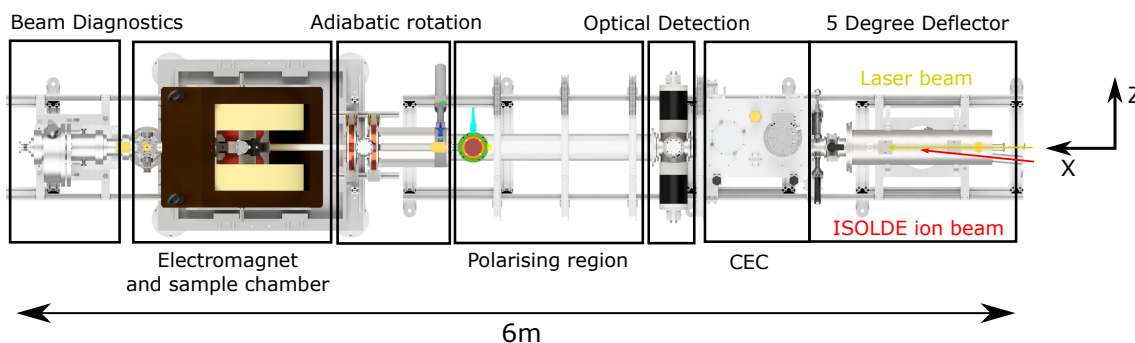
FIGURE 4.7: 2D Schematic of the VITO Beamline at ISOLDE as viewed from above, the axes indicate the magnetic field directions reference in this section.

Radioactive beams of spin-polarised nuclei are of great interest for a plethora of studies, ranging from nuclear structure, fundamental interactions, material sciences and life sciences. To facilitate the increasing demand for such beams, a new laser polarisation beamline, referred to in this text as the Versatile Ion-polarised Techniques Online (VITO) beamline, has been constructed at ISOLDE. Nuclei are first polarised, then implanted into a host crystal or sample of interest from which β-decay asymmetry is measured in opposing directions. The relevant information is extracted from an excitation radio-frequency applied to the system, which resonantly destroys the nuclear polarization.

The first experiments commenced in 2016, successfully measuring β-decay asymmetry from ^{26,28}Na in a NaF crystal, as previously demonstrated at COLLAPS [21, 104]. This has progressed into pursuit of measuring the interaction of Na$^+$ cations with DNA quadruplex structures [45]. A thorough discussion of the different components of the polarisation beam line can be found in our recent publication [18], though some of the key elements will be summarised here.

4.4.1 5 Degree deflector

The ion beam from ISOLDE first enters the VITO beamline through a 5 degree deflector with a 40-mm opening. This contains two pairs of electrostatic steering plates, two in the horizontal plane machined with a bending radius of 2 m and two in the vertical plane (see Fig. 6 in [18]). These act to bend the ion beam through five degrees to enable overlap with the laser beam (which enters through a 25 mm window at the rear of the deflector). After deflection there is an adjustable conductive iris from which the beam current can be read, to aide in adjusting the ion beam focus for maximal laser-ion beam overlap. The aperture can be shut completely or opened to 50 mm. There is also conductive plate to readout the ion current, that can be slid into and out of the setup.

4.4.2 Voltage Scanner and Charge Exchange Cell

After the iris, the beam enters the charge exchange vacuum chamber, see Fig. 4.7. The inner components of the chamber are detailed in Fig. 4.8. First, the beam passes through a specially designed electrode arrangement hereafter referred to as the voltage scanner. The voltage scanner is comprised of eight tapering electrodes (red in Fig. 4.8) mounted in a circular configuration. The potential of these electrodes is modified to adjust the velocity of the ion beam and induce a Doppler shift in transition frequency of the polarising laser as seen by the ion beam. A grounded cage (green in Fig. 4.8) surrounds the electrodes. Over the length of the scanner, the kinetic energy of the ion beam is changed gradually to reduce any focusing or steering effects from a non-axially aligned ion beam. The voltage to the scanner is supplied by a KEPCO x100 amplifier, which multiplies the applied voltage from the DAQ software by a factor of 100. This increases the available scanning range, such that it is greater than an isotopes hfs. Further details can be found within [18].

At VITO it is possible to polarise both ions and neutral atoms. In the case of sodium, it is preferential to polarise neutral atoms using the $^2S_{1/2} \to {}^2P_{3/2}$ transition. To achieve

Figure with labels: Ion beam, Voltage Scanner, CEC, ^{23}Na Vapour, Ion deflector, Laser beam, Atom beam, Fluid Circulator, Optical Collimator
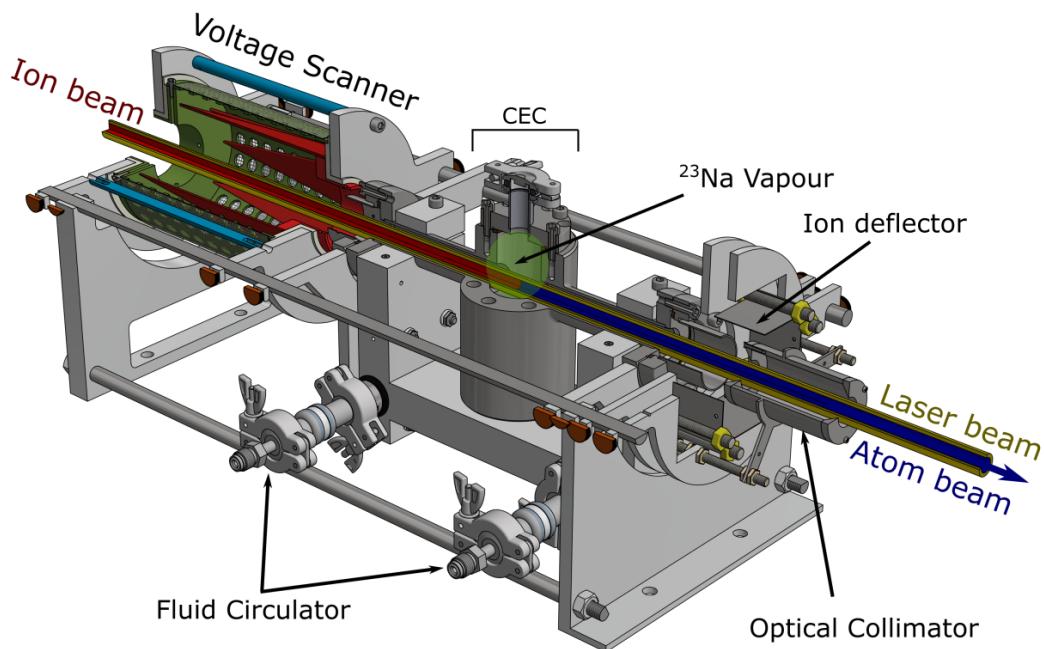
FIGURE 4.8: 3D Schematic of the inner components of VITO's charge exchange chamber. The ion and laser beams enter from the left of the diagram.

this, the ion beam must be neutralised in a charge exchange cell (CEC), see Fig. 4.8. The CEC is a small chamber heated to $\approx 300\,^{\circ}$C by six cartridge heaters (a resistive coil of wire which is wound around a ceramic block, surrounded by a dialectic material and encased in a metal sheath). Inside the chamber, the heat melts a reservoir of stable ^{23}Na, vaporising it into a gas which diffuses into the beam path. Through collisions with the ^{23}Na vapour in the central cavity, the ion beam of radioactive sodium is neutralised. The CEC is placed on a hollow conductive block of copper. Inside the block, Galden (an oil-like fluid with a low electrical conductivity) is circulated at 100 $^{\circ}$C. This cools the ends of the CEC beam pipe, such that any sodium vapour that diffuses out from the central cavity condenses through

collisions with the walls instead of dispersing throughout the beamline. The Galden is circulated into the block from an external oil heat exchanger via the two oil circulator feedthroughs, as shown in Fig. 4.8.

Ions of sodium that are not neutralised in the charge exchange cell, are removed from the beam path via a pair of electrostatic plates located after the optical collimator, one grounded and the other at a potential of 1 kV.

4.4.3   Polarisation Interaction region

After the CEC chamber, the beam passes into an optical detection region. At the entrance of this section there is a collimator with a pair of knife edges. The collimator decreases the amount of laser light scattered from surfaces within the CEC that enters the optical detection region, reducing the photon background for optical resonance scanning. Two PMTs detect photon resonances as described in Sec. 3.2.3. However, due to the low detection efficiency, this was not utilised in the studies involving the sodium nuclei.

Following the optical detection section, the atom and laser beams enter the polarisation interaction region, see Fig. 4.7. Here, repeat excitations of the D2 line, $^2S_{1/2} \rightarrow {}^2P_{3/2}$ transition in sodium polarised the atoms as discussed in 3.3.2 over an interaction length of 1.6 m. This length was chosen as a compromise between achievable polarisation and available space within the ISOLDE hall. The typical laser power recorded at the end of the beamline was 80 mW/cm^2, which should induce a theoretical polarisation of ≈ 70 % for ^{26}Na in the strongest component of the hyperfine spectrum, see Fig. 5 in [18]. A weak guiding magnetic field of 20 G was applied in the direction of the atom/ion beam path to define a quantization axis and prevent the atomic spins coupling to potential stray magnetic fields in the surrounding environment. This field was induced by four copper coils 800 mm in diameter, placed in a Helmholtz configuration, see Fig. 4.7.

At the end of the polarising region there is a segmented, conductive collimator with a 1 cm opening, see Fig. 6.8. Four isolated segments detect the beam current deposited on the collimator. The beam can be steered and focused using the electrostatic elements in the 5 degree deflector, until no ion current is observed from the readout plates. Using the segmented collimator and the iris located at the end of the 5 degree bender, ensures a good overlap of the atom and laser beam in order to maximise the degree of polarisation achieved.

4.4.4 Spin rotation and decoupling

Following the polarisation interaction region, the atoms were implanted into a host sample in the centre of a 0.5 T electromagnet or (in the final experiments presented in this work) a 1.2 T Bruker BE25 electromagnet, henceforth referred to as the NMR magnet. As the field direction of the NMR magnet (B_z) was perpendicular to the polarization axis (B_x), the atomic spins underwent adiabatic rotation into B_z prior to implantation. This rotation was performed in a transitional field of $\approx$ 100 - 200 G applied in the B_z direction. The field also decoupled the electron and nuclear spins, an effect that continued into the fringe field of the NMR magnet. On implantation into the sample, the electron spin polarisation is easily disturbed, therefore decoupling the two spins preserves the nuclear polarisation for an increased duration.

The transitional field is provided by a series of solenoids, including a large solenoid, two Helmholtz coils and a small segmented solenoid tube as indicated in Fig. 4.7. The field profile produced by these coils was simulated using COMSOL, with the results shown in Fig. 4.9. These results closely match the experimental data measured with a hall probe, shown in blue in Fig. 4.9. Due to the intensity of the field required from the Helmholtz coils, they were water cooled in parallel plumbing circuit with the NMR magnet.
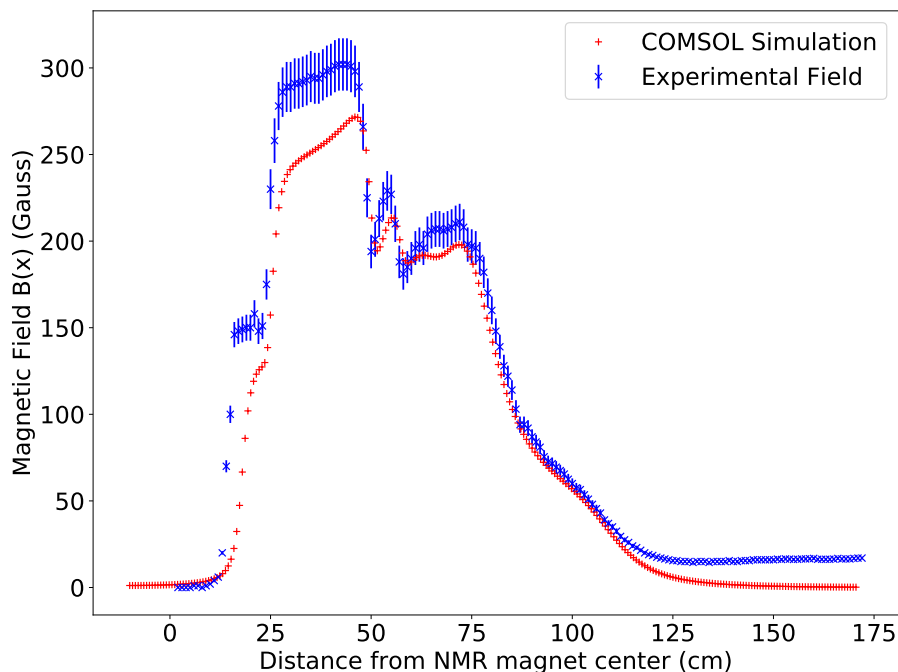
FIGURE 4.9: Simulation (red +) and experimental (blue x) measurements of the magnitude of VITO's transitional magnetic field. The atom beam beam direction of travel is from right to left.

4.4.5 NMR using Radio-Frequency

A schematic diagram of the detection chamber within the NMR magnet is shown in Fig. 4.10, a 3D CAD drawing is also shown in Fig. 6.17. Once the atoms have undergone adiabatic spin rotation, they travel through a collimator and get implanted into a material in the center of the NMR magnet. The samples studied in this thesis consist of a cubic lattice NaF crystal and several Room Temperature Ionic Liquids (RTIL). The liquid samples were placed onto a substrate, mounted on a retractable ladder that was moved into the atom beam path. Shimming coils on the outside of the detection chamber shape the field in the centre
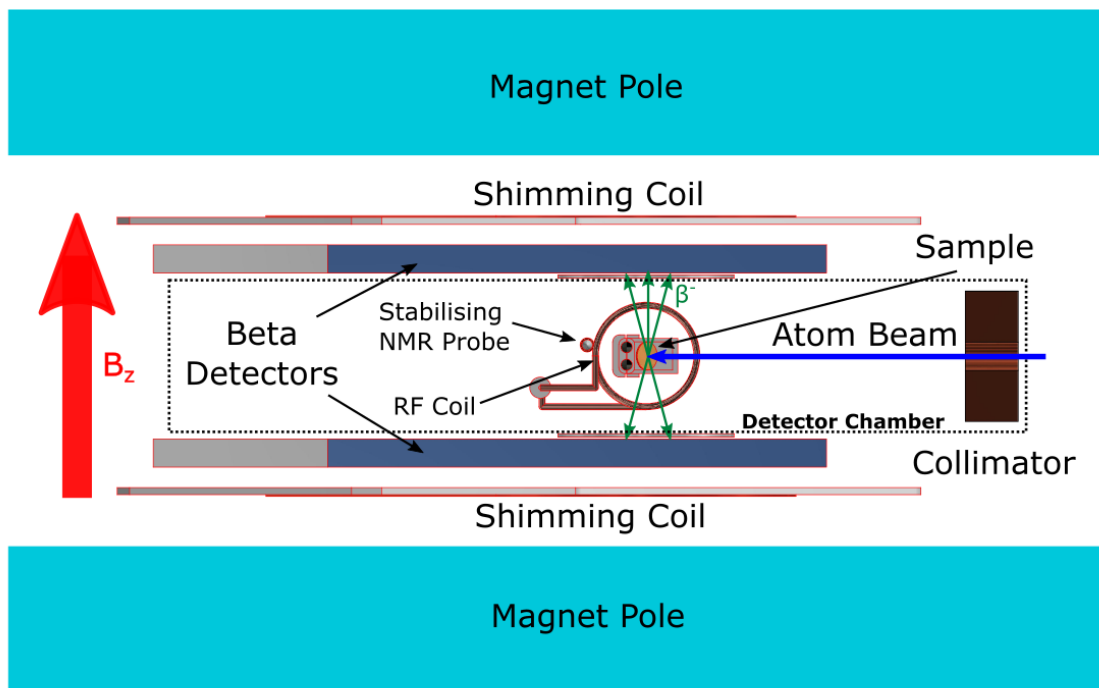
FIGURE 4.10: Schematic of the VITO's NMR detection setup.

of the NMR magnet such that it is homogenous in all three axes across the sample volume.

β decay was observed by two pairs of detectors placed on either side of the sample in the axis of the field, located outside the detector chamber. Each detector pair consisted of a thin 2 mm organic scintillator and a thicker 6 mm organic scintillator with silicon photo-multipliers (SiPMs) connected at one end. A thin "β-window" of 500 μm thick aluminium foil separated the detectors from the chamber vacuum. The opening angle of each detector was $\approx 35°$, corresponding to a solid angle coverage of ≈ 10 %.

The sample was surrounded by an solenoid "RF coil" 30 mm in diameter, with the field

orientated along the Y axis (into the page in Fig. 4.10). In order to implant the beam into the sample, the coil has a central space 16 mm in diameter (chosen such that the two coil segments form a Helmholtz configuration) for the beam to pass though, see Fig. 6.17. The RF is applied to the sample by the coil which, when in resonance, destroys the polarisation and thus β-decay asymmetry observed by the detectors. Located behind the RF coil is a smaller stabilising NMR probe. This is a small glass vial filled with water and surrounded by a small RF coil, on which pulsed NMR is performed. The pulsed NMR signal allows calculation of the exact magnetic field at the time of measurement. This stabilising probe is used to control temporal drifts in the NMR magnet, as described in Sec. 6.3.

4.4.6   Data Acquisition

The data collection was controlled by a multi-channel scalar program, referred to as MCP. A diagram of the data acquisition and control system is shown in Fig. 4.11. MCP controlled the offset voltage sent to the KEPCO x100 amplifier for hfs scans and NMR measurements, see Sec. 4.4.2, as well as the applied RF frequency during NMR scans. A hardware shutter to block the polarising laser was also controlled by the program. This would allow scans with the laser blocked to establish the background β-decay asymmetry level. Measurements were laid out into two "tracks" within the program. The first track would record β decay with the laser shutter open, while the second would record β decay with laser shutter closed. Fewer measurement points were taken during the second track in order reduce the time a scan would take.

Timing signals from all four β detectors passed through an analogue to digital converter (ADC), and were sent as NIM signals to input scalars for MCP. In parallel the NIM signals from the ADC, left and right, were passed through a logic timing coincidence module. A time window of 100 ns was used as the coincidence condition, with the resulting signals
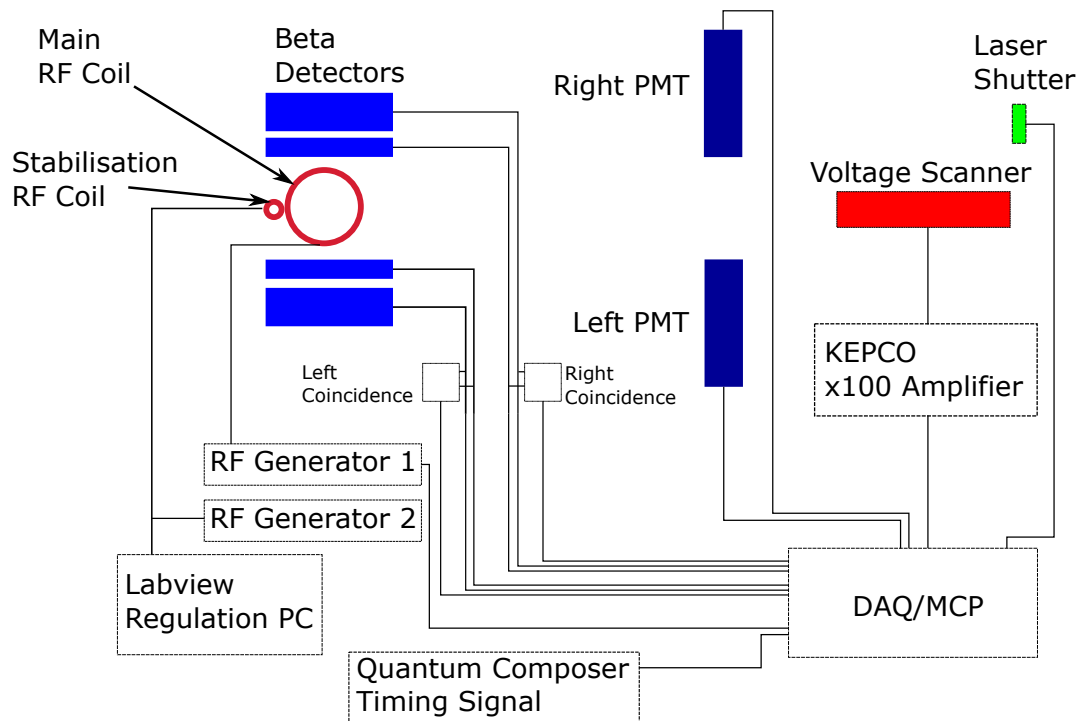
FIGURE 4.11: Wire diagram of VITO's data acquisition and control system.

(left and right coincidence) also sent to input scalars for MCP. In the data shown in Sec. 6, the β-decay asymmetry was measured by comparing the left and right coincidence signals.

To co-ordinate the ISOLDE beamgate/RFQ with the data acquisition system, a delay and gate generator from Quantum Composers was utilised [105]. The generator would control the length of time the beamgate was open, synchronising this with the data acquisition and the proton pulse signal from ISOLDE. If the RFQ was being utilised, the accumulation/release times of the device were also controlled by the delay and gate generator.

The magnet regulation was controlled by a separate computer close to the beamline.

This used a custom built LabView program to operate a second RF generator connected to the stabilising RF coil. The output FID signal from the stabilising NMR probe was read by the computer and used as to compute the magnetic field for input into a PID loop. If the measured magnetic field did not match the value set in the program, the computer would send a signal to turn a motor attached to an adjustable resistor connected in parallel with the magnet power supply. This would adjust the current flowing through the magnet and hence change the magnetic field to the desired value.

5 Laser assisted decay spectroscopy of ^{180,182}Au

The previously-known α-decay data for ^{180}Au stem from the studies at the SHIP velocity filter by Keller *et al*. [33] and from the GSI on-line mass separator, by Wauters *et al*. [34]. Both studies used complete-fusion reactions to produce ^{180}Au, thus several other nuclides originating from different evaporation channels (xn, px, and α,xn) were implanted in the detection system in both cases, even after the use of respective separators. This limited the measurements of decay properties from such mixed samples. In the SHIP investigation the authors attributed a single E_α = 5685(10) keV decay to ^{180}Au and deduced the lower limit of α-decay branching ratio, $b_\alpha(^{180}$Au$)$ >1.8%[1]. However, an α decay of this energy was not observed by the authors of work [34], this will be commented on this later in the text. Instead, at least seven α decays were seen for ^{180}Au, but only three of them (5497(10), 5611(10) and 5648(10) keV) were placed in the tentative decay scheme, see Fig. 10 in [34]. Four γ rays (36.5, 41.5, 118 and 195 keV) were seen in coincidence with these α decays. The present study contains $\sim$ 10 times more statistics than the study by Wauters *et al*. which, in combination with the purity of the sample provided by the laser ionization, has allowed us to derive a more detailed decay scheme for ^{180}Au.

---

[1]The derivation of this value in the SHIP study relied on the α-decay branching ratio of the daughter isotopes ^{180}Pt, $b_\alpha(^{180}$Pt$)$= 0.3%, only measured with a precision of a factor of 3-5, as determined in an earlier study [106]. This uncertainty determines the uncertainty of the lower limit value of $b_\alpha(^{180}$Au$)$ from SHIP, the latter was however not quoted in the original work.

5.1 Calibration of detectors

5.1.1 Silicon detectors

The sum singles α-decay energy spectrum registered in Si1 and Si2 is shown in Fig. 5.4(a). The spectrum shows the purity of the collected sample, with the strongest groups of α decays belonging to ^{180}Au and its β-decay daughter ^{180}Pt. It is important to note here that the α-decay energies quoted for ^{180}Au in Fig. 5.4(a), and further in the text and in the decay scheme are the values after a small correction ($\approx$ 1-6 keV) for α + conversion electrons summing in the silicon detectors, implemented based on GEANT4 simulations, as discussed in Sec. 5.2.4.

Due to the relatively low resolving power of the GPS, a weak α-decay peak from the neighbouring mass ^{179}Au is also seen in the spectrum, with $\sim$ 20,000 times lower intensity. ^{180}Hg and its α-decay daughter ^{176}Pt are also weakly present, as products from the decay chain of surface-ionized nuclide ^{180}Tl, their decays aid in the validation of the calibration procedure outlined below.

The α decay of ^{180}Pt (5140(10) keV [107], 5139(19) keV [108]) would be the most appropriate as one of the calibration points for the energy calibration of the silicon detectors. However, as these measurements are from over 50 years ago, α decays from ^{178}Pt (5446(3) keV [109]) and ^{179}Au (5848(5) keV [106]) were used, taken in short measurements at respective GPS mass settings before the main run at $A = 180$, and ^{180}Hg (6119(4) keV [110]) weakly present in the $A = 180$ α-decay spectrum. The relevant data are shown in Fig. 5.1. Based on this calibration procedure, an α-decay energy of 5160(5) keV was deduced for ^{180}Pt which deviates from the literature value by $\approx$ 20 keV.

This shift likely stems from the difference in α-decay energies used for calibration. In Wauters study, the $E_\alpha = 5458$ keV decay of ^{178}Pt was used for calibration, 12-keV higher than the presently-accepted literature value of 5446(3) keV [109]. This likely explains the
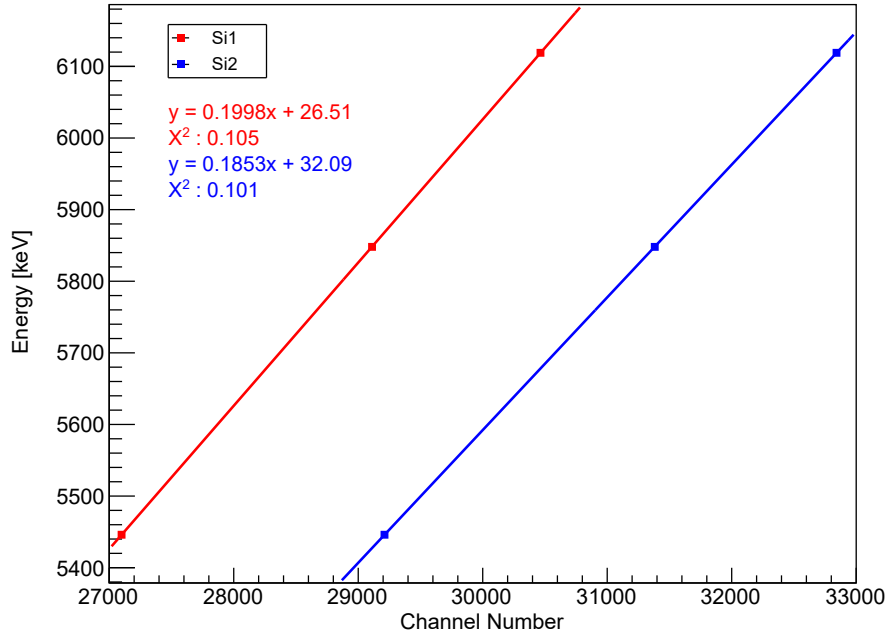
FIGURE 5.1: Energy calibration of the Si1 (red) and Si2 (blue) detectors, using α decays from ^{178}Pt, E_α = 5446(3) keV, ^{179}Au, E_α = 5848(5) keV and ^{180}Hg, E_α = 6119(4) keV

discrepancy in $E_\alpha(^{180}$Au) between the two studies. As will be shown below, there is a small shift in the α-decay energies of ^{180}Au ($\approx$ 7 keV) compared to the previous study by Wauters *et al.* [34]. For example, in Fig. 5.4(a) the highest-energy α decay attributed to ^{180}Au is observed at 5639(5) keV, compared to E_α = 5648(5) keV quoted in [34]. Furthermore, the α + conversion electron summing, discussed in Sec. 5.2.4, can also lead to a small 'apparent' increase of the original α-decay energies for most of the peaks of ^{180}Au. Most probably, this effect was not considered in study [34], while it is included in the present work.

5.1.2   Germanium detectors

Both of the Ge detectors were calibrated using sources of ^{152}Eu (7.953 kBq on 10/09/2014), ^{137}Cs (18.519 kBq on 10/09/2014), ^{133}Ba (6.686 kBq on 10/09/2014) and ^{60}Co (0.716 kBq on 10/09/2014) sources. Figure 5.2(a) shows the energy of detected γ rays as a function of channel number for each detector, fitted with linear functions. An absolute efficiency curve of the LEGe detector from the aforementioned calibration sources, is shown in Fig. 5.2(b). The efficiency data is fitted with a crystal ball function [111].

5.1.3   Prompt timing windows

In the final analysis of the α-γ coincident data, it was necessary to define a prompt time window between the registration of an α particle in one of the Si detectors and a γ ray measured in the LEGe. The time gate removes time-random coincident events, whilst keeping true events for the relevant analysis. The time window was chosen by plotting the time distribution of the known 5640-36.5 keV α-γ coincidence in the fine structure of ^{180}Au. The results are shown in Fig. 5.3. A prompt timing condition of $0 < \Delta t < 250$ ns was chosen for the investigation of α-γ coincidences in the following sections.
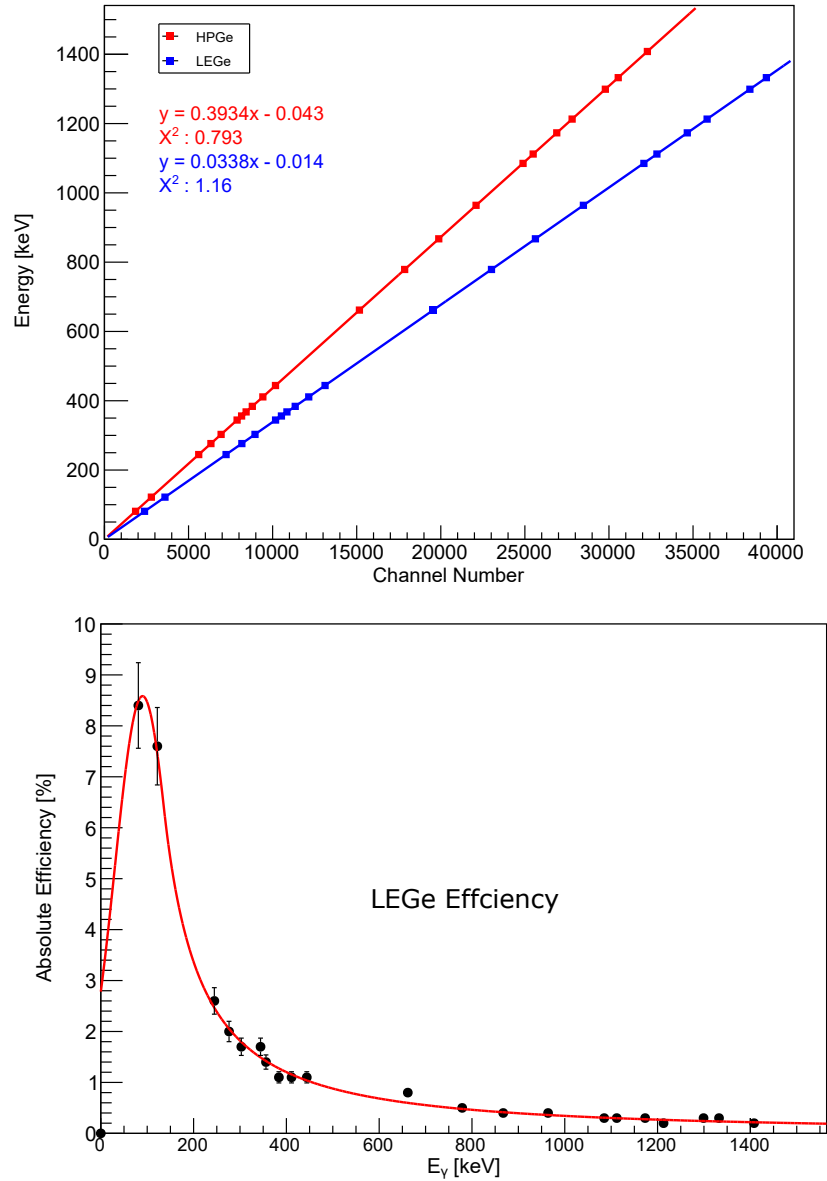
FIGURE 5.2: (a) Energy calibration of the HPGe (red) and the LEGe (blue), fitted using a linear relationship. (b) Absolute efficiency curve of the LEGe detector fitted using a crystal ball function [111].
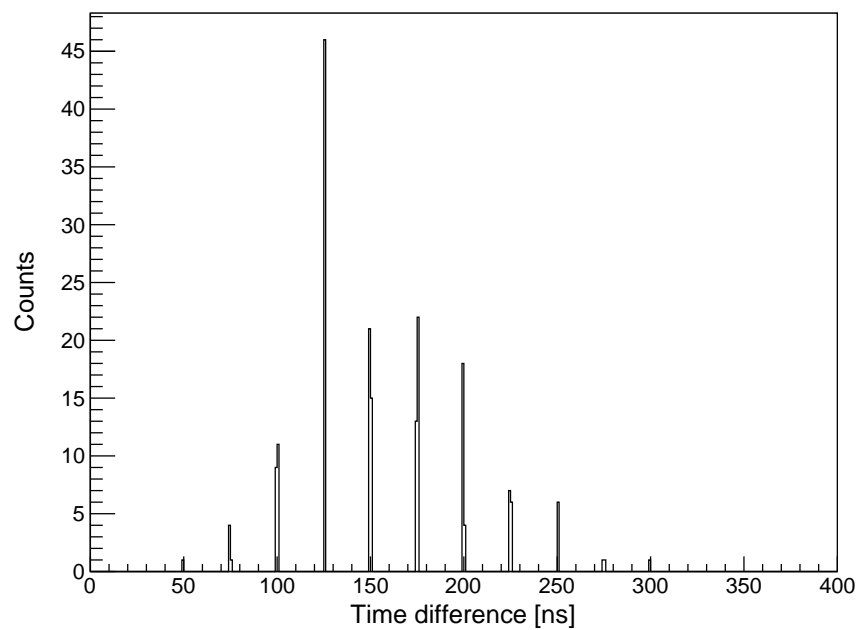
FIGURE 5.3: Time difference between α particle and γ-ray belonging to the 5640-keV and 36.5-keV fine structure decay.

5.2 α decay of ^{180}Au

5.2.1 α-γ coincidences for ^{180}Au

An $\alpha - \gamma$ coincidence matrix for prompt γ transitions registered in the LEGe following α decays measured in Si1/Si2, is shown in Fig. 5.4(b). A prompt time gate of $\Delta t(\alpha - \gamma) < 250$ ns was used. A projection on the Eγ axis for the events within the blue-shaped region in Fig. 5.4(b), which is relevant for ^{180}Au, is shown in Fig. 5.4(c). It contains a number of low-energy transitions with energies up to 218 keV, along with a large number of iridium $K_{\alpha,\beta}$ x rays. The γ rays at 36.5(3) keV, 41.5(3) keV, 118.0(3) keV and 195.7(5) keV were previously reported by Wauters et al. [34], while the transitions at 89.1(4), 108.9(4), 130.3(4), 159.9(5), 177.8(4), 205.2(5) and 218.8(5) keV are newly observed.

Several f.s. α decays of ^{180}Au were distinguished by gating on coincident γ rays from Fig. 5.4(c) and were placed in the decay scheme shown in Fig. 5.5, based on the arguments presented further in the text. Figure 5.6 shows the respective α-decay projections for some of these γ rays.

The 5639(7)-keV α decay is seen in coincidence with a 36.5-keV γ ray, see Fig. 5.6(a). This establishes an excited state at 36.5(3) keV in ^{176}Ir as depicted in the decay scheme shown in Fig. 5.5. Based on this α-γ coincident pair, we define the full energy $Q_{\alpha,tot,ref} = Q_{\alpha}(5639 \text{ keV}) + E_{\gamma}(36.5 \text{ keV}) = 5804(7)$ keV, which will be used throughout the text.

An α decay at 5598(8) keV is seen in coincidence with both the 41.5-keV and the 36.5-keV γ rays, see Fig. 5.6(b). The $Q_{\alpha,tot} = Q_{\alpha}(5598 \text{ keV}) + E_{\gamma}(41.5 \text{ keV}) + E_{\gamma}(36.5 \text{ keV}) = 5803(8)$ keV matches well with $Q_{\alpha,tot,ref}$. This proves that the 41.5-keV and 36.5-keV γ rays form a γ-ray cascade following the 5598 keV α decay, establishing a level at 78.0(4) keV as was already proposed by Wauters *et al.* [34].

By gating on the 118.0-keV γ ray, an α decay at $E_{\alpha} = 5485(10)$ keV is observed, see Fig. 5.6(e). Due to the matching of $Q_{\alpha,tot} = Q_{\alpha}(5485 \text{ keV}) + E_{\gamma}(118 \text{ keV}) + E_{\gamma}(41.5 \text{ keV})$
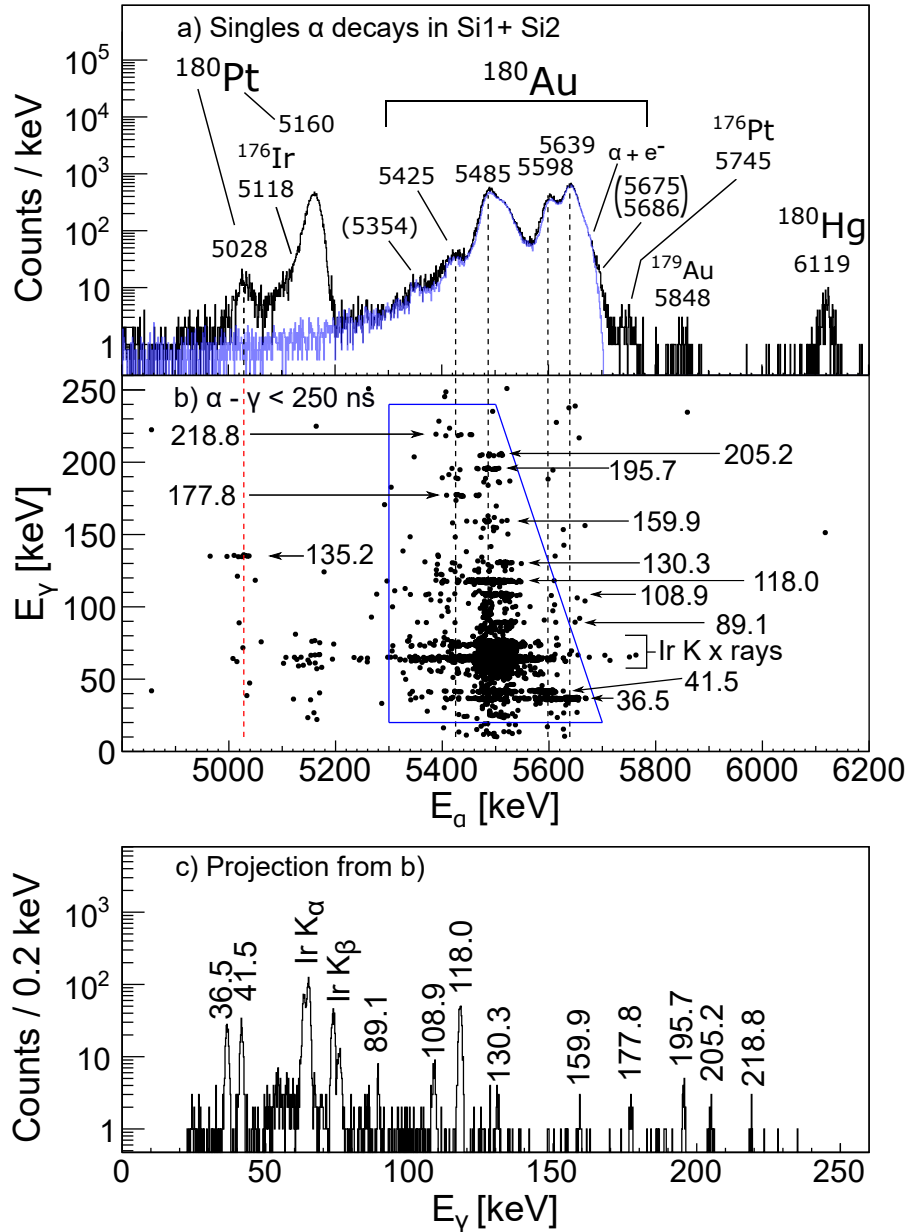
FIGURE 5.4: (a) Singles α-decays spectrum registered in Si1 and Si2 at A = 180; their peaks marked with their energies in keV. The quoted α-decay energies for ^{180}Au include the correction for α + conversion electrons summing in silicon detectors. The overlapped blue histogram is the result of GEANT4 simulations, see Sec. 5.2.4 for details. (b) $\alpha - \gamma$ coincidences for α decay from Fig. 2(a) for γ-ray energies up to 250 keV with a coincidence timing gate $\Delta t(\alpha - \gamma) = 250$ ns. (c) Projection of the γ-ray axis from Fig. 2(b) of the region indicated by the blue lines on Fig. 2(b).
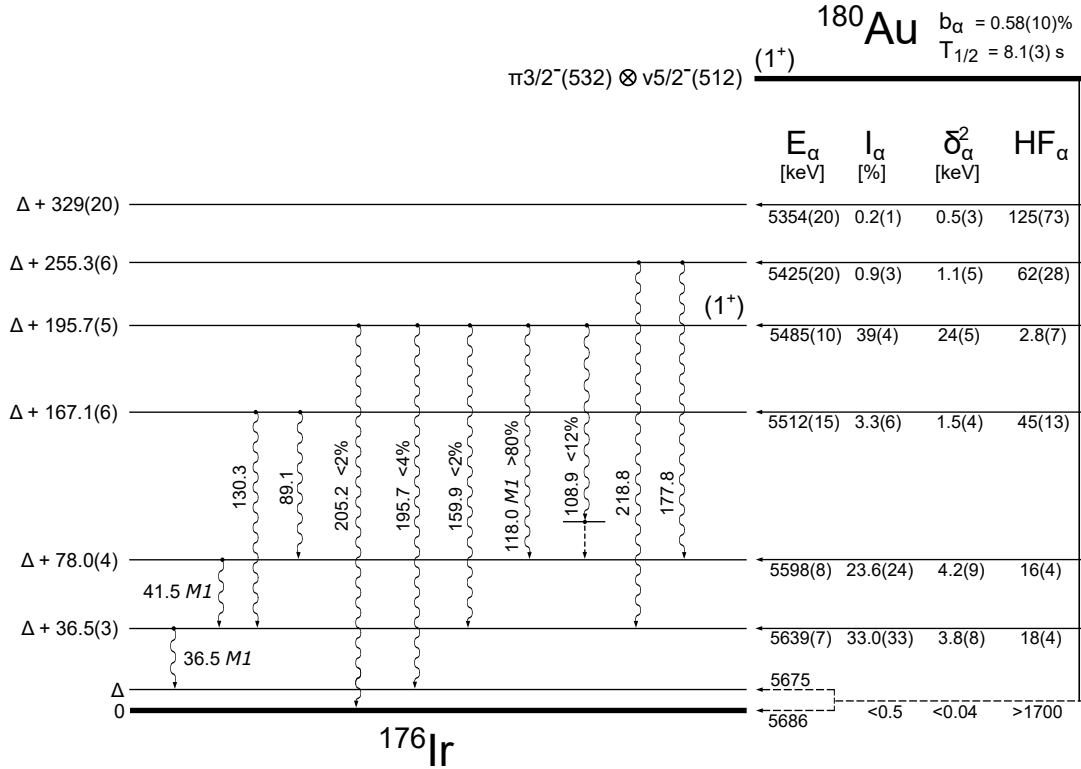
FIGURE 5.5: A decay scheme for ^{180}Au proposed in this study. The α-decay energies E_α, relative intensities I_α, reduced α-decay widths δ_α^2 and hindrance factors HF_α for the parent isotopes ^{180}Au and levels and transitions in the daughter ^{176}Ir deduced in this work are shown alongside some previously-known data from Ref. [34]. The half-life value of 8.1(3) s is taken from [112]. Hindrance factors were extracted relative to the average value of $\delta_\alpha^2 = 66(6)$ keV for the unhindered α decays from ^{179,181}Au, see Sec. 5.6.2 for details. A value of $\Delta = 9.5(7)$ keV is discussed in Sec. 5.2.2. The 5675-keV and 5686-keV α decays are shown by a dashed line as tentative.

+ E_γ(36.5 keV) = 5806(10) keV to the $Q_{\alpha,tot,ref}$, the 118 keV transition is assigned in a cascade with the 41.5 keV and 36.5 keV γ rays. The 195.7 keV γ ray, which is also in

coincidence with the 5485-keV decay [see Fig. 5.6(g)] is placed as a crossover transition to the same state as fed by the 36.5 keV decay. This confirms a level at 195.7(5) keV in ^{176}Ir, which has been proposed in Ref. [34]. Within the experimental energy uncertainties, the weak 159.9-keV transition seen in Fig. 5.4(c) matches well to the decay between the 195.7- and 36.5-keV levels, thus it was also placed in the decay scheme in Fig. 5.5.

The 5485-keV α decay is also seen in coincidence with the 108.9-keV γ ray, see Fig. 5.6(d). Very tentatively, this observation might suggest that an $\approx$ 9 keV transition should exist in a cascade with the 108.9 keV decay, but it would be unobserved in our experiment. We note that the 5485-keV peak in Fig. 5.6(d) has a higher-energy tail, which tentatively might be attributed as being due to the summing of the 5485-keV transition with the conversion electrons originating from this 9-keV decay, apart of summing with electrons from 36.5- and 41.5- keV decays, Sec. 5.2.4. We tentatively placed the 108.9-keV decay as shown in Fig. 5.5, followed by the yet unobserved 9 keV decay, which is shown by a dashed arrow as tentative.

An α decay of 5512(15) keV is in coincidence with the 89.1- and 130.3-keV γ rays see Fig. 5.6(c) and see Fig. 5.6(f). The $Q_{\alpha, tot} = Q_{\alpha}(5512 \text{ keV}) + E_{\gamma}(89.1 \text{ keV}) + E_{\gamma}(41.5 \text{ keV}) + E_{\gamma}(36.5 \text{ keV}) = 5804(15)$ keV is in good agreement with $Q_{\alpha, tot, ref}$. Thus, the 89.1-keV γ ray is placed in cascade with the 41.5- and 36.5-keV γ rays, establishing a level at 167.1(6) keV. The 130.3-keV γ ray is assigned as a crossover transition feeding the 36.5-keV level.

A weak α decay at 5425(20) keV is seen in the singles α-decay spectrum in Fig. 5.4(a). It is also seen in coincidence with the 218- and 177.8-keV γ rays, see Fig. 5.6(i). Since the $Q_{\alpha, tot} = Q_{\alpha}(5425 \text{ keV}) + E_{\gamma}(218.8 \text{ keV}) + E_{\gamma}(36.5 \text{ keV}) = 5803(20)$ keV is in agreement with $Q_{\alpha, tot, ref}$, the 218.8-keV γ ray is placed in cascade with the 36.5 keV, establishing a level at 255.3(6) keV. 177.8-keV γ ray is proposed as a transition to the 78-keV level as the γ-ray energy difference 218.8(5)-177.8(5)=41.0(7) keV fits well to the energy of 41.5(3)-keV decay from this level.

In Fig. 5.4(a), a weak α decay at 5354(20) keV, is seen in coincidences with Ir $K_{\alpha,\beta}$
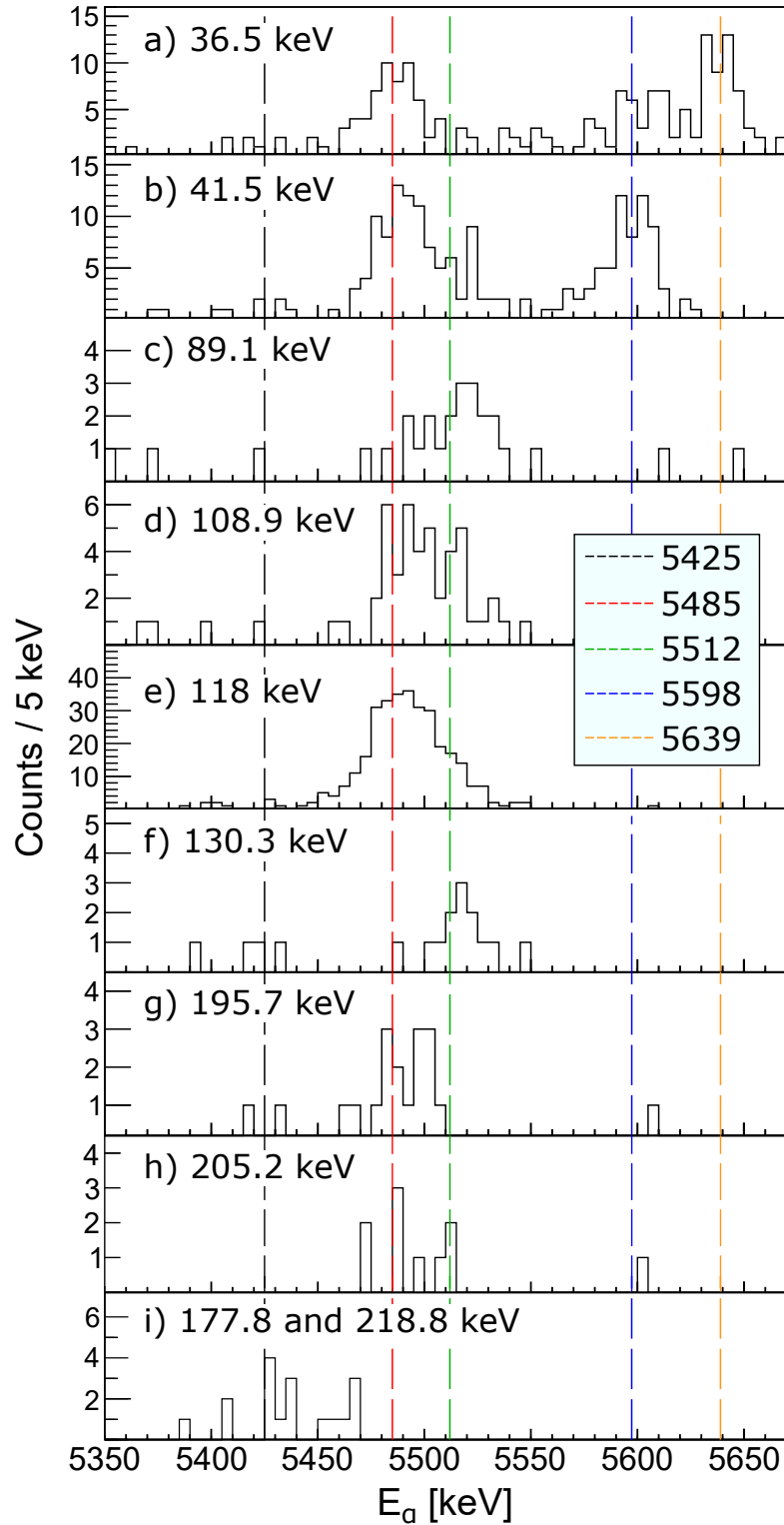
FIGURE 5.6: Projections on the α-energy axis from α-γ coincident plot in Fig. 5.4(b), using a ± 1.5 keV gate encompassing the γ ray indicated in the top left of each projection.

x rays, see Fig. 5.4(b). The latter fact confirms that the 5354-keV decay originates from ^{180}Au. The Q_α-analysis requires the presence of an excited state at E* = 329(20) keV in ^{176}Ir, but no coincident γ-ray transition could be identified following this weak α decay. The number of Ir $K_{\alpha,\beta}$ x rays in coincidence with this decays suggests that such a transition (or a cascade of them) should be strongly converted, possibly implying its (their) M1 and/or E0 component and also possibly proceeding via some known lower-lying states. This α decay and respective excited state were added to the scheme in Fig. 5.5.

For completeness, we mention that in Fig. 5.4(a), two α decays attributed to ^{180}Pt have been identified; the 5160(5) keV (5139 keV and 5140 keV in previous studies [107, 108]) and a f.s. α decay at 5028(7) keV, in coincidence with a γ ray of 135.1(5) keV feeding to the known 2$^+$ state in the daughter nucleus ^{176}Os.

5.2.2 Determination of the Δ value in the decay scheme of ^{180}Au

Finally, as shown in Figs. 5.4(b) and 5.6(h), the 5845-keV decay is also seen in coincidence with the 205.2-keV γ ray. In this case the $Q_{\alpha,tot} = Q_\alpha(5485 \text{ keV}) + E_\gamma(205.2 \text{ keV}) =$ 5815(10) keV, thus is $\approx$ 11 keV higher than the $Q_{\alpha,tot,ref}$ value, albeit with a large uncertainty. Furthermore, the energy difference for the 205.2(5)- and the 195.7(5)-keV γ rays which follow the 5485-keV decay determines a more precise Δ = 9.5(7) keV, shown in the decay scheme in Fig. 5.5. Such a scenario supports the decay scheme proposed by Wauters *et al*. in Ref. [34], where Δ was introduced (see Fig. 10 in [34]), albeit with no prescribed value or any explanation of why it was introduced.

An attempt was also made to derive an estimate of Δ based on a comparison of directly measured masses of ^{180}Au and ^{176}Ir. To date, the most precise mass excess of $m(^{180}$Au) = -25627.25(4.95) keV/c^2 was reported by the ISOLTRAP Penning trap study [113]. This value agrees with, but is much more precise, than a mass excess of -25612(28) keV/c^2 from direct measurements at the Experimental Storage Ring (ESR) at GSI [114]. The latter work

also published a mass excess $m(^{176}Ir) = $ -33839(28) keV/c^2. Based on a combination of ISOLTRAP-ESR measurements for a pair of ^{180}Au - ^{176}Ir, a value of $Q_\alpha(^{180}$Au$) = 5787(29)$ keV can be derived. Within a rather large experimental uncertainty, dominated by the uncertainty of the ESR measurements, this value fits well to $Q_\alpha(^{180}$Au$) = 5802(40)$ keV, if both parent and daughter masses are taken from the ESR data.

Within their large uncertainties, both above-mentioned $Q_\alpha(^{180}$Au$)$ values match well to the $Q_{\alpha, tot, ref} = 5804$ keV. This analysis also establishes that the Δ value should not exceed ≈ 20 keV therefore the deduced value of $\Delta = 9.5(7)$ keV supports this estimate.

The derivation of Δ value leads to an important conjecture that, based on the proposed decay scheme and $Q_{\alpha,tot}$ analysis, two decays of ^{180}Au with the energies ≈ 5675 and ≈ 5686 keV could be expected, feeding respectivley to the $\Delta = 9.5(7)$-keV state and the lowest state in ^{176}Ir. Indeed, a small higher-energy tail of the 5639-keV peak, extending up to ≈ 5690 keV is observed in Fig. 5.4(a), which might include these two α decays. This possibility will be further discussed in Sec. 5.2.4.

5.2.3   Multipolarities of γ rays in ^{176}Ir

The 36.5 and 41.5 keV γ rays

All γ-ray transitions following the α decay of ^{180}Au are prompt, which limits their multipolarities to E1, M1 or E2. In our study, a more precise determination of multipolarities could be performed for some of the transitions based on the deduced values of total internal conversion coefficients (α_{tot}). For a particular γ ray, $\alpha_{tot,exp}$ can be deduced from:

$$\alpha_{tot} = \frac{N_\alpha \varepsilon_\gamma}{N_{\alpha\gamma}} - 1, \tag{5.1}$$

where N$_\alpha$ is the number of singles α decays from Fig. 5.4(a), N$_{\alpha\gamma}$ is the number of α - γ coincidence events from Fig. 5.4(b) and ε_γ is the γ-ray detection efficiency at a given

energy. To evaluate the α_{tot}(36.5 keV), only events in coincidence with the 5639 keV α decay are considered, in order to exclude feeding to the 36.5-keV level from other states. By using Eqn. 5.1, an $\alpha_{tot,exp}$(36.5 keV) = 22(4) is deduced which agrees within the experimental uncertainty with the theoretical $\alpha_{tot,th}$(M1) = 20.59 calculated using BrIcc [115], see Table 5.1. Thus, the 36.5-keV γ ray is assigned a pure M1 multipolarity.

TABLE 5.1: Comparison of total experimental ($\alpha_{tot,exp}$) and theoretical ($\alpha_{tot,th}$) conversion coefficients for listed γ decays. The theoretical values were calculated with BrIcc [115].

E_γ [keV]	α_{tot}(exp)	α_{tot}(E1)	α_{tot}(M1)	α_{tot}(E2)
36.5(3)	22(4)	1.212	20.59	49.94
41.5(3)	17(4)	0.853	14.10	265.5
118.0(3)	3.4(6)	0.2616	3.812	2.376

By considering events in coincidence with the 5598 keV α decay, it was possible to deduce a value for $\alpha_{tot,exp}$(41.5 keV). As the 41.5-keV γ ray is in cascade with the 36.5-keV γ ray, it should have the same intensity (after correcting for conversion and γ ray efficiency). A value of $\alpha_{tot,exp}$(41.5 keV) = 17(4) was deduced, which agrees within uncertainty with the theoretical value of $\alpha_{tot,th}$(M1) = 14.1 (see Table 5.1). Therefore, the 41.5-keV γ ray is also assigned a pure M1 multipolarity.

118 keV γ ray

In Fig. 5.4(a) several f.s. α decays have been identified between 5450 and 5550 keV. Of the γ rays seen in coincidence with this α-decay structure, the 118 keV γ-ray transition has the largest intensity (see Fig. 5.4(c)). A lower limit on α_{tot}(118 keV) can be calculated by assuming an M1 multipolarity (thus the largest internal conversion for γ rays at these energies) for the remaining γ-ray transitions (130.3, 89.1, 108.9, 159.9 and 195.7 keV) in

coincidence with the α decays in the 5450-5550 keV region. Based on Eqn. 5.1 the number of α decays preceding each of the γ rays listed above was deduced, and subtracted from the total number of α decays in the 5450-5550 keV region. The remaining number gives a lower limit for the number of α decays, N_α(5450-5550 keV), which are followed by a 118 keV γ ray or associated conversion electron.

Placing this N_α(5450-5550 keV) number back into Eqn. 5.1, an α_{tot}(118 keV) $\geqslant 3.4(6)$ was deduced, which lies between the theoretical $\alpha_{tot,th}$(M1) = 3.812 and $\alpha_{tot,th}$(E2) = 2.376 values. As this is a lower limit on α_{tot}(118 keV), this implies that the 118 keV γ ray is predominantly M1 with a possibility for a small E2 admixture. This likely means that the parities of the states from which the 118-keV and 41.5 keV γ rays originates are the same. This would restrict the 159.9-keV and 195.7-keV γ rays to multipolarities of either M1 or E2, based on the parity of their state of origin and their prompt nature, but based on our data a more precise determination is not possible.

5.2.4 $\alpha - e^-$ summing in the α decay of ^{180}Au

The presence of strongly-converted 36.5-, 41.5- and 118-keV transitions, which follow most of the observed decays of ^{180}Au, leads to α + conversion electron (CE) summing in the Si1/Si2 detectors. Namely, if both the α particle and CE are registered simultaneously in the same silicon detector, both the original energy and the shape of the α-decay peak will be distorted. Depending on the intensity, multiplicity and energy of the CEs, an energy shift to higher energies, an appearance of a high-energy tail and/or appearance of an artificial peak of full α + CE energy summing might occur.

To understand these effects, GEANT4 [116, 117] simulations were performed, which included all decays of ^{180}Au. The simulations included the CEs and the relevant x rays for the 36.5-, 41.5- and 118.0-keV M1 γ-ray transitions, with the conversion coefficients deduced in the present work (see Tab. 5.1). Based on these simulations, an energy shift of

1 keV was deduced for the single-fold α + CE(36.5) summing, 2 keV for a double-fold α + CE(36.5) + CE(41.5) summing, and 6 keV for a triple-fold α + CE(36.5) + CE(41.5) + CE(118) summing. Following this procedure, the 'apparent/uncorrected' measured energies of 5640-, 5600- and 5491-keV of the main peaks of ^{180}Au in Fig. 5.4(a) were corrected, resulting in the 'true' values of 5639-, 5598- and 5485-keV, used in the text and in the decay scheme.

A very good agreement of the simulated (blue histogram) and measured energy spectra for ^{180}Au, by starting from the corrected α-decay energies, is shown Fig. 5.4(a), which confirms the correctness of the applied procedure. The intensities of α decays of ^{180}Au shown in the decay scheme were taken from the GEANT simulations. A very important fact, relevant to the discussion of the value of Δ and hindrance factor values in Sec. 5.6.2, is an experimental observation of a small high-energy tail of the 5639-keV α-decay peak in Fig. 5.4(a) extending up to 5690 keV.

Based on the GEANT4 simulations, most of this tail can be understood as being due to the full α + CE summing energy of the dominant L-shell conversion electron from the 36.5-keV γ ray with the 5639-keV decay, which gives an energy of 5662 keV, while the 4 times lower M-shell conversion summing peak has an energy of 5672 keV. Therefore, if real, a small excess of events in the region of 5680-5690 keV could indicate the presence of 5675- and/or 5686-keV decays of ^{180}Au, mentioned in Sec. 5.2.1. By subtracting the measured and simulated spectra, an upper limit of $I_\alpha \leq 0.5\%$ be established for the combined intensity of these decays, which are schematically shown as a tentative single α decay in Fig. 5.5; they will be further discussed in Sec. 5.6.2.

To conclude the discussion on the α + CE summing, we also note that the 5685(10)-keVα decay, proposed for ^{180}Au by Keller *et al*. [33], can now be fully understood as being due to this summing effect. In their experiments, the ^{180}Au nuclei were implanted to a depth of a few micrometers into the silicon detector, therefore the degree of α + CE summing was much higher than in the present study [118]. We performed GEANT4 simulations for the

SHIP-like conditions, which confirmed that the dominant full-energy (5598/5639 keV) + CE(36.5, 41.5 keV) summing leads to a well-pronounced peak at $\approx$ 5685 keV, in agreement with the SHIP data.

5.3 Half-life and α-decay branching ratio for ^{180}Au

To determine the half-life of ^{180}Au, the grow-in/decay-out method, as described in detail in Ref. [119], was applied. The time distribution of the α decays in the energy region 5300-5800 keV from Fig. 5.4(a), is presented in Fig. 5.7. An exponential decay curve is fitted in the 5.1 s decay time interval between 30.89-36 s, from which a half-life of $T_{1/2} = 7.2(5)$ s is derived. Within two sigma, our result in agreement with the previously-reported value of 8.1(3) s from Ref [112]. The precision of the half-life determination in our study is limited by the short time interval (5.1 s) used in this analysis. This was due to an unstable proton pulse implantation cycle occurring before the beamgate was closed at 30.89 s.

The α-decay branching ratio can be derived by comparing the number of α decays from ^{180}Au and its β-decay daughter ^{180}Pt in Fig. 5.4(a), as shown in Eqn. 2.

$$
\begin{aligned}
b_\alpha(^{180}Au) &= \frac{N_\alpha(^{180}Au)}{N_{tot}(^{180}Au)}, \\[2mm]
&= \frac{N_\alpha(^{180}Au)}{N_\alpha(^{180}Au) + N_{tot}(^{180}Pt)}, \\[2mm]
&= \frac{N_\alpha(^{180}Au)}{N_\alpha(^{180}Au) + \frac{N_\alpha(^{180}Pt)}{b_\alpha(^{180}Pt)}},
\end{aligned}
\tag{5.2}
$$
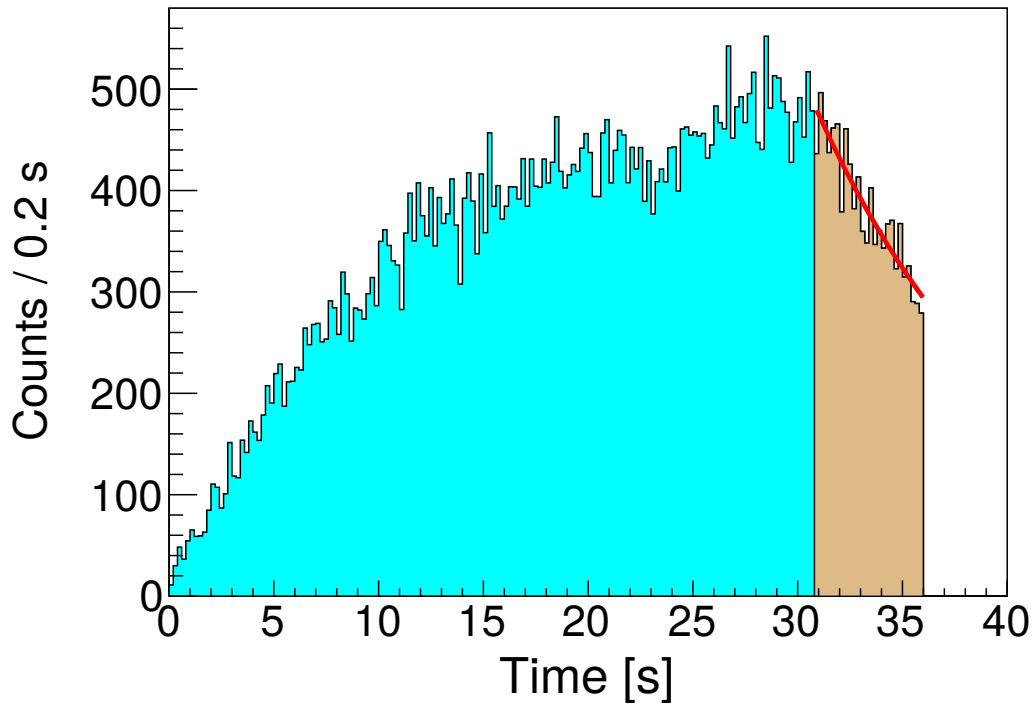
FIGURE 5.7: The time distribution for α decays of ^{180}Au as seen in Si1 and Si2 at the implantation position. A sequence of implantation-decay cycles was implemented in which the beam was implanted for 30.89 s (shaded in blue) followed by the closing of the ISOLDE beamgate for 5.11 s (shaded in brown). At the end of each 36 s cycle, the Windmill was rotated and a fresh foil placed into the implantation position. The decay part of the distribution was fitted with an exponential function, from which a value of $T_{1/2}(^{180}Au) = 7.2(5)$ s was deduced. By extrapolating the decay curve beyond 36 s, one can estimate the amount of ^{180}Au activity removed by the Windmill movement, which is needed for the $b_\alpha(^{180}Au)$ determination.

Where $b_\alpha(^{180}\text{Pt}) = 0.52(5)\%$ [120] and N_{tot} the total number of a given isotope produced during the experiment. Direct production of ^{180}Pt is not possible in the experiment, as a negligible amount of ^{180}Pt is surface ionized and it is not produced by laser ionization with the lasers tuned to the gold ionization scheme. This was demonstrated during the studies of neighbouring masses: when the lasers were tuned off the gold ionization scheme, no platinum α decays were observed. Thus, all the ^{180}Pt present in the spectrum can only originate from β-decay of implanted ^{180}Au.

By direct application of Eqn. 5.2 (without any corrections, see below) we can determine an upper limit of $b_\alpha(^{180}\text{Au}) < 2.2(2)$ % This value is larger than the lower limit of $> 1.8\%$ deduced at SHIP [33]. The deduced upper limit has to be corrected for the periodical movement of Windmill which removed the activity that was implanted into the foil at the end of each supercycle. Due to the presence of Si3 and Si4 located in the decay position, see Fig. 4.5, we can attempt to approximate the activity removed by the rotation of the wheel. For ^{180}Au, the decay fraction removed can be extrapolated from fitting the decay part of the implantation spectrum, to obtain the total number of nuclei when the beamgate was closed. A decay curve is then extrapolated past the end of the super cycle at 36 s to estimate the number of ^{180}Au nuclei removed, see the green line in Fig.5.8.

The α decay of ^{180}Pt is still observed in Si3 and Si4, when the foil arrives at this position after 3 super cycles, due to its longer half-life of 56(3) s (a weighted average from ENSDF [121]). Only pure decay is observed for ^{180}Pt in Si3 and Si4, as all of the ^{180}Au has decayed by the time the implantation foil reaches this position. By using the extrapolated ^{180}Au decay curve and the ^{180}Pt Si3/Si4 spectra, we can fit a decay curve to estimate the amount of ^{180}Pt α-decay between the two implantation positions, see the red line in Fig. 5.8. From the integral of the green and red curves, we can correct the intensities of ^{180}Pt and ^{180}Au α decay, as observed in Si1/Si2 for the rotation of the Windmill movement.

A $b_\alpha = 0.58(10)\%$ was deduced for ^{180}Au using Eqn. 5.2, with the intensities of the parent ^{180}Au and daughter ^{180}Pt α decays, corrected for the Windmill movement as mentioned

above. This value is about three times lower than the lower limit on $b_\alpha(^{180}Au)$ deduced by the SHIP study.
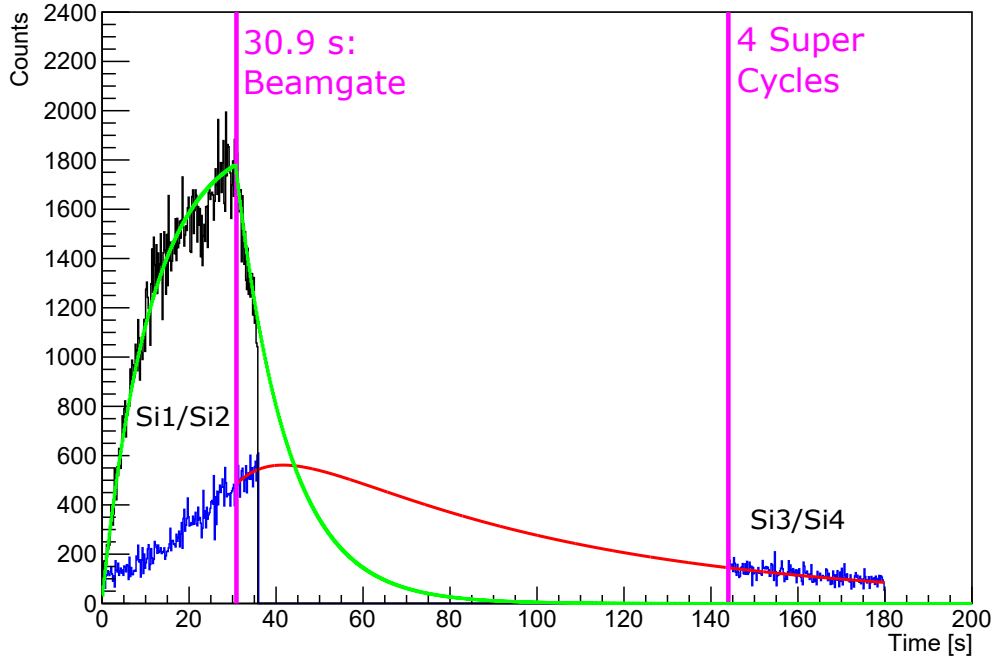
FIGURE 5.8: The time distribution of α decays from ^{180}Au as seen in Si1/2 (Black) and from ^{180}Pt (blue) from Si1/2 and Si3/4. The green line shows the extrapolated decay of ^{180}Au, using the half-life of 8.1(3) s from the from Ref [112]. The implantation foil moves in front of Si3/Si4 after 3 super cycles, indicated by the pink line. The red curve is the estimated Pt unobserved due to the windmill rotation, see text for details.

^{176}Ir, being the α-decay daughter of ^{180}Au has an α decay with $E_\alpha = 5118(8)$ keV [122]. This α decay is masked by the more abundantly produced 5160 keV α decay of ^{180}Pt, see

Fig. 5.4(a). However, as this decay branch is small ($b_\alpha(^{176}Ir)$ = 3.1(6) %) [123], this is regarded as a negligible contribution to the branching ratio calculation.

5.4 ^{180}Au β decay

Apart of α-decay measurements, the Windmill setup also allowed for the collection of γ-decay data. Figure 5.9 shows the background subtracted singles γ-ray spectrum recorded by the LEGe. As no dedicated on-line measurement of the background was performed during or after the run at A = 180, we were only able to use a background measurement taken beforehand. This explains the large background still present in Fig. 5.9, which results from γ rays produced in the actual on-line measurement at A = 180. In this spectrum, the γ rays originating from excited states in ^{180}Pt populated by β decay of ^{180}Au are labelled, identified in the previous dedicated β-decay study of ^{180}Au by Davidson *et al*. [124]. As a much higher statistics was collected for ^{180}Pt decays in [124] in comparison to our experiment, we will rely on the spin/parity assignments from that earlier work. In Fig. 5.9, one clearly sees the 153.2(1)-keV, $2_1^+ \rightarrow 0^+$ and the 257.5(1)-keV, $4_1^+ \rightarrow 2_1^+$ γ rays, with numerous other decays previously seen by [124]. No evidence for the 346.3-keV, $6_1^+ \rightarrow 4_1^+$ ground-state band transition in ^{180}Pt was observed, see Fig. 5.9.

The observed decay pattern of feeding to 2_1^+, 4_1^+ and 6_1^+ states in ^{180}Pt in our work is in agreement with the Davidson's *et al*. study, where the ratio of intensities, corrected for efficiency, is $I(153.2$ keV$)/I(257.5$ keV$)/I(346.3$ keV$) \approx 1000(31){:}233(10){:}6(2)$, see Tab. 4 of [124]. The much weaker apparent feeding to the 4_1^+ and, especially, 6_1^+ states (in respect of 2_1^+) is most probably due to the feeding from the higher-lying states, rather than directly from β decay. Because of the high value of $Q_\beta(^{180}$Au$)$=8.810(12) MeV [125], one can indeed expect some β-decay feeding to the higher-energy states, whose de-excitation is usually hampered by the Pandemonium effect.
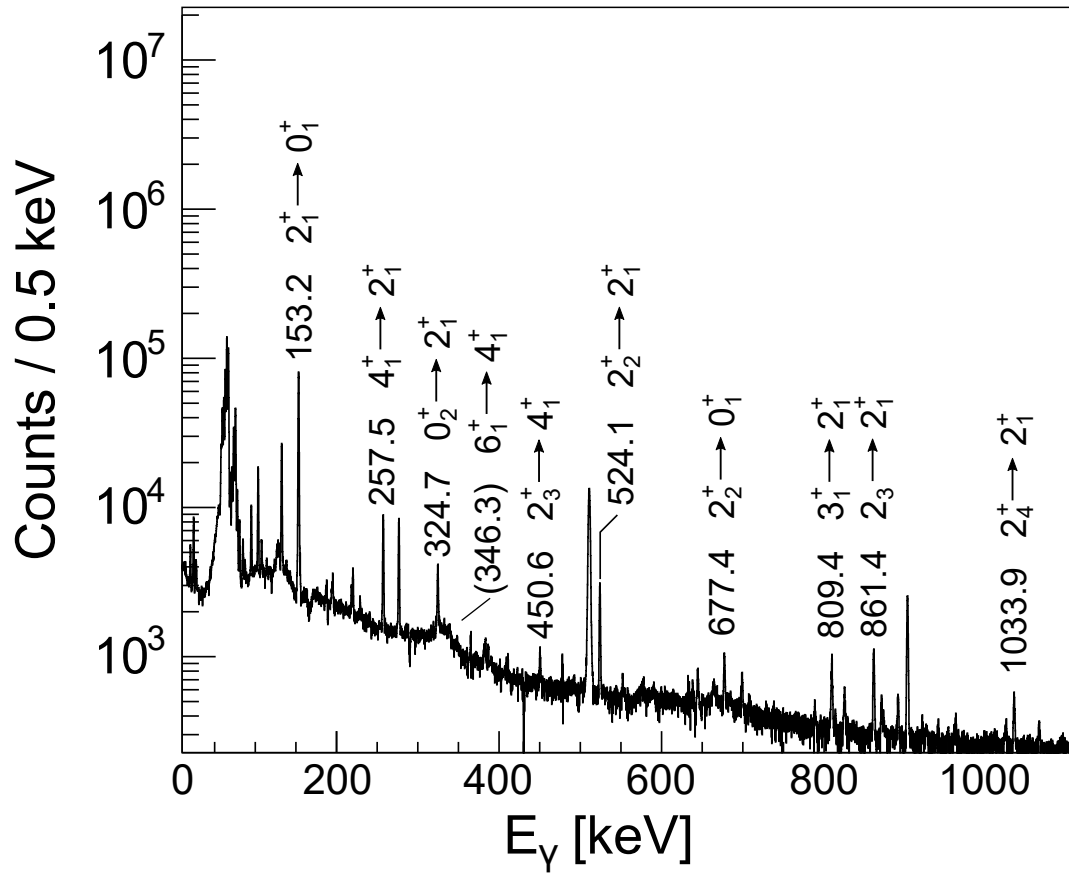
FIGURE 5.9: Background subtracted γ-ray energy spectrum detected by the LEGe at A = 180. Transitions associated with the decay of ^{180}Pt are indicated (energies in keV). The expected position of the unobserved 346.3 keV $6_1^+ \rightarrow 4_1^+$ decay is in indicated in brackets.

For the follow-up discussion in Sec. 5.6.1 in respect of the spin and configuration of ^{180}Au, it is instructive to compare the observed β-decay patterns of ^{180,182}Au$\rightarrow^{180,182}$Pt, both presented in the Davidson *et al.* work. Similarly to the ^{180}Pt case, a predominant feeding to the 2_1^+ state in ^{182}Pt was also observed in the β decay of the $I = 2^+$ ground state of ^{182}Au (see below), see Table 2 in [124], with the ratios $I(154.9, 2_1^+)/I(264.7, 4_1^+)/I(355.6, 6_1^+) \approx 1000(10):443(10):19(5)$. One notices a difference by a factor of ~ 2 in the feeding of the of 4_1^+ state in respect of 2_1^+ between ^{180,182}Au, and a much lower feeding of 6_1^+ in ^{180}Au. The lower relative feeding to 4_1^+ and 6_1^+ in ^{180}Au might indicate that the ground-state spin of ^{180}Au is lower than that of ^{182}Au. This is because the structure and positions of the low-energy states in the daughter nuclides ^{180,182}Pt are very similar [124], therefore the difference in β-decay patterns should be related predominantly to the difference in the structure of the parent ^{180,182}Au isotopes. The strong direct β-decay feeding in decay of both ^{180,182}Au and the difference in respective patterns was further demonstrated in Fig. 7 of [124].

5.5 Hyperfine Structure Measurements for ^{180,182}Au.

With an aim to gain further insight into the possible spin assignment for ^{180}Au, the hfs data collected in our experiment for both ^{180,182}Au were also investigated. Similar to the discussion of the respective β-decay patterns, the comparison of hfs structure for ^{180}Au with known data for the $I=2^+$ ground state of ^{182}Au, deduced in [30, 31], could be instructive to validate the analysis procedures applied further for ^{180}Au.

5.5.1 Spin assignments for ^{180,182}Au

The left-hand-side of Fig. 5.10 shows the RILIS ionization scheme, used to study ^{180,182}Au, the same scheme as exploited in our study of ^{177,179}Au in [36]. The expected
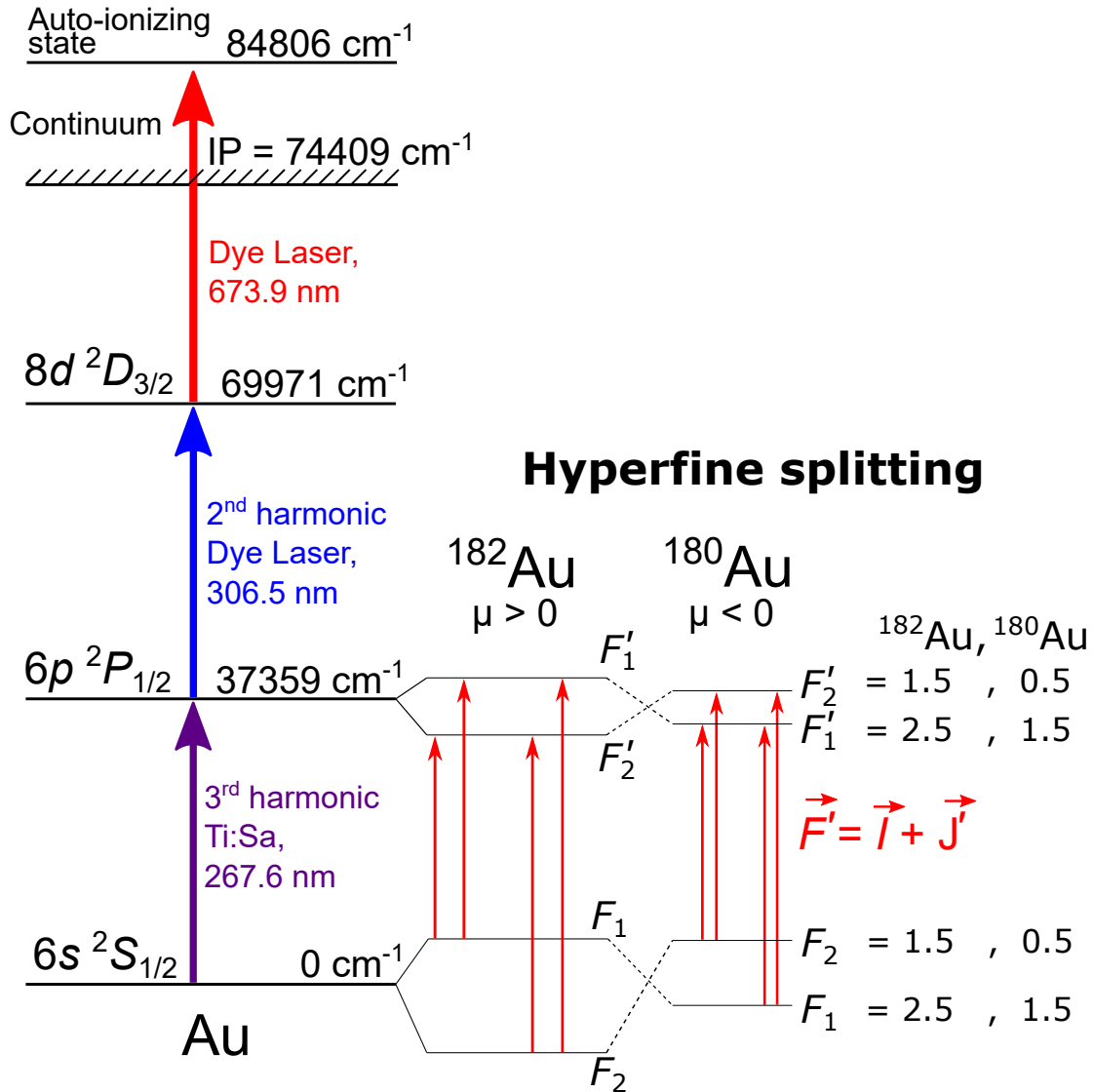
FIGURE 5.10: The three-step resonant photo-ionisation scheme used by RILIS to produce
^{180,182}Au ions. The hfs for the 267.6 nm (natural linewidth $\approx$ 26MHz) first step is shown (not to
scale). I is the nuclear spin, while J, F and J', F' are the electron spin and the total angular atomic
momenta for the ground state $6s^2S_{1/2}$ and excited state $6p^2P_{1/2}$, respectively. The four allowed
atomic transitions between $F_{1,2}$ and $F'_{1,2}$ sub-levels are indicated by the coloured arrows. Note the
inverted positions of the sub-levels $F_{1,2}$ and $F'_{1,2}$ in ^{180,182}Au, which reflects the opposite signs of
their respective magnetic moments.
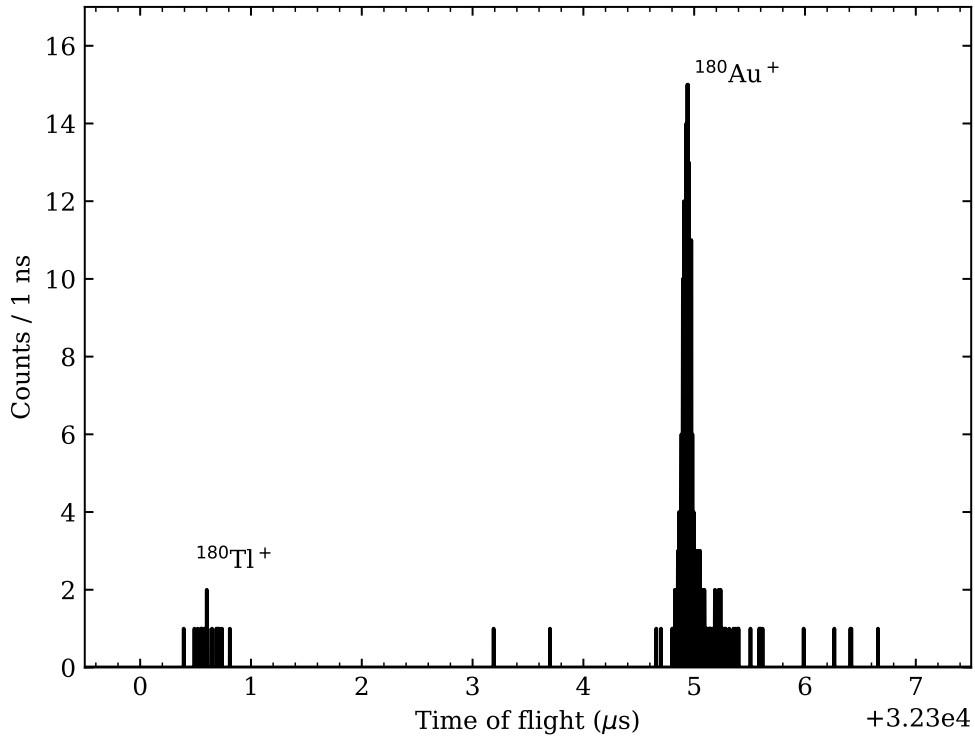
FIGURE 5.11: Time-of-flight spectrum of A = 180 after 1000 cycles in the MR-ToF MS, with the RILIS optimised for the maximum peak efficiency of ^{180}Au. A small amount of ^{180}Tl is visible at edge of the acceptance window. Data courtesy of [113].

hyperfine splitting is shown schematically for the 267.6-nm excitation laser step. Four transitions between the initial and final states of the hfs structure are possible in both cases, as indicated in the right-hand-side part of Fig. 5.10, but their ordering and relative positions depend on the sign and on the value of the magnetic hyperfine constant A (thus on the sign

of the magnetic moment), respectively. A positive magnetic moment, $\mu_I(^{182}Au)$, was derived by the study [30], which is confirmed by the present data, discussed below, while the first measurement of the magnetic moment, $\mu_I(^{180}Au)$, and its negative sign were deduced in this work. The Fig. 5.10 shows the respective differences in hfs between the two cases.

The hfs spectra for the 267.6-nm transition in $^{180,182}Au$ were scanned by counting photo-ions ions as a function of the first step Ti:Sapphire (Ti:Sa) laser which was used to produce the 267.6-nm beam via a third harmonic generation. The fundamental laser frequency was measured using a wavelength meter (WS7 model by HighFinesse/Angstrom). Further details of the scanning procedure can be found in [35, 36, 71]. For each step in the scanned laser frequency (1 per super-cycle), the laser power and integral proton pulses were recorded to normalise the data across the scanning range. Typically the laser would see a 10-15% power reduction at higher frequencies.

Two hfs spectra for ^{182}Au were measured by ion counting with the MR-ToF method and five for ^{180}Au (two scans with the Windmill and three scans with MR-ToF MS); Figure 5.11 shows an example of a typical MR-ToF MS Time-of-Flight spectrum and Fig. 5.12 shows examples of the respective hfs scans. The spectral resolution is a culmination of the large Doppler broadening in the hot cavity of RILIS [126], laser line width and potential saturation broadening effects. As a result, the pairs of closely-lying hfs transitions, which are shown schematically by the narrow black vertical lines in Fig. 5.12, result in their partial (^{182}Au) or full overlap (^{180}Au).

We start the discussion with an example of a MR-ToF hfs spectrum for ^{182}Au shown in Fig. 5.12(a). Despite the Doppler broadening, a clear separation of four expected atomic transitions can be seen. The FWHM of a single transition was equal to 4.8 GHz. For ^{182}Au, with $\mu > 0$, the two left peaks at lower wave numbers in Fig. 5.12(a) correspond to transitions $F_1 \rightarrow F_1', F_2'$, as shown in Fig. 5.10. The two right peaks at higher wave numbers in Fig. 5.12(a) correspond to the two transitions from the F_2 sub-level (cf. Fig. 5.10).

We can consider the experimental ratio, (r_{exp}), of the sum of the intensities for two left

and two right peaks in Fig. 5.12(a), respectively. Theoretically, this ratio is determined by a simple expression as a function of nuclear spin I:

$$r_{th}(I) = \frac{\Gamma(F_1 \to F'_2) + \Gamma(F_1 \to F'_1)}{\Gamma(F_2 \to F'_2) + \Gamma(F_2 \to F'_1)} = \frac{2F_1 + 1}{2F_2 + 1} = \frac{I+1}{I} \tag{5.3}$$

where Γ is the intensity of the respective transition. This ratio is independent of laser saturation and other factors which may distort the spectrum shape. For spin assignments of $I = 1,2,3$, the theoretical ratio values are $r_{th} = 2$, 1.5 and 1.33 respectively. The weighted mean of the experimental r values for the two hfs spectra available for ^{182}Au, $r_{exp} = 1.61(15)$, further supports the $I(^{182}$Au$) = 2$ spin assignment, earlier proposed in [31] as 'most likely', and the validity of the r-ratio method.

Furthermore, the hfs spectra for ^{182}Au were fitted using Voigt profiles with the Lorentzian component coming from the natural linewdith and the Gaussian component from thermal Doppler broadening, see [71] for details of the fitting procedure. However, it should be noted the difference between the fitting with a guassian or voigt profile was negligible. By using the spin assignment of $I(^{182}$Au$) = 2$, the measured hfs pattern is accurately reproduced by the fit, see the red line in Fig. 5.12, which gives further confirmation from our data on the validity of this spin assignment.

We now turn to the hfs of ^{180}Au shown in Figs. 5.12(b,c). As seen in these spectra, the hfs of the upper level in ^{180}Au was not resolved due to the Doppler broadening of the atomic transitions [35], thus only two bumps have been observed. In this case, the peak at lower wavenumbers has a lower intensity than that of the higher wavenumbers, which unambiguously testifies to the negative sign of $\mu_I(^{180}$Au$)$, discussed further in the next section. As a result, the ordering of the F_1,F_2 and F'_1,F'_2 sub-levels is reversed, see Fig. 5.10. Experimentally, this means that the left bump of Figs. 5.12(b,c) is now the sum of the two unresolved peaks which correspond to transitions $F_2 \to F'_1, F'_2$, whilst the right peak is the sum of two transitions $F_1 \to F'_1, F'_2$, the opposite of the hfs of ^{182}Au shown
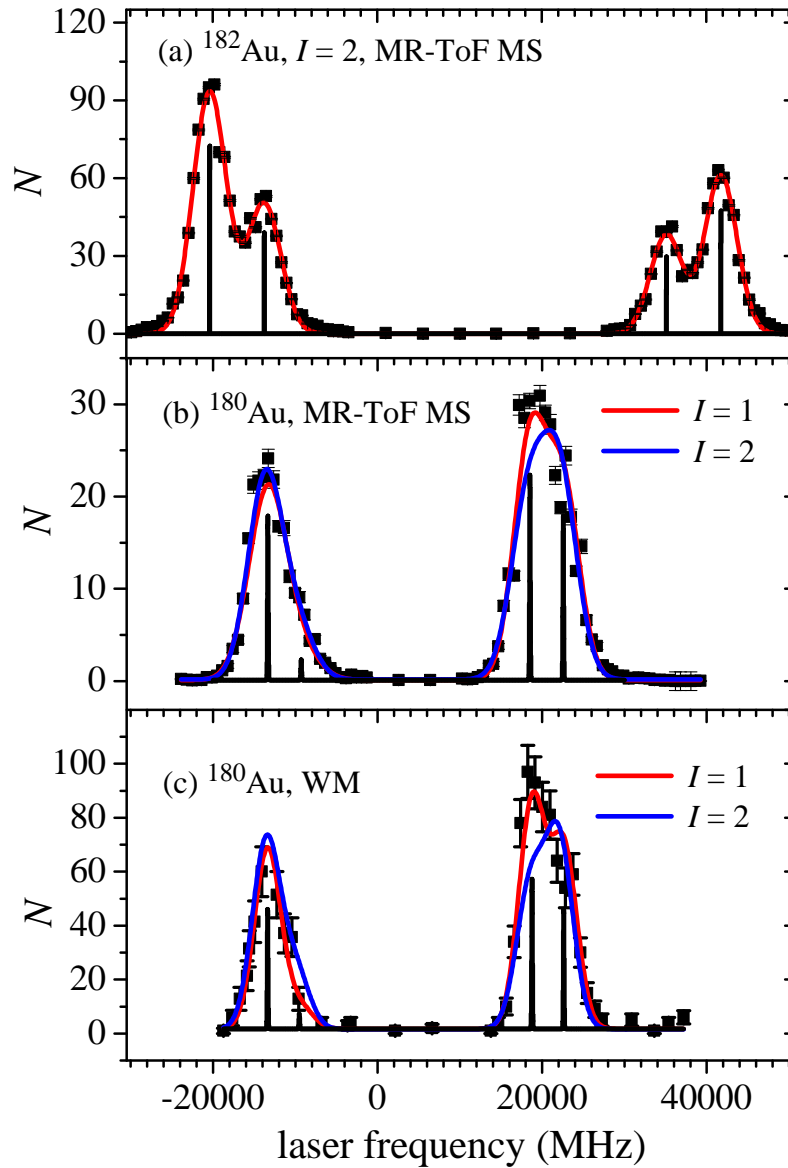
FIGURE 5.12: Typical examples of the hfs spectra (filled black squares) for the 267.6-nm transition in $^{182,180}Au$: a) an hfs scan of ^{182}Au as measured by the MR-ToF MS; b) and c) are the hfs scans of ^{180}Au using the MR-ToF MS and Windmill decay station, respectively. The expected theoretical positions and intensities of the four hfs components for the assumptions of $I=2$ for ^{182}Au and $I=1$ for ^{180}Au are shown by the narrow black peaks. The results of the Voigt-profile fits of the experimental hfs spectra are shown by solid red lines (spin assignments $I(^{182}Au)=2$ and $I(^{180}Au)=1$), and by solid blue line for $I(^{180})Au=3$. Fitting with $I=2$ is not shown on (b/c) as it is visually indistinguishable from that of $I=3$.

in 5.12(a). Therefore, for ^{180}Au, the experimental r-ratio is equal to the ratio of integrals under the right and left bumps in Figs. 5.12(b,c), respectively.

The weighted mean of experimental r values for the five hfs spectra available for ^{180}Au, $r_{exp}= 2.06(20)$, indicates the strong preference for an $I = 1$ assignment. Additionally, fittings with $I = 2, 3$ spin assumptions for ^{180}Au, which could be possible from the β-decay data if there was a direct β-decay feeding to 4^+ states, do not reproduce the details of the shape of the observed spectra, (see Fig. 5.12(b,c) only $I = 3$ is shown), which further favours the $I = (1)$ value.

To summarize this sub-section, the hfs analysis for ^{180,182}Au clearly suggests a difference in their spin values, with confirmed $I = 2$ for ^{182}Au and suggested $I = (1)$ for ^{180}Au. These inferences could naturally explain the difference in the feeding of several 2^+ states in comparison with 4^+ states in the respective β-decay patterns of ^{180,182}Au$\rightarrow$ ^{180,182}Pt, see Sec. 5.4. Indeed, the ratio $\frac{I(2_1^+)}{I(4_1^+)}(^{180}$Au, $I{=}(1)) = 4.3$ is larger than the respective ratio of 2.26 for ^{182}Au ($I = 2$) [124].

5.5.2 Experimental magnetic moments of the $I = 2$ state in ^{182}Au and $I = (1)$ state in ^{180}Au

The positions of the hyperfine components as a function of the scanning laser frequency in Fig. 5.12 are determined by the expression:

$$\nu_{F,F'} = \nu_0 + A(6p)\frac{K'}{2} - A(6s)\frac{K}{2},\qquad(5.4)$$

where ν_0 is the centroid frequency of the hfs, the prime symbols denote the upper level of the atomic transition (see definitions in Fig. 5.10), K is determined as per Eqn. 3.3 and $A(nl)$ is the magnetic hyperfine coupling constant for the atomic level with the quantum

numbers n and l. The hfs spectra for ^{182}Au were fitted using Voigt profiles [71], with an $I = 2$ assumption, resulting in a value of $A(6s,^{182}\text{Au}) = 22190(90)$ MHz with a ratio $\frac{A_{6p}}{A_{6s}}(^{182}\text{Au}) = 0.1196(24)$.

To determine the magnetic moment, recall Eqn. 3.10, where one can determine the magnetic moment of the desired isotope from its spin I and A factor using a reference isotope with magnetic moment $\mu_{I,ref}$, I_{ref}, A_{ref} and relative hyperfine anomaly (RHFA) Δ. For ^{180,182}Au, ^{197}Au is used as the reference isotope. Usually the RHFA is small effect, however in some gold isotopes it is known to very large, e.g. $^{197}\Delta^{198} = 0.0853(8)$ [127]. Therefore careful treatment of the RHFA must be considered for gold isotopes far from stability.

Previously, the prescription by Ekström *et al.* [22], modified in [25] was used to account for the large RHFA in gold when calculating their magntic moments:

$$\mu_I = \frac{A(6s)I}{29005} \tag{5.5}$$

However, Ref. [62] has shown this prescription is based on poorly justified assumptions and should be reconsidered. As shown in Ref. [62] the value of the RHFA for each isotope can be deduced directly from the ratio of the magnetic hfs constants for different atomic states of a nucleus, 6p and 6s in the case of gold. The ratio A_{6p}^A/A_{6s}^A, depends the atomic mass mumber (superscript A), because different atomic states differ in sensitivity to the distribution of the nuclear magnetisation (see [62] for full details). By applying this procedure a RHFA $^{197}\Delta^{182} = 0.19(3)$ was deduced.

Using $A_{6s}(^{197}\text{Au}) = 3049.660092(7)$ MHz [128], $A_{6p}(^{197}\text{Au}) = 312.7(1.2)$ MHz [129] and $\mu_I(^{197}\text{Au}) = 0.14574(4)$ μ_N [128] with the diamagnetic correction from [130] and the RHFA deduced above, a value of $\mu_I(^{182}\text{Au}) = 1.68(5)$ μ_N was derived.

By using the same procedure as above for ^{180}Au, the hfs spectra were fitted with an $I = 1$ assumption, resulting in the value of $A(6s,^{180}\text{Au}) = -21370(180)$ MHz, with

$A_{6p}(^{180}\text{Au})/A_{6s}(^{180}\text{Au}) = 0.1219(70)$ and $^{197}\Delta^{180} = 0.22(10)$. From the above a value of $\mu_I(^{180}\text{Au}) = -0.83(7)\ \mu_N$ was deduced. The latter value will be used in Sec. 5.6.1 to evaluate the configuration of ^{180}Au. The experimental magnetic moments for ^{180,182}Au deduced with the Ekström *et al.* prescription [Eq. (5.5)] and with the approach by Barzakh *et al.* [Eq. (3.10)] are shown in Table 5.2. One can notice a difference by $\approx 10\%$ between the two methods.

5.6   Discussion

5.6.1   Derivation of magnetic moments and configurations for the ground states of ^{180,182}Au based on the deformed additivity relation

Proton and neutron Nilsson orbitals relevant for ^{180,182}Au

As shown by the analysis of the isotope shift in ^{180,182}Au, these nuclei are deformed with a mean-square quadrupole deformation of $\langle\beta^2\rangle^{1/2} \approx 0.28$ [131]. Therefore, to assign configurations for the ground states of ^{180,182}Au we will consider the systematics of the lowest deformed single-particle states near $Z = 79$ and $N = 101,103$. As seen in Fig. 5.13, several proton and neutron levels are expected to lie close to the Fermi surface for ^{180,182}Au at $\langle\beta_2\rangle^{1/2} \approx 0.2 - 0.3$. It is worth noting that the ground states of the deformed gold isotopes $^{182\text{-}186}$Au ($N = 103 - 107$) are assumed to be based on the $\pi1/2^-[541]$ or $\pi3/2^-[532]$ Nilsson states [26, 27, 132, 31]. Note also, that the $\nu1/2^-[521]$ orbital is assigned as the ground state configuration in isotonic ^{181}Hg$_{101}$ and ^{179}Pt$_{101}$ [133, 134].

The Gallagher-Moszkowski rule may be used to constrain the orbitals near the Fermi surface which can couple to $I = 1$ for ^{180}Au and $I = 2$ for ^{182}Au. The possible configurations are shown in Tab. 5.2, where both negative and positive parity states are shown for the sake of completeness. The choice of the most likely configurations for ^{180,182}Au is determined
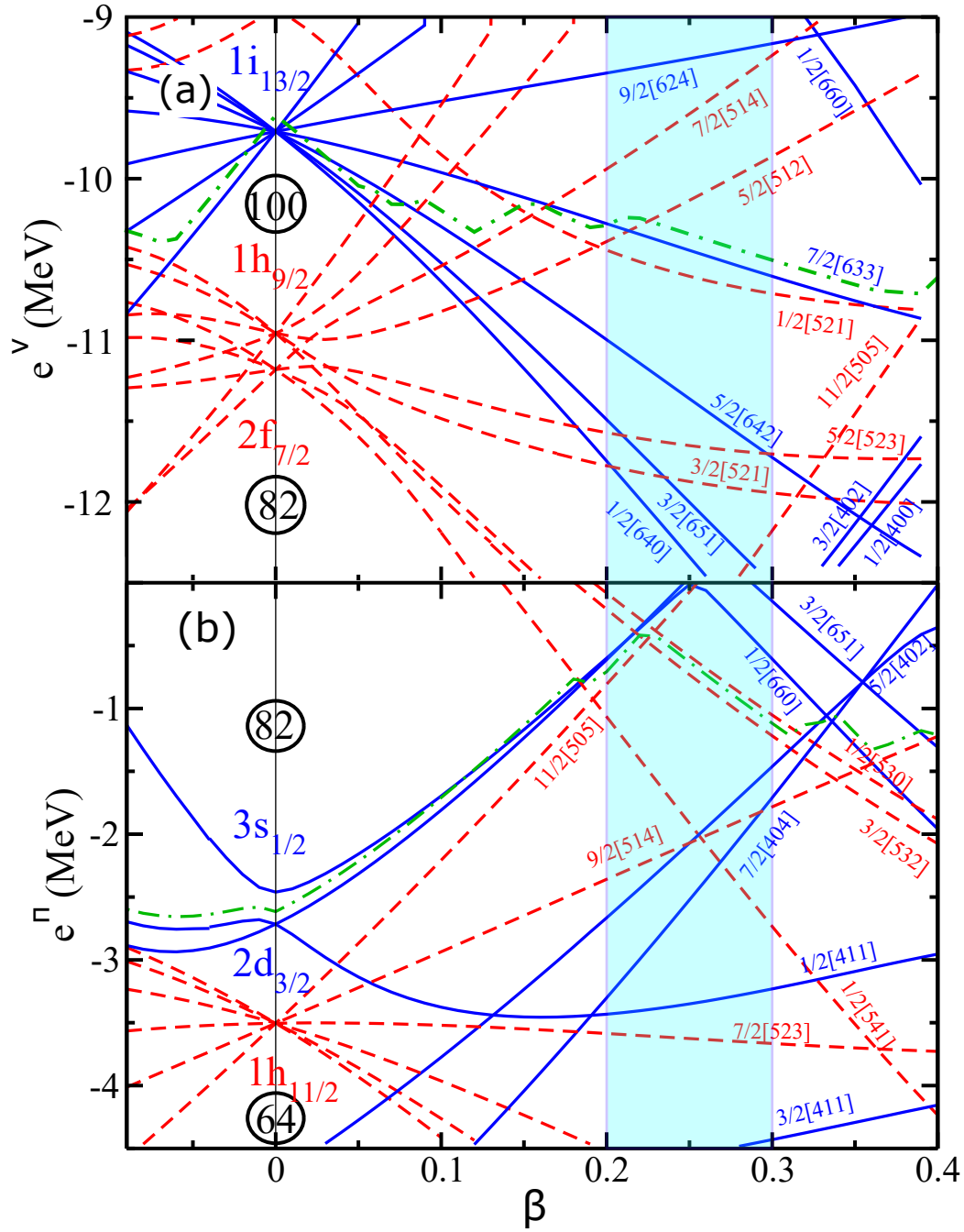
FIGURE 5.13: Nilsson diagram relevant to the ^{180}Au; (a) for neutrons ($82 < N < 126$), (b) for protons ($50 < Z < 82$). The shaded region indicates the region of deformation $0.2 < \beta_2 < 0.3$.

by comparing their experimental μ_I values, with the theoretical values for the odd-odd configurations from Tab. 5.2, calculated using the following additivity expression [135]:

$$\mu_{calc} = \frac{K}{K+1}[\pm g_{KP} \cdot K_p \pm g_{Kn} \cdot K_n + g_R], \tag{5.6}$$

$$K = |K_p \pm K_n|, \tag{5.7}$$

where $K_{p,n}$ is the projection of the angular momentum on the symmetry axis for proton and neutron states, g_K is the intrinsic g factor, g_R is the rotational gyromagnetic ratio ($g_R = Z/A \approx 0.4$ is usually adopted for odd-odd nuclei in this region [135]). Signs in Eqn. 5.6 are chosen in accordance with those in Eqn. 5.7.

The intrinsic g_K factors for the chosen orbitals were calculated by the standard Nilsson-model approach with the different parameters sets [136, 137, 138, 121], and extracted, when possible, from the measured magnetic moments [43] by the relation [135]:

$$g_K \cdot K = \frac{K+1}{K}\mu_{odd,exp} - g_R, \tag{5.8}$$

The uncertainties in the g_K values were estimated from the dispersion of the results obtained by the different approaches. The deduced μ_{calc} values are shown in the last column of Tab. 5.2.

Configuration of the I=2$^+$ ground state of ^{182}Au

The previously-reported $\mu_I(^{182}\text{Au})$, was derived from g-factor measurements by employing time-resolved and time-integral on-line nuclear orientation methods at the NICOLE-ISOLDE facility, considering different spin assumptions $I = 1\text{-}5$, see Tab. 3 of [30]. By comparing the g-factors from the two methods, the authors of [30] derived $\mu_I(^{182}\text{Au}) = 1.65(15)\,\mu_N$ by assuming $I = 3$, which gave the best agreement between the two different experimental

TABLE 5.2: Possible neutron-proton configurations which could couple to produce $I = 2$ in ^{182}Au and $I = 1$ in ^{180}Au. The magnetic dipole moment, μ_{calc}, of each configuration was calculated using the deformed additivity relations, Eq. (5.6). The configurations marked in bold correspond to the ground states of ^{180,182}Au as proposed by this work, see the main text. The last two columns show the magnetic moments deduced in this study within the Ekström *et al.* approach [22] and with the RHFA correction following the prescription from [62], respectively.

Isotope	$\pi \otimes \nu$ configuration	I^{π}	$\mu_{\text{calc}}(\mu_N)$	$\mu_{\text{exp}}(\mu_N)$, [22]	$\mu_{\text{exp}}(\mu_N)$, [62]
^{182}Au	**3/2⁻[532]h$_{9/2}$⊗1/2⁻[521]p$_{3/2}$**	2^+	1.22(35)	1.53(7)	1.68(5)
	$3/2^-[532]h_{9/2} \otimes 7/2^+[633]i_{13/2}$	2^-	-1.09(27)		
	$1/2^-[541]h_{9/2} \otimes 5/2^-[512]h_{9/2}$	2^+	-0.73(20)		
^{180}Au	**3/2⁻[532]h$_{9/2}$ ⊗ 5/2⁻[512]h$_{9/2}$**	1^+	-0.87(21)	-0.74(4)	-0.83(7)
	$7/2^+[404]g_{7/2} \otimes 5/2^-[512]h_{9/2}$	1^-	2.02(13)		
	$1/2^-[541]h_{9/2} \otimes 1/2^-[521]p_{3/2}$	1^+	0.58(20)		
	$5/2^+[402]d_{5/2} \otimes 7/2^-[514]f_{7/2}$	1^-	-1.51(20)		

techniques, although the spin values of $I = 2,4$ could not be excluded, as was stated by the authors themselves. A subsequent β^+/EC decay study of ^{182}Hg $\rightarrow$ ^{182}Au at ISOLDE [31] proposed the ground state spin $I(^{182}\text{Au}) = (2^+)$ based on γ-γ and e$^-$-γ coincidence measurements, with the $\pi h_{9/2} \otimes \nu 1/2^-[521]$ as the most probable configuration from evaluating the lowest energy configurations and systematics from the neighbouring ^{184,186}Au isotopes [31]. The $I = (2^+)$ value is used in the present NNDC evaluations [121], which reported a value of $\mu_I(^{182}\text{Au}) = 1.30(10) \mu_N$ calculated from the average $g = 0.65(5)$ value of the two spin $I = 2$ g-factor derivations from Tab. 3 [30]. A $\approx 3 \sigma$ discrepancy between the evaluated value and the result from this work ($\mu_I(^{182}\text{Au}) = 1.65(5) \mu_N$) may be explained by the fact that in Ref. [30] the BW effect was neglected.

Out of three possible configurations, shown in Tab. 5.2, only the $\mu_{calc} = 1.22(35) \mu_N$ is reasonably close to the experimentally-deduced value, which further supports the choice

of $I = 2^+$ and the $3/2^-[532]h_{9/2} \otimes 1/2^-[521]p_{3/2}$ configuration for the ground state of ^{182}Au.

Configuration of the $I = (1^+)$ ground state in ^{180}Au

As seen from Tab. 5.2, a reasonable agreement between the experimental value, $\mu_I(^{180}\text{Au})$ = -0.83(7) μ_N and the calculated additivity values can only be obtained for the state with $I^\pi(^{180}\text{Au}^g) = 1^+$, with a $\pi 3/2^-[532] \otimes \nu 5/2^-[512]$ configuration. Thus, the proton state in ^{180}Au^g is expected to be the same as in ^{184,182}Au ($\pi 3/2^-[532]$), whereas the assigned neutron orbital ($\nu 5/2^-[512]$) is the same as the ground states of several $N = 99$ and 103 nuclei (^{177}Pt$_{99}$, ^{175}Os$_{99}$, ^{173}W$_{99}$, ^{171}Er$_{103}$, ^{173}Yb$_{103}$, ^{175}Hf$_{103}$, see [138] and the references therein).

5.6.2 α-decay hindrance factors for ^{180}Au

Alpha-decay hindrance factors (HF$_\alpha$) are a sensitive probe for providing information on the spin and/or configuration of the states linked by the decay, provided the properties of either parent or daughter states are well established. In the case of ^{180}Au, one could try to use the HF$_\alpha$ values in the decay chain of ^{184}Tl $\rightarrow$ ^{180}Au $\rightarrow$ ^{176}Ir. However, the application of this method is not possible in this case due to the following reasons. First of all, as shown below, the tentative 5675/5686-keV α decay is strongly hindered, by a factor of HF$_\alpha > 1700$. This provides evidence for a large spin and configuration difference between the ground states of ^{180}Au and ^{176}Ir, possibly supporting the validity of tentative $I(^{176}\text{Ir}) = (5^+)$ proposed in earlier studies [123]. However, no further conclusions can be drawn especially considering the multitude of low-energy states proposed by other studies [139, 140, 141]. Similarly, there are also no direct α decays linking the known α-decaying states with $I = 10^-$, 7^+ and 2^- of ^{184}Tl to the proposed $I = (1^+)$ ground-state of ^{180}Au (see Figs. 12, 13 of Ref. [32]).

Turning to the discussion of the relative strengths of the f.s. α decays from ^{180}Au^g, could help establish the similarities or differences of respective daughter states in ^{176}Ir. Figure 5.5 shows the δ_α^2 values of each f. s. decay of ^{180}Au, calculated using the Rasmussen approach assuming $\Delta L = 0$ decays. HF$_\alpha$ values, can be calculated by comparing the δ_α^2 values for α decays from ^{180}Au, to unhindered α decays in neighbouring odd-A nuclei ^{181}Au and ^{179}Au.

Based on the data from [121], values of $\delta_\alpha^2(^{181}$Au, 5479 keV $(3/2^-) \rightarrow 3/2^-) = 75(11)$ keV and $\delta_\alpha^2(^{179}$Au, 5848 keV $1/2^+ \rightarrow 1/2^+) = 57(4)$ keV were deduced, for the respective unhindered $J \rightarrow J$ α decays. The average of these values, $\delta_\alpha^2 = 66(6)$ keV, was used as a reference for ^{180}Au in the following analysis. The 5485-keV α decay in ^{180}Au is only weakly hindered with HF$_\alpha = 2.7(7)$. Based on this low HF$_\alpha$ value, we suggest that the state at $\Delta + 195.7$ keV in ^{176}Ir fed by the 5485-keV α decay, is probably of the same spin and/or configuration as the parent ^{180}Au ground state. Further tentative spin assignments could be made for some of the states linked to the $\Delta + 195.7$ keV state, via γ decays with deduced M1 multipolarities (e.g. the 36.5-, 41.5- and 118-keV transitions) which can establish the parities of the respective states. However, it is best to refrain from this analysis due to the large number of possible spin values when coupling several angular momenta which are not well defined.

As another explanation for relatively low and comparable hindrance factors for several f.s. α decays in ^{180}Au, one could consider a possibility of decays to excited states of the same rotational band in the (deformed) daughter. There are such cases known in the literature, including in the region close to ^{180}Au. For example, in the ^{181}Hg$\rightarrow^{177}$Pt α decay, the $1/2^- \rightarrow 1/2^-$ decay is unhindered [HF$_\alpha = 0.86(12)$], while the two decays to the $(3/2^-)$ and $5/2^-$ excited states have moderate hindrance factors of 6.5(20) and 7(3), respectively. The $(3/2^-)$ and $5/2^-$ states are most probably the members of a rotational band built on the 147-keV $1/2^-$ state fed by unhindered α decay of ^{181}Hg. Thus, medium values of HF$_\alpha$ = 5–20 in this region may be due to the decay to rotational states in the daughter nuclide

based on the same configuration as in the parent nucleus. However, at present, it is difficult to assess the validity of this scenario for ^{180}Au, because not much is known about the detailed structure of the daughter nucleus ^{176}Ir. A dedicated study of both its ground state and of the expected complex pattern of low-lying excited states, as suggested by calculations in Ref. [140], would be needed to shed more light on this scenario.

This additional information could possibly help understand the puzzling fact of the strong hindrance of the tentative 5675-keV α decay relative to the 5485-keV, 5598-keV and 5539-keV decays. Indeed, an M1 character of the three γ transitions at 36.5-keV, 41.5-keV and 118-keV linking the four states fed by these decays suggests that the spin of the state at Δ fed by the 5675 keV decay should be not too distinctive from the states fed by other α decays. Therefore, the α-decay hindrance for the 5675-keV decay should be much lower than observed. The presence of the direct, albeit rather weak, 195.7-keV parity-conserving transition following the unhindered 5485-keV decay also highlights this discrepancy.

A similar argument cannot however yet be applied for the case of the 205.2 keV transition, as the parity of the lowest state in ^{176}Ir is not known. For example, a negative parity of this state (thus, an E1 or M2 multipolarity for the 205.2 keV decay) would indeed cause a strong hindrance for the 5686-keV decay. This is both due to the very strong sensitivity of the α-decay process to the parity change and a need for a respective substantial change of the underlying configuration of the state.

6 β-NMR studies with Na isotopes

6.1   Hyperfine structure of ^{26}Na observed by β-asymmetry

Two isotopes, ^{26,27}Na were used for the β-NMR studies presented throughout this chapter. Both are readily produced at ISOLDE, have a high degree of β-decay asymmetry, are easily polarised as atoms and possess suitable half-lives to perform β-NMR measurements. ^{28}Na was also considered as a probe isotope, however it was dismissed due to the decreased production yield and long-lived daughter isotope (^{28}Mg, $T_{1/2}$ = 20.9 hours) which would contribute to the β-decay background. Intially, the nuclei were implanted into a cubic lattice crystal host, in this case a NaF crystal. The crystal host had a uniform local electric field at the substitutional site, and therefore did not induce a quadrupole component to the NMR resonances. Furthermore, previous β-decay asymmetry studies with ^{26,27}Na [104] have shown a polarisation relaxation time up to 37 s, preserving the polarisation of the implanted nuclei for longer than the lifetime of the nuclear decay.

A hfs scan of ^{26}Na of the D2 line, $^2S_{1/2} \to {}^2P_{3/2}$ is shown in Fig. 6.1. Here, the β-decay asymmetry from the beam implanted into the NaF crystal is shown as a function of Doppler tuning voltage. The $^2S_{1/2}$ state splitting is well resolved as evidenced by the two main structures located at -1.9 V and $\approx$ 0 V. The splitting of the excited $^2P_{3/2}$ is only partially resolved, thus optical excitation is not restricted to the idealised closed system of $|^2S_{1/2}; F = I + 1/2\rangle \leftrightarrow |^2P_{3/2}; F' = I + 3/2\rangle$. As such, it is possible for photon emission from the upper state to occur via neighbouring hyperfine levels of the $^2P_{3/2}$ state

to the $F = I - 1/2$ component of the ground-state, ending the optical pumping process. This acts to reduce the overall achievable polarisation.
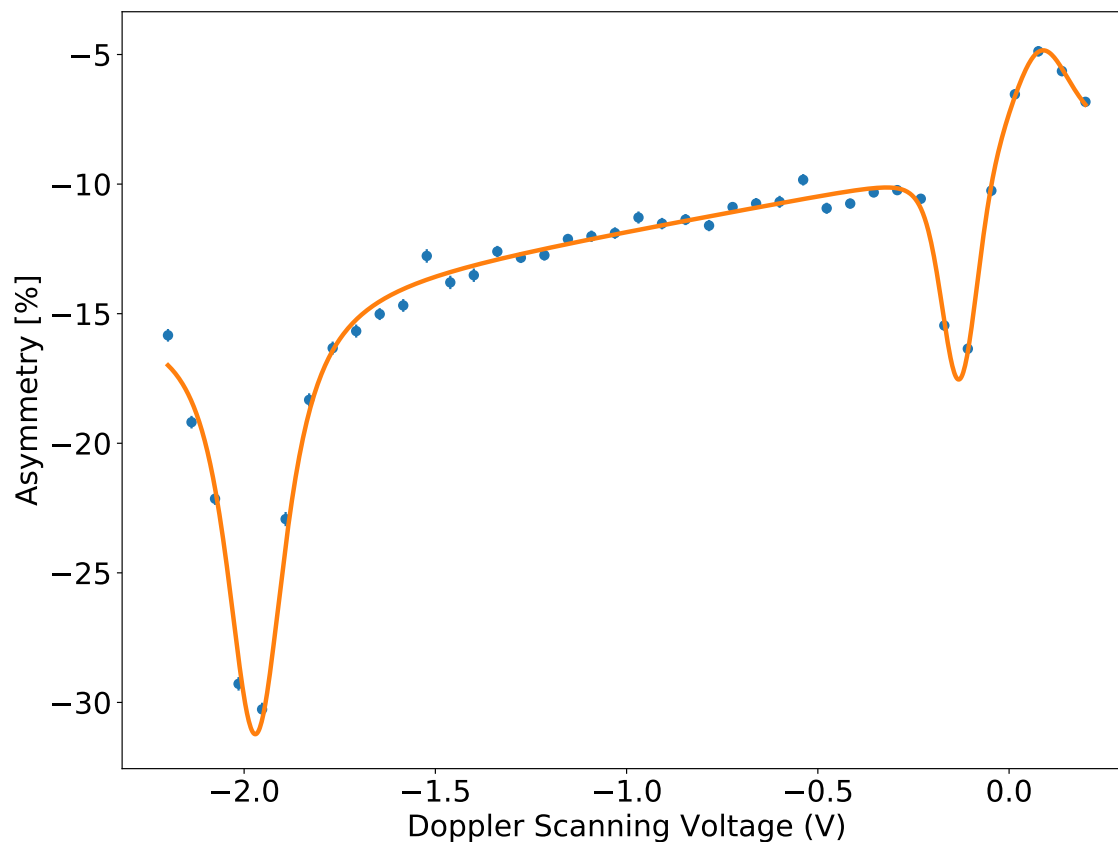
FIGURE 6.1: Hfs scan of ^{26}Na, measured using β-decay asymmetry. The resonance positions are shown as function of the Doppler tuning voltage applied to the voltage scanner.

The signs and amplitudes can be understood from simulations of the optical pumping process, and the hyperfine structure scan shown in Fig. 6.1 replicates those found in [104, 142]. The sloping background in the hfs scan is due to a small misalignment of elements

within the voltage scanner, leading to beam steering and focusing as the ion beam energy is scanned across the voltage range. This creates a shift in the beam position on the crystal causing a change in the overall asymmetry. The installation of VITO's new charge exchange cell and voltage scanner in January 2018 rectified these problems for the later experiments, more details are found within [18]. For the β-NMR studies, the voltage is locked to the greatest component of the β-decay asymmetry in the hyperfine structure, for ^{26}Na this was located at -1.95 V.

6.1.1   Beta-NMR with isotopes of sodium in crystal hosts
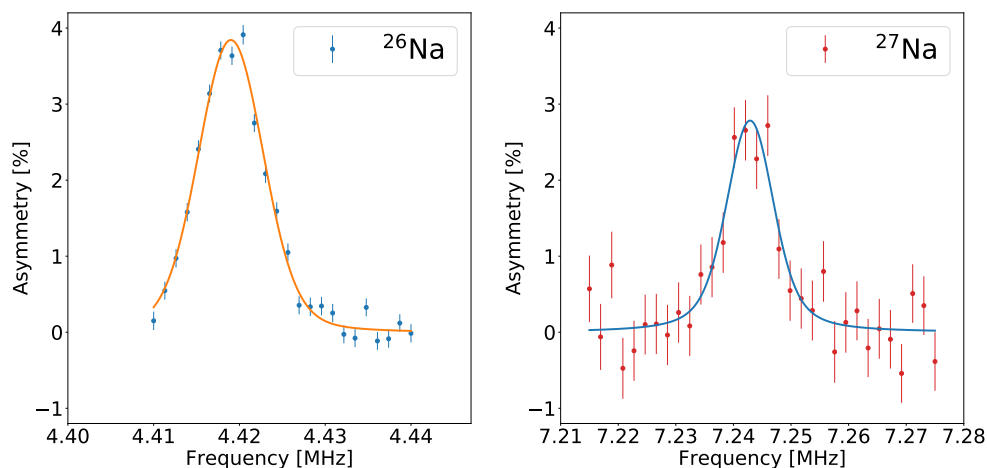
FIGURE 6.2: β-NMR spectra of ^{26}Na and ^{27}Na implanted into a NaF crystal, taken during the first β-NMR experiments in September 2017.

β-NMR scans of ^{26,27}Na implanted into a NaF crystal are shown in Fig. 6.2. Here, the frequency emitted from the RF coil is varied in discrete steps in an attempt to destroy the induced laser polarisation. These data, and all the following NMR spectra in this thesis

were fitted using the SATLAS analysis package in python [143]. In the following sections, ^{27}Na was used in the online tests of the differential pumping system and ^{26}Na was used for the systematic study of Room Temperature Ionic Liquids (RTIL). The saturation of the resonances in the NaF crystal as function of RF amplitude, is shown in Fig. 6.3.
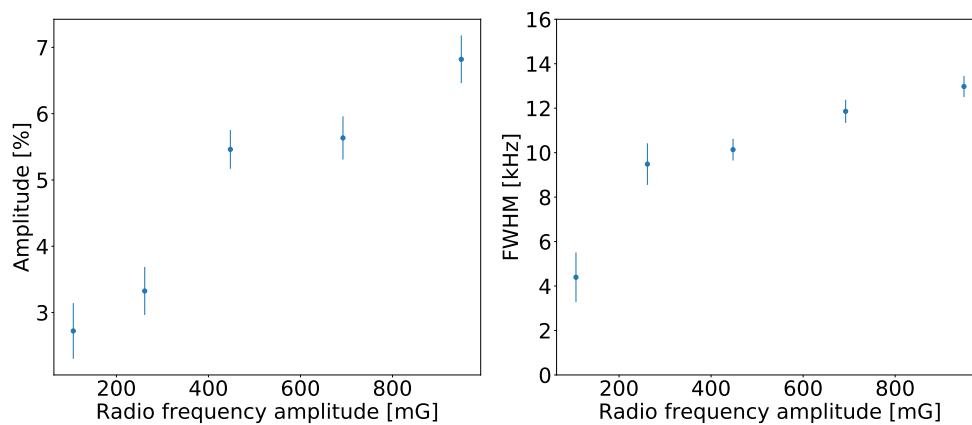
FIGURE 6.3: Left: Amplitude saturation curve of ^{26}Na implanted in a NaF crystal, as a function of applied RF amplitude. Saturation appears to occur at $\approx$ 450 mG. Right: FWHM of the resonance as a function of applied RF amplitude.

6.2 Towards Beta-NMR in bad vacuum environments

After successfully demonstrating β-NMR of sodium isotopes implanted in inorganic crystals, the project transitioned to the application of the β-NMR technique to the inter-disciplinary fields of inorganic chemistry and biology. Here, the increased detection efficiency coupled with the palette of probe nuclei available would provide an excellent addition to already established NMR studies. One area of research that would greatly benefit from the increased sensitivity of β-NMR, is the investigation of the role of alkali metal ions such as K^+ and Na^+ in the formation and stability of G-quadruplex DNA structures [144, 145, 146]. It is preferable to study these DNA structures in a solution, such as in water, where cation movement is less restricted, and better represents the natural biological environment where these structures are found. Previous efforts to study DNA G-quadruplexes using conventional NMR spectroscopy [144, 145, 146] have revealed the likely chemical shift of one binding site within the central structure observed between -15 and -20 parts-per-million (ppm), away from the ^{23}Na signal from the bulk medium.

To directly compare the chemical shift between the bound sites in a DNA G-quadruplex and the bulk medium, it would be ideal to use NaCl(aq), (NaCl dissolved in water) as our host medium for the DNA G-quadruplex, as has been done in previous studies [144, 146]. However, aqueous solutions require pressures of several mbar to remain in their liquid state (water has vapour pressure of ≈ 8.6 mbar at 278 K [147]). Throughout ISOLDE, the vacuum is on the order of 10^{-7} mbar to avoid ion beam transmission losses from collisions with rest gas molecules in the beamlines. The sample will need to be kept in a region of bad vacuum to prevent evaporation. To perform this task a differential pumping system was designed and tested at VITO, with the objective of transiting eight orders of magnitude in pressure, whilst providing a high degree of ion beam transmission to the sample and preserving the beam's polarisation.

6.2.1 Offline testing and vacuum simulation of a differential pumping system

To maximise the transmission efficiency of the 50-kV ISOLDE beam and preserve beam polarisation, the most prudent approach would be to use a series of small apertures with no physical barrier between the regions of different pressure. Figure 6.4 shows a schematic diagram of such a system. To keep a constant pressure in the detection chamber, the gas flow into and out of the chamber must be equal. The gas flow out the chamber, qpV_{tot} can be defined as:

$$qpV_{tot} = C_1(P_1 - P_2) \tag{6.1}$$

where $P_{1,2}$ are the pressures in the chamber and differential pumping system, respectively [148]. C_1 is the conductance of the aperture A1 separating the two regions, which is dependent on the dimensions of the aperture and the flow regime of the gas. To optimise the transport of the ion beam and preserve its properties, P_2 needs to be kept as small as possible. Therefore, we can assume that $P_1 >> P_2$ and Eqn. 6.1 simplifies to $qpV_{tot} \approx C(P_1)$.

The flow through the differential pumping region is also constant, therefore $qPV_{tot} = qPV_1 + qPV_2$. If the diameter of $A3$ is chosen such that it is $<< A2$, then it follows that $qPV_2 << qPV_1$ and $qPV_{tot} \approx qPV_1$.

The pressure inside the differential pumping vacuum vessel can be described by:

$$P_1 = \frac{qPV_{tot}}{S_1} \tag{6.2}$$
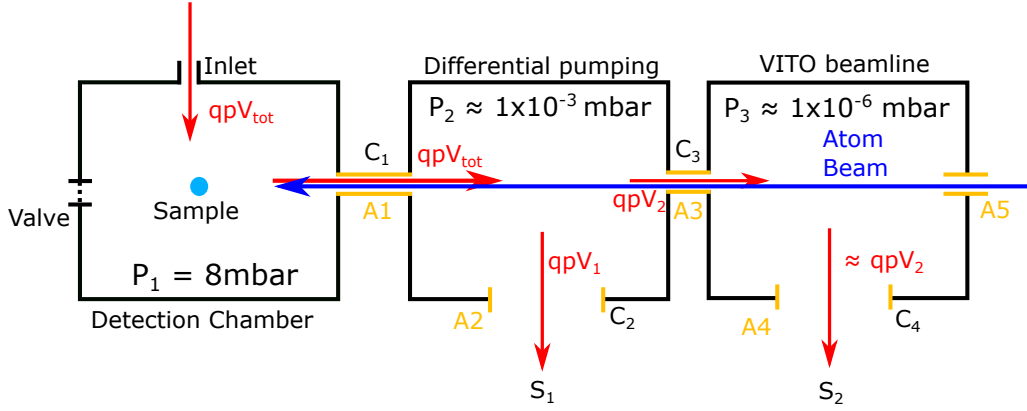
FIGURE 6.4: A simplified schematic diagram of VITO's differential pumping system. The gas flow through the system is indicated by the red arrows. The polarised atom beam from ISOLDE is represented by the blue arrow. The orange lines indicate the different apertures through which the gas will flow. The expected pressure in each region, 'P', is indicated within each chamber of the diagram. For an explanation of the symbols see the main text.

where S_1 is the speed of the pump in that region [148]. Combining Eqns. 6.2 and 6.1 we obtain:

$$S_1 = C_1 \frac{P_1}{P_2} \tag{6.3}$$

Therefore if S_1, desired P_1 and the conductance C_1 of the aperture separating the differential pumping region and the chamber are known, it is possible to approximate P_2 [149].

The conductance through any part of the vacuum system is dependent on the flow regime of the gas, usually defined by the Knudsen number, *Kn*. This is a dimensionless quantity which depends on the mean free path of a molecule, λ, and the characteristic length of the conducting vacuum element [148]. For an aperture, the characteristic length is taken

as the diameter, *D*, therefore *Kn* is defined as:

$$Kn = \frac{\lambda}{D} \tag{6.4}$$

The mean free path is conditional on the pressure, temperature and mass of the gas. The boundaries between different flow regimes are continuous, but a rough approximation of is given by [148]:

$$Kn < 0.01 : \textit{Viscous flow}$$
$$0.01 < Kn < 0.5 : \textit{Transitional flow} \tag{6.5}$$
$$Kn > 0.5 : \textit{Molecular flow}$$

At sufficiently low pressures, the mean free path is comparable or greater than the characteristic length of the system. Therefore, collisions with the walls of the vacuum vessel are more frequent than with other gas molecules and this regime is known as molecular flow. Here, as is shown in Eqn. 6.6, the conductance is independent of pressure. For viscous flow, where *Kn* < 0.01, collisions with other gas molecules dominate instead and the gas exbibits a fluid-like flow behaviour. The transitional region between these two regimes is a culmination of both of these effects and is difficult to describe analytically.

To determine the conductance in each regime we will use the formulas laid out in [148]. The aperture is assumed to be a tube of length L greater than diameter D. The formulas for

conductance in each regime are shown below:

$$C = \frac{\pi D^4}{128\eta L}\overline{P} : \textit{Viscous flow}$$

$$C = \left(\frac{\pi RT}{18M}\right)^{1/2}\frac{D^3}{(L + \frac{4}{3}D)} : \textit{Molecular flow}$$

$$C = \frac{\pi D^4}{128\eta L}\overline{P} + \frac{D^3}{6L}\left(\frac{2\pi RT}{M}\right)^{1/2}\left(\frac{1+F}{1+1.24F}\right) : \textit{Transitional flow} \qquad (6.6)$$

$$F = \left(\frac{M}{RT}\right)^{1/2}\frac{D}{\eta}\overline{P}$$

For accuracy, L has to be $\approx > 10\ D$, otherwise the conductance through the tube is overestimated; as L approaches zero, the conductance goes to infinity. In reality as L approaches zero, the conductance becomes equivalent to the flow through an aperture of zero length, but the dynamics between these two extremes is not easily described analytically. Furthermore, few numerical tools exist that accurately describe the behaviour of transitional flow where $L \approx D$. For simplification, only flow through a long tube will be examined. Finally, the conductance of the connecting vacuum elements between the aperture and the pump needs to be included.

Using Eqns. 6.3 and 6.6 the expected pressure in the differential pumping chamber, P_2, was calculated using the formulas in 6.6, for apertures of different L and D. To optimise atom beam transmission, a minimum aperture diameter of ≈ 3 mm was chosen. Due to the necessity of overlapping the atom and laser beam over a distance of ≈ 4 m, it would prove technically challenging to focus the atom beam to a sufficiently small cross section to pass through an opening smaller than 3 mm. Helium was chosen as the flow gas instead of air, due to its small molecular size and closed atomic shell (leading to lower beam scattering and a reduced loss of polarisation from collisions) and higher flow throughput in vacuum pumps. Finally, S was fixed to 860 l/s, the pumping speed for helium of an STP-603 pump
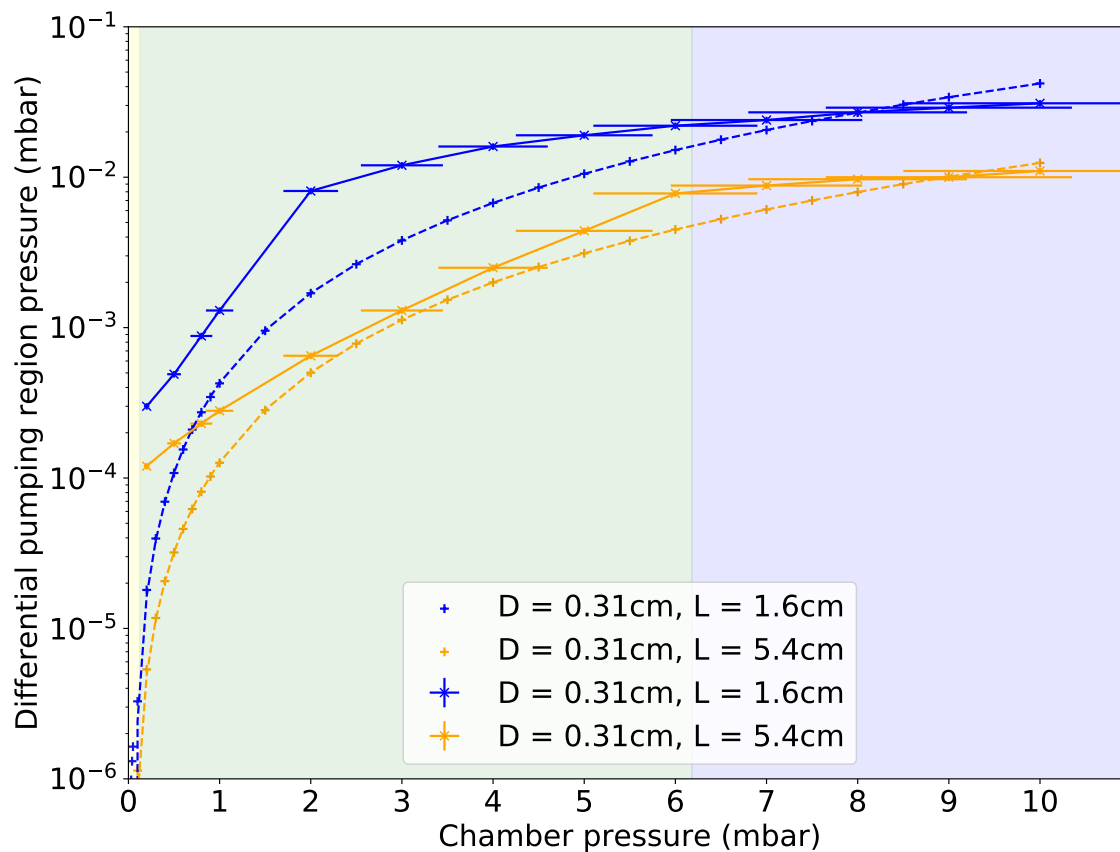
FIGURE 6.5: Simulations of the pressure in the differential pumping system through an aperture of various lengths (dotted lines). Experimental results from the offline results (solid lines), are shown for comparison.

which would be used in the practical setup, connected to nXDS 20i backing pump.

Using the above parameters the pressure P_2 was simulated for different length apertures as a function of the pressure in the detection chamber, P_1. The results are shown in Fig 6.5 as the dashed lines, with the flow regime of conductance through an aperture

of $D = 0.31$ cm indicated by the shaded regions. The simulations show that by using a long aperture it would be possible to achieve a differential pumping chamber pressure of 10^{-3} mbar, while maintaining a pressure of 8 mbar in the detection chamber, sufficient to keep a low temperature aqua solution from evaporating.

To benchmark the simulations an offline setup was constructed to test a variety of apertures. It comprised a detection chamber connected to a Con-Flange (CF) cross with inner tube diameters of 40- and 63 mm, with the STP-603 pump attached at one of the CF63
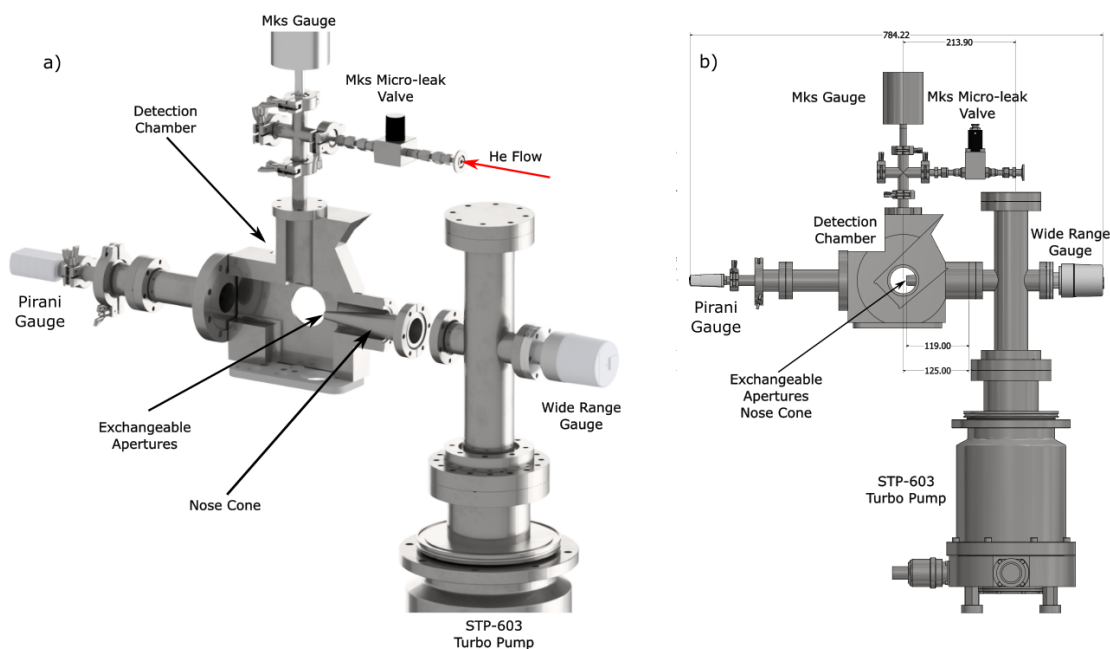
FIGURE 6.6: a) CAD Schematic of the offline differential pumping system. He gas flows into the detector chamber through the Mks micro-leak valve, and out through the nose cone towards the STP-603 Turbo Pump. The tip of the nose cone is threaded, to allow different size apertures to be exchanged. b) Dimensioned 2D schematic of the offline differential pumping system, in mm.
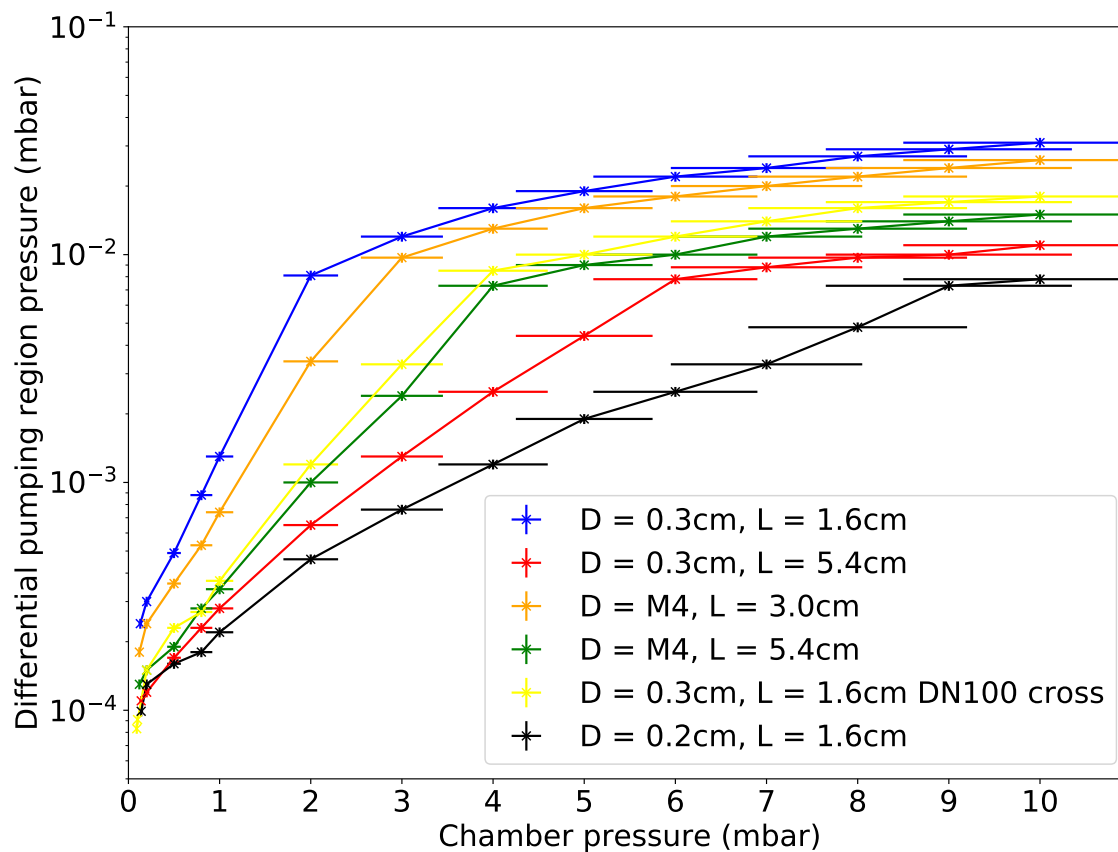
FIGURE 6.7: Offline tests of the differential pumping system involving different apertures of a variety of diameters and length.

openings. In between the cross and the chamber, a CF40 "nose cone" double-sided CF flange was placed with a threaded 6 mm diameter in the centre. The cone was introduced in order to reduce the distance the atom beam had to transit in the 8 mbar vacuum region of the chamber. The total length of the cone was the distance from central sample position to the edge of the detection chamber, see Fig. 6.6

Different size apertures or tubes could be exchanged via insertion into the threaded pinhole at the tip of the nose cone. All the vacuum parts were selected from aluminium components, to be compatible with VITO's magnetic field setup. A Pfeiffer PKR-251 full-range compact gauge was used to read out the pressure in the cross section and a Pfeiffer TPR-280 pirani gauge was attached to a vacuum port on the detection chamber. Helium was released into the chamber through an MKS instruments 148J micro-leak valve attached to another vacuum port, which was adjusted until the desired P_1 could be read from the pirani gauge.

Initially, tubes of 1.6 cm (the width of a CF40 flange) and 5.4 cm in length were chosen to compare to the simulations, see Fig. 6.5. Good agreement is seen in the higher pressure regions, while the simulations appear to underestimate the flow at lower pressures. However, the simulation neglects outgassing from the vacuum vessel walls, which dominates in low pressure regions. A variety of different diameter and length tubes were measured using the offline setup, as shown in Fig. 6.7. In general, smaller diameter and longer length tubes were more beneficial. Apertures with an M4 (4 mm) threaded inner diameter were also tested to examine the effects a non smooth surface would have on the gas flow in higher pressure regimes. The threaded aperture performed worse than expected, in part due to its diameter being $\approx$ 4 mm, larger than the 3 mm or smaller other diameters of the other tested apertures. The best results were obtained using the 2 mm diameter tube. Unfortunately, this was deemed impractical due to the limited transmission of the atom beam through such a small opening. Results also improved when using a larger diameter cross piece of DN100 compared to DN63, thus we endeavoured to use the largest conducting vacuum elements that would fit between the poles of the magnet.

A practical issue in the assembly of the setup was discovered during testing. The detection chamber consisted of CF40 flange, with threaded M6 holes which were used to secure exterior vacuum components to the flange. As the chamber was constructed out of aluminium, the threads were easily damaged or sheared from over tightening. Once a

thread had become damaged it impossible to repair. Thus, in further development of the differential pumping system, KF fittings were used instead.

6.2.2 Beam transmission and design of a differential pumping system

Using the information from the offline tests and simulations, an online differential pumping setup was developed in order to test the transmission efficiency of the atom beam to the sample. A new chamber was developed, equipped with KF flanges instead of the
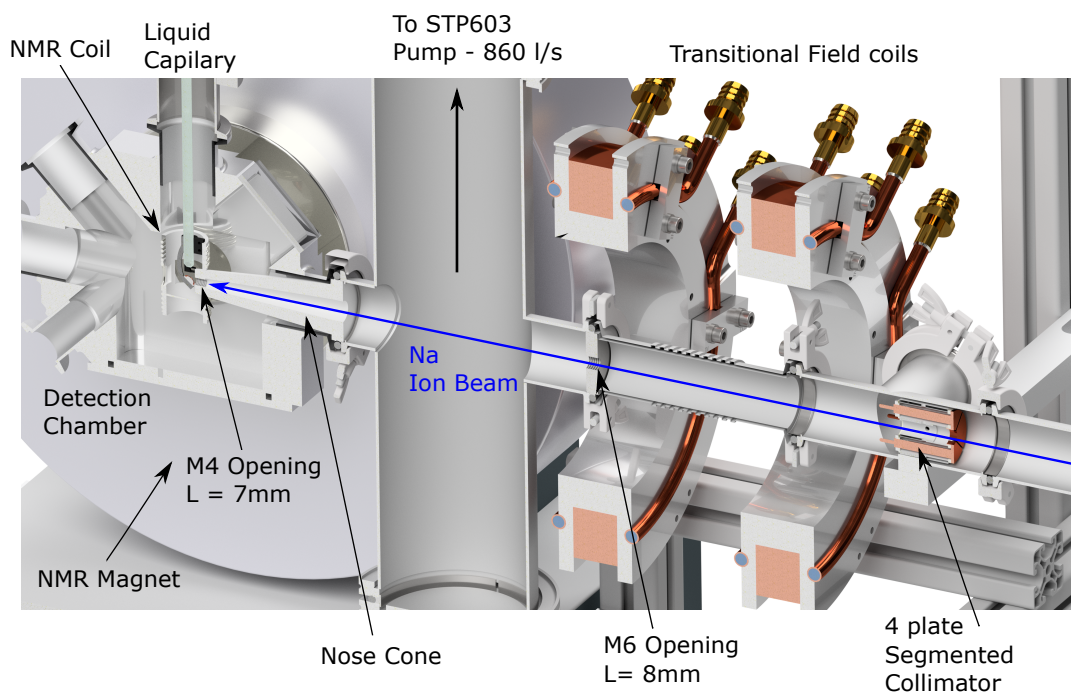
FIGURE 6.8: CAD drawing of VITO's differential pumping system, used in the online tests. A 3 mm diameter tube of length 16 mm was placed inside the tip of the nose cone, such that the end of tube was 0.5 mm from the sample.

previous CF. By moving to a KF design, the nose cone could be integrated into the KF-40 centring ring between the chamber and the differential pumping cross piece. The walls of the cone were thickened in order to reduce the transmission of β particles from atoms implanted on the inner surface of the cone. The length of the chamber was also reduced to lower the distance between the differential pumping system and the sample. A CAD design of the final design is shown in Fig. 6.8. At the end of the nose cone, an M4 thread permitted the use of tubes with different length and diameter. For the initial online tests a diameter of 3 mm and a length of 16 mm was used.

To maximise the conductance through the differential pumping system via the cross piece to the pump, a cross of DN-160 would be most prudent. However, the design is limited by the geometry of the electromagnet and surrounding structure. The largest size diameter cross that could be placed between the magnet cooling poles was DN-100. Finally, as the STP-603 is a magnetic levitation turbo pump, it had to be placed at sufficient distance from the magnet such that the stray field from the electromagnet did not interfere with the pump's operation, see Fig. 6.8. The transitional magnetic field was also redesigned from a solenoidal tube into a set of Helmholtz coils (HH coils) in order to accommodate the differential pumping cross piece and the pump. The diameter of the HH coils was limited to 180 mm to reduce the stray field along the beam axis to zero before the center of the electromagnet. If this was not the case, any misalignment of the HH coil magnetic field axis with the beam axis could potentially influence the NMR measurements.

To assist in the transport of the atom beam through the central hole of the nose cone, a segmented collimator was placed inside the beamline after the optical pumping interaction region. The collimator is composed of four conducting plates, attached to isolated pins read out by a four channel pico-ammeter. In the center of the collimator is a hole of 1 cm in diameter. If the beam is axially aligned it should pass through VITO's first iris before the CEC and through the collimator without inducing a readout signal. Due to the segmentation of the collimator, the atom beam can be steered and focused in the appropriate direction to
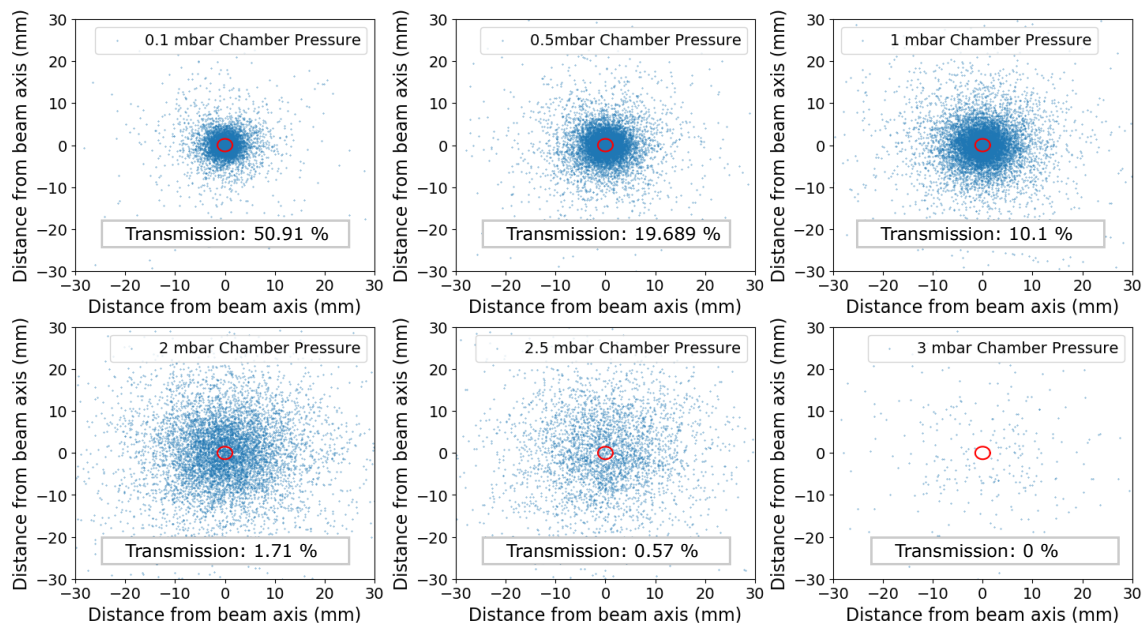
FIGURE 6.9: SRIM XY distribution plots for 10,000 atoms of ^{27}Na after transiting 263 mm of differential pumping vacuum and 0.5 mm of chamber vacuum. The chamber pressure is indicated in the top of each plot, with the differential pumping vacuum chosen according to the offline tests with an aperture of 3 mm diameter and 16 mm length. The red circle denotes a region of 3 mm in diameter. Particles within this region were considered transmitted to the sample.

correct beam misalignment.

With the geometry of the system established, the beam transmission of a 50 kV ^{27}Na atom beam was simulated using the SRIM package. The system was modelled as two regions, one of 0.5 mm width at pressure P_1 and the other of 263 mm at pressure P_2, with $P_{1,2}$ chosen in accordance with the offline tests for an aperture of diameter 3 mm and length 16 mm. Figure 6.9, shows the X,Y co-ordinates of the final position for the simulated particles (with Z being the beam axis). To estimate the transmission through the aperture,

any particle whose radial distance from the beam axis was below 1.5 mm was considered transmitted. The red circle on each plot indicates this region. While transmission at lower pressures was acceptable, the simulations showed that it is unlikely to transmit the atom beam to the sample when the chamber pressure is greater than 3 mbar. While this result would rule out the feasibility of having a water based solution as our host, there is potential for other solutions, e.g. glycerol or Polyethylene Glycol (PEG), which are used to mimic the surrounding environment of a cell. These solutions are biologically relevant and have slightly lower vapour pressures than water.

6.2.3   Online Beta-NMR from a crystal in bad vacuum

The differential pumping system as shown in Fig. 6.8, was tested online by examining β-NMR resonances from a 50-kV ^{27}Na atom beam implanted a NaF crystal. Unfortunately due to limited space, a vacuum guage wasn't installed in the differential pumping section, making direct comparison with the offline vacuum testing difficult. For an accurate comparison to the previous NMR data, the first test was performed in high vacuum conditions with a chamber pressure of 2×10^{-6} mbar. The pressure in the chamber was gradually increased, with β-NMR resonances taken at different He gas pressure intervals. The resulting spectra are shown in Fig. 6.10.

Increasing the pressure had no visible effect on the amplitude of the resonance until 0.5 mbar where a dramatic decrease was observed, see Fig. 6.11 and 6.10. The FWHM of the resonance remained constant across the entire pressure range. Spectra were also taken at 1 mbar but no resonance was visible. These results show the system in its current design would be unable to produce β-NMR resonances at the 8 mbar envisioned for water solutions. Possible solutions would include further reducing the size of the pinhole aperture, increasing the pump capacity, re-designing the system or changing the choice of host solution.
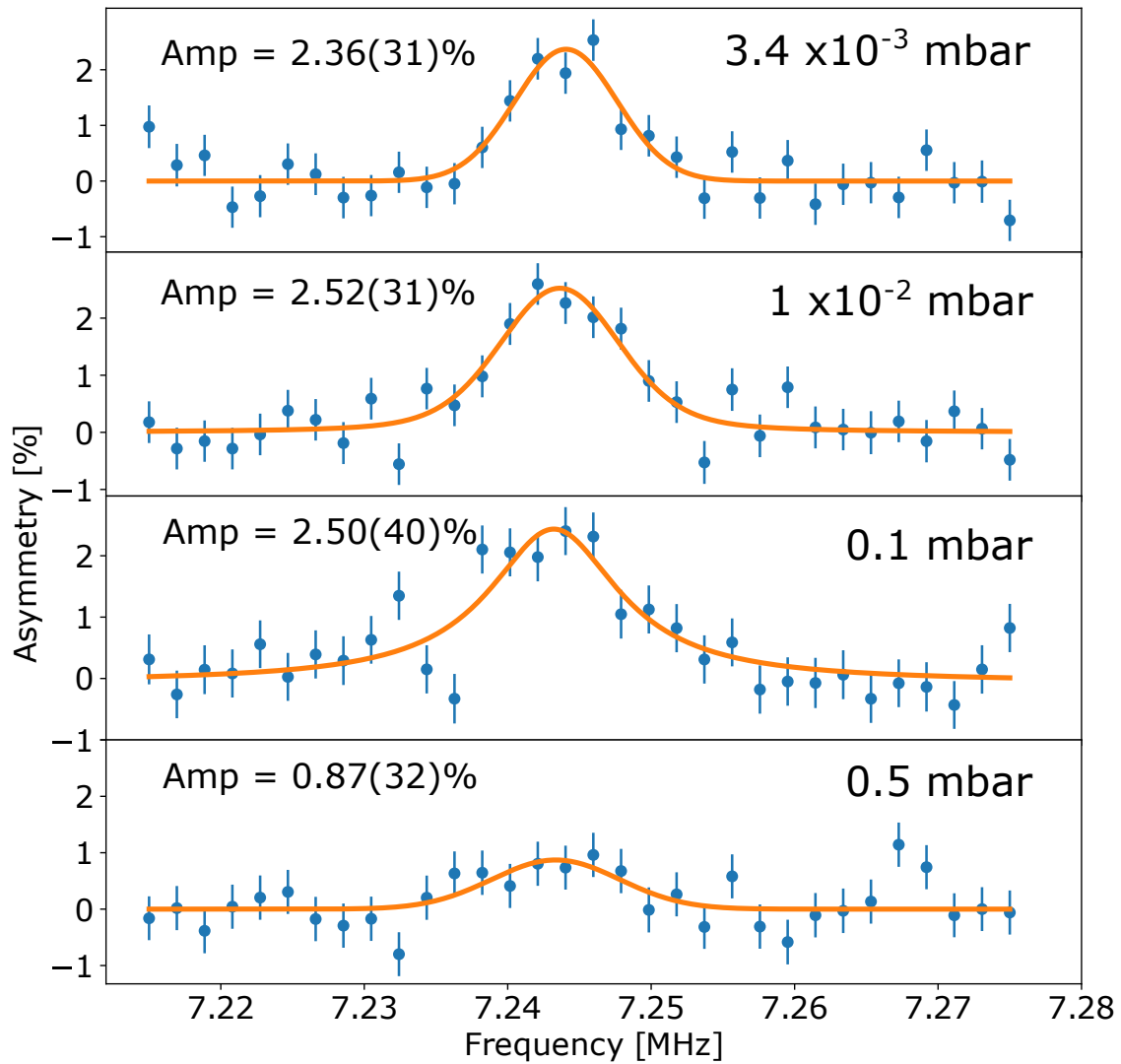
FIGURE 6.10: *β-NMR resonances from* ^{27}Na *implanted into a NaF crystal in different vacuum environments. The pressure in the chamber is indicated in the top right corner.*

In order to not compromise on signal quality from a reduced diameter aperture, alternative host solutions to water were investigated. In particular Room-Temperature-Ionic-Liquids (RTIL) would prove to be an excellent alternative that remain in a liquid state within high vacuum environments. Results from commissioning experiments involving these solutions are presented in the next section.
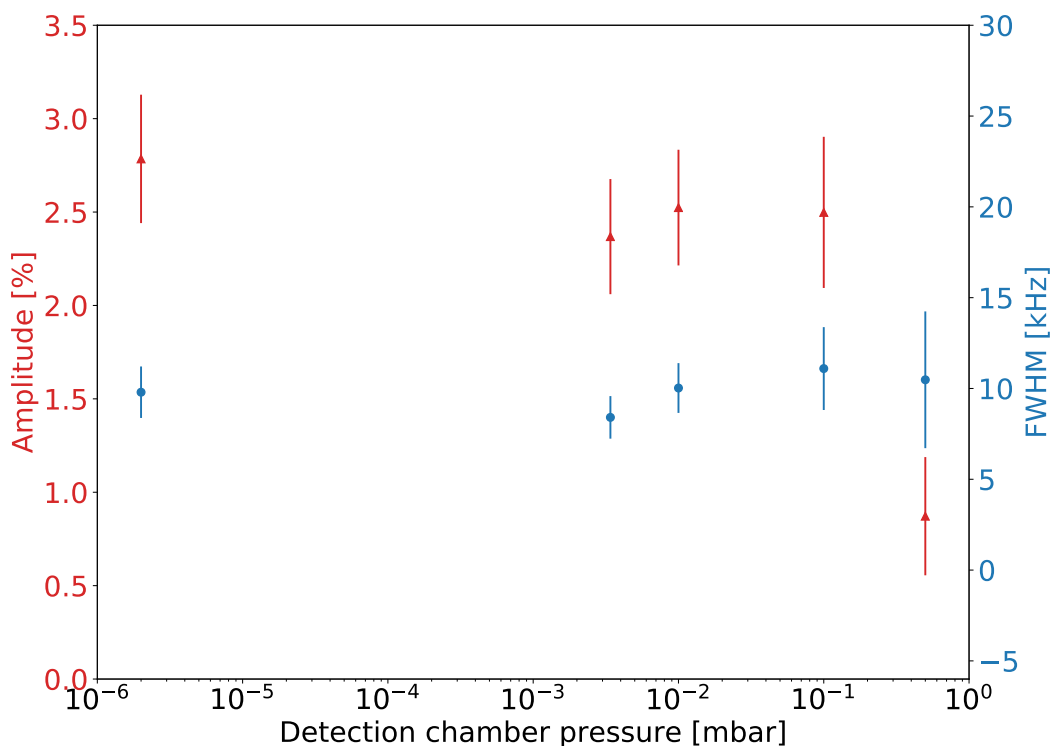
FIGURE 6.11: Comparison of amplitude and FWHM of β-NMR resonances from ^{27}Na implanted into a NaF crystal in different vacuum environments. The red triangles and axis refer to the amplitude of the resonances and the blue points and axis refer to the FWHM.

6.3 Beta-NMR from liquid hosts

RTIL are liquids that consist exclusively of ions, often referred to as molten salts. Compared to conventional organic solvents, these liquids have an extremely low vapour pressure originating from their dual ionic and organic nature [150, 151]. Furthermore, both organic and inorganic substances can be dissolved into them, indicating their potential as suitable hosts for high-precision NMR studies in vacuum environment.

Three different RTIL were investigated as potential hosts for future VITO experiments, 1-Butyl-3-methylimidazolium Acetate (BMIM-Ac), 1-Butyl-3-methylimidazolium formate (BMIM-HCOO) and 1-Ethyl-3-methylimidazolium dicyanamide (EMIM-DCA). These RTIL have vapour pressures around $1x10^{-6}$ mbar and were extensively used during the first tests of β-NMR at ISOLDE and as a part of complimentary NMR studies. They are available commercially and were also produced by collaborators at Poznan University of Technology.

In the first experiments in 2017, a liquid capillary system was used to place the liquid in the atom beam path. Before insertion into the chamber, each of the ionic liquids underwent outgassing for 24 hr in an offline vacuum chamber. Next the samples were removed and transported to the beamline where they were inserted into a liquid delivery system. In a two stage process, the liquid was evacuated to $2x10^{-2}$ mbar, before a valve was opened to a glass capillary that descended into the center of the chamber. The RTIL would travel down the capillary under gravity, and deposit onto a substrate holder in the center of the chamber. The capillary system was attached to 3-axis tilting bellows to lower and center the capillary/sample holder assembly into the beam path.

20 μL of each liquid was deposited onto the substrate for measuring one sample at a time. When changing the ionic liquid, the sample chamber was vented with the capillary and insertion tube replaced, with the procedure repeated for each RTIL. A comparison of the spectra from different liquids is shown in Fig. 6.12, with an RF amplitude of 950 mG.
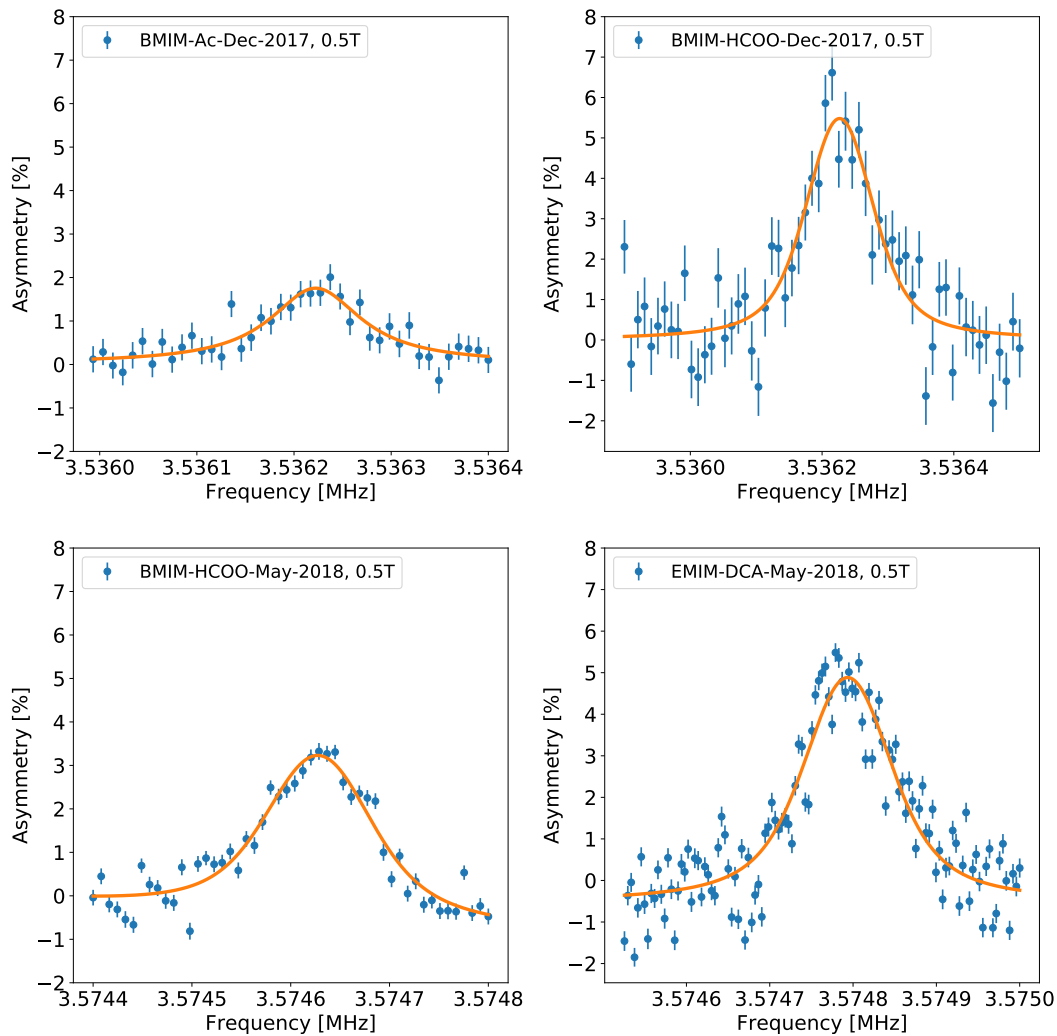
FIGURE 6.12: Comparison of *β*-NMR spectra from different RTIL hosts. All measurements were taken in a 0.5 T magnetic field with an RF amplitude of 950 mG. Developments to VITO modified some of the experimental conditions between the 2017 and 2018 experiments, see text for more details.

^{26}Na was used as the probe isotope in each case. The later experiments from 2018 used a sample ladder system instead, see Fig. 6.17. Here, each liquid was once again degassed in a offline chamber before being placed onto a sample holder substrate via a syringe. By using a sample ladder, different liquids could be studied in sequence without the need to vent the detector chamber.

The RTIL were tested across two experiments, one in December 2017 and the other in May 2018. Between these two experiments, VITO's charge exchange cell was replaced with a new unit. Table 6.1 shows the amplitude, centroid position (relative to a reference frequency, see each table for details) and FWHM of ^{26}Na β-NMR signals from each ionic liquid tested in the 2017 experiments. The data from the 2018 experiment is shown in Tab. 6.2. The centroid shifts and FWHM are shown in ppm, a quantity independent on the magnetic field. By using ppm, it is easier to directly compare NMR spectra taken in different magnetic fields.

Conversion between Hz and ppm is achieved by:

$$v_{ppm} = \frac{v - v_{ref}}{v_{ref}} \cdot 10^6 \tag{6.7}$$

where v_{ref} is the chosen reference frequency and v is the resonance frequency. In each table, v_{ref} is the resonant signal of the first measurement from each experiment. For these experiments in which the electromagnet operated at 0.5 T, 1 ppm is ≈ 0.5 Hz.

Remarkably, all of the RTIL had FWHM up to two orders of magnitude narrower compared to the previous measurements from the NaF crystal. A direct comparison of the spectra is shown in Fig. 6.13. This resonance narrowing arises due to molecular tumbling within the liquid sample, effectively averaging out the anisotropic contributions found in NMR spectra [152, 153, 154]. Also notable is the reduction in amplitude of the resonance in the RTIL as compared to the NaF crystal. The reason for this reduction becomes apparent upon examining the polarization relaxation in each material.
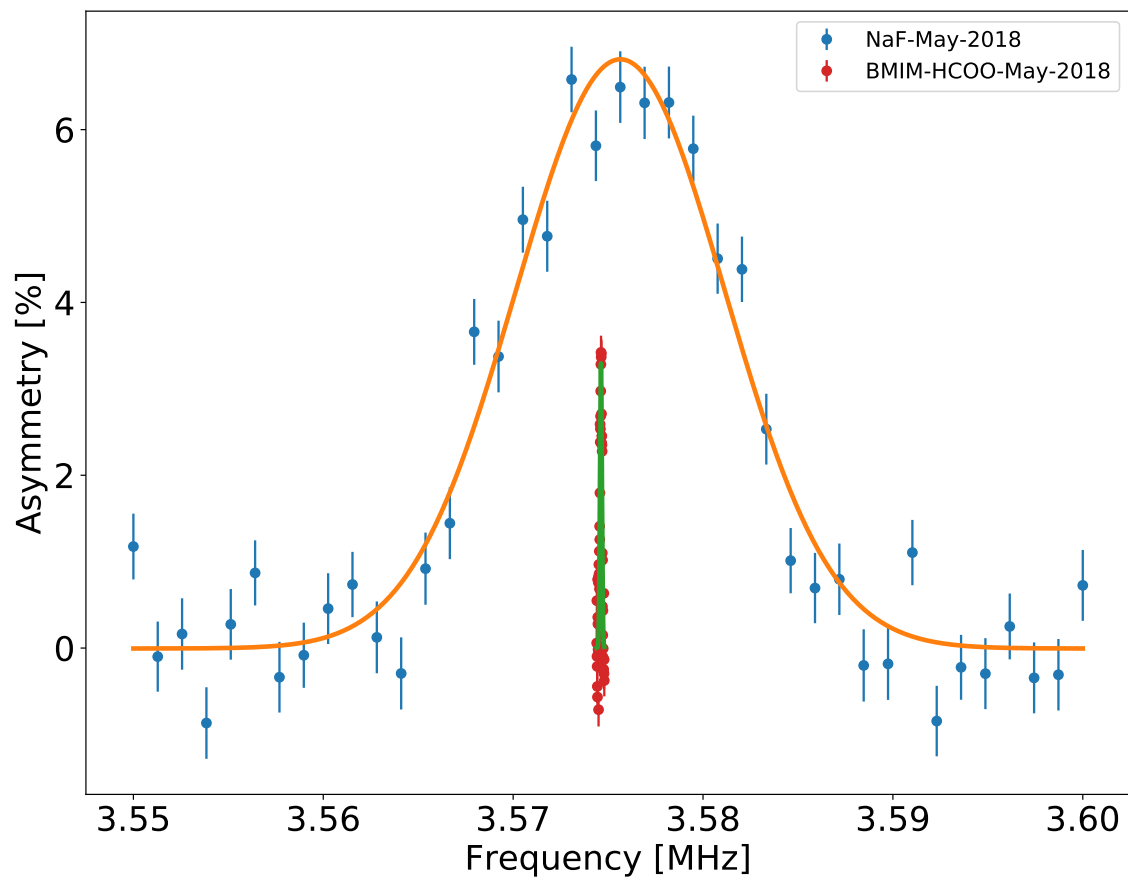
FIGURE 6.13: Comparison of *β*-NMR resonances from a NaF crytsal and BMIM-HCOO as measured during the 2018 beamtime, with the RF amplitude set to 950 mG. The width of the RTIL resonance is over 2 orders of magnitude smaller.

TABLE 6.1: *β-NMR measurements of RTIL from the December 2017 experiment using the 0.5 T NMR magnet. The centroid position and FWHM are shown in ppm. A reference frequency of 3.536222 MHz was used to calculate the centroid shifts and FWHM.*

RTIL	Run number	RF amplitude (mG)	Centroid B (ppm)	Amp (%)	FWHM (ppm)
BMIM-Ac	55	950	0(1)	1.8(2)	32(5)
BMIM-Ac	57	1500	0(1)	1.7(3)	49(5)
BMIM-Ac	63	450	0(1)	0.8(1)	19(4)
BMIM-Ac	64	260	-3(1)	1.5(3)	11(3)
BMIM-Ac	66	690	5(1)	2.0(2)	34(5)
BMIM-Ac	67	260	0(2)	0.9(2)	21(5)
BMIM-HCOO	71	690	2(1)	4.0(6)	40(5)
BMIM-HCOO	72	690	1(1)	5.5(4)	34(3)
BMIM-HCOO	73	260	0(1)	5.4(7)	11(1)
BMIM-HCOO	74	260	1(1)	5.3(2)	16(1)
BMIM-HCOO	79	260	10(1)	5.1(2)	17(1)
BMIM-HCOO	80	130	10(1)	5.0(8)	9(1)
BMIM-HCOO	81	130	13(1)	2.6(2)	12(1)
BMIM-HCOO	82	220	12(1)	2.8(6)	16(4)
BMIM-HCOO	83	80	14(1)	2.4(2)	6(1)
BMIM-HCOO	84	80	13(1)	2.7(1)	7(1)
BMIM-HCOO	86	40	12(1)	1.2(1)	8(1)
BMIM-HCOO	87	220	13(1)	3.4(4)	15(2)
BMIM-HCOO	89	450	16(1)	5.2(5)	17(2)

TABLE 6.2: *β-NMR measurements of RTIL from the May 2018 experiment using the 0.5 T NMR magnet. The centroid position and FWHM are shown in ppm. A reference frequency of 3.574625 MHz was used to calculate the centroid shifts and FWHM.*

RTIL	Run number	RF amplitude (mG)	Centroid B (ppm)	Amp (%)	FWHM (ppm)
BMIM-HCOO	27	950	0(1)	3.3(1)	34(1)
BMIM-HCOO	29	450	2(1)	4.1(1)	20(1)
BMIM-HCOO	30	260	3(1)	3.0(1)	18(1)
BMIM-HCOO	32	110	0(2)	1.9(1)	14(1)
BMIM-HCOO	34	30	2(1)	0.9(1)	9(1)
BMIM-HCOO	39	20	12(1)	0.7(1)	8(1)
EMIM-DCA	65	950	47(1)	4.8(1)	33(1)
EMIM-DCA	66	450	47(1)	6.7(1)	30(1)
EMIM-DCA	67	260	46(2)	3.3(1)	15(1)
BMIM-HCOO	68	110	50(1)	2.6(1)	17(1)
BMIM-HCOO	69	50	50(1)	1.4(1)	14(1)
BMIM-HCOO	71	50	47(1)	1.2(1)	16(1)
EMIM-DCA	83	30	38(2)	1.0(1)	15(2)
BMIM-HCOO	85	30	38(1)	1.0(1)	14(1)
EMIM-DCA	87	270	29(1)	2.6(1)	17(1)
EMIM-DCA	88	270	28(2)	3.7(2)	20(1)
EMIM-DCA	89	270	27(1)	3.2(1)	20(1)
EMIM-DCA	90	270	40(2)	5.8(1)	23(1)
EMIM-DCA	90	270	40(1)	5.8(1)	23(1)
EMIM-DCA	91	270	25(2)	3.7(1)	19(1)
EMIM-DCA	91	270	25(1)	3.7(1)	19(1)
EMIM-DCA	92	270	39(2)	6.2(1)	28(1)
EMIM-DCA	94	270	35(1)	5.8(1)	20(1)
EMIM-DCA	96	270	17(1)	7.7(1)	30(2)
EMIM-DCA	98	270	19(1)	5.5(1)	26(1)
EMIM-DCA	100	270	21(1)	5.7(1)	28(1)
EMIM-DCA	102	270	20(1)	5.8(1)	27(2)
EMIM-DCA	104	270	10(2)	7.0(1)	31(1)
EMIM-DCA	110	270	19(1)	4.6(1)	23(1)
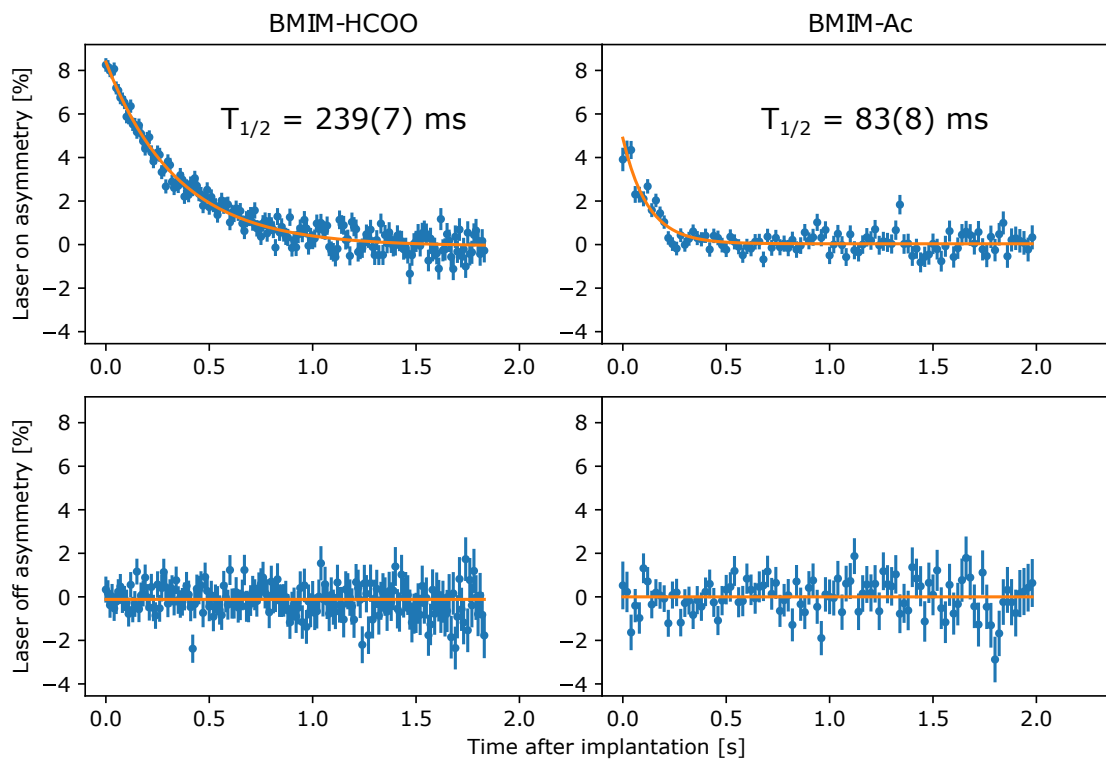
FIGURE 6.14: Relaxation of β-decay asymmetry of ^{26}Na in BMIM-HCOO (left) and BMIM-Ac (right). The measurements were performed in sequence with a laser shutter open (top) and closed (bottom) in order to observe the baseline asymmetry.

Figure 6.14 shows the relaxation of β-decay asymmetry in BMIM-HCOO and BMIM-Ac. Here, the beam is implanted into the RTIL after polarisation and β-decay asymmetry is observed as a function of time. For comparison, β-decay asymmetry with the laser shutter closed, and hence no polarisation, is also shown beneath each spectra. BMIM-HCOO shows a longer relaxation time, which is reflected in an increase in signal amplitude as the measurement window for a typical β-NMR resonance was several seconds. Previous

studies have shown that the relaxation time of ^{26}Na implanted into NaF is ≈ 37 s [104], much longer than each of the RTILs studied. In the May 2018 experiment the measurement window was reduced to one second to improve the signal amplitude.

The most promising ionic liquids (those with NMR resonances showing the largest amplitude and narrowest widths) were EMIM-DCA and BMIM-HCOO. To observe the RF saturation curve in each of these liquids, the resonance was recorded as a function of RF amplitude, which is shown in Fig. 6.15. The saturation starts being visible at around 300 mG amplitude.

As can be seen from Tabs. 6.16.2, the centroid position of different liquids appeared to drift by several dozens of ppm over the course the experiment. The drift was observed both when moving back and forth between the same samples, and if the sample was left in the same position for an extended duration. In order to measure a chemical shift at the expected 17-20 ppm level in DNA, the system would need a reproducible signal with this accuracy. Further investigation after the experiments revealed that the magnetic field of the NMR magnet, B_0, was unstable in time at the dozens of ppm level, previously un-observed in the NaF crystal due to lack of sensitivity associated with the broad resonance. As a result of the problems with the magnet which were not present in previous experiments, the magnetic field stability was tested extensively and improved as outlined in the next section.
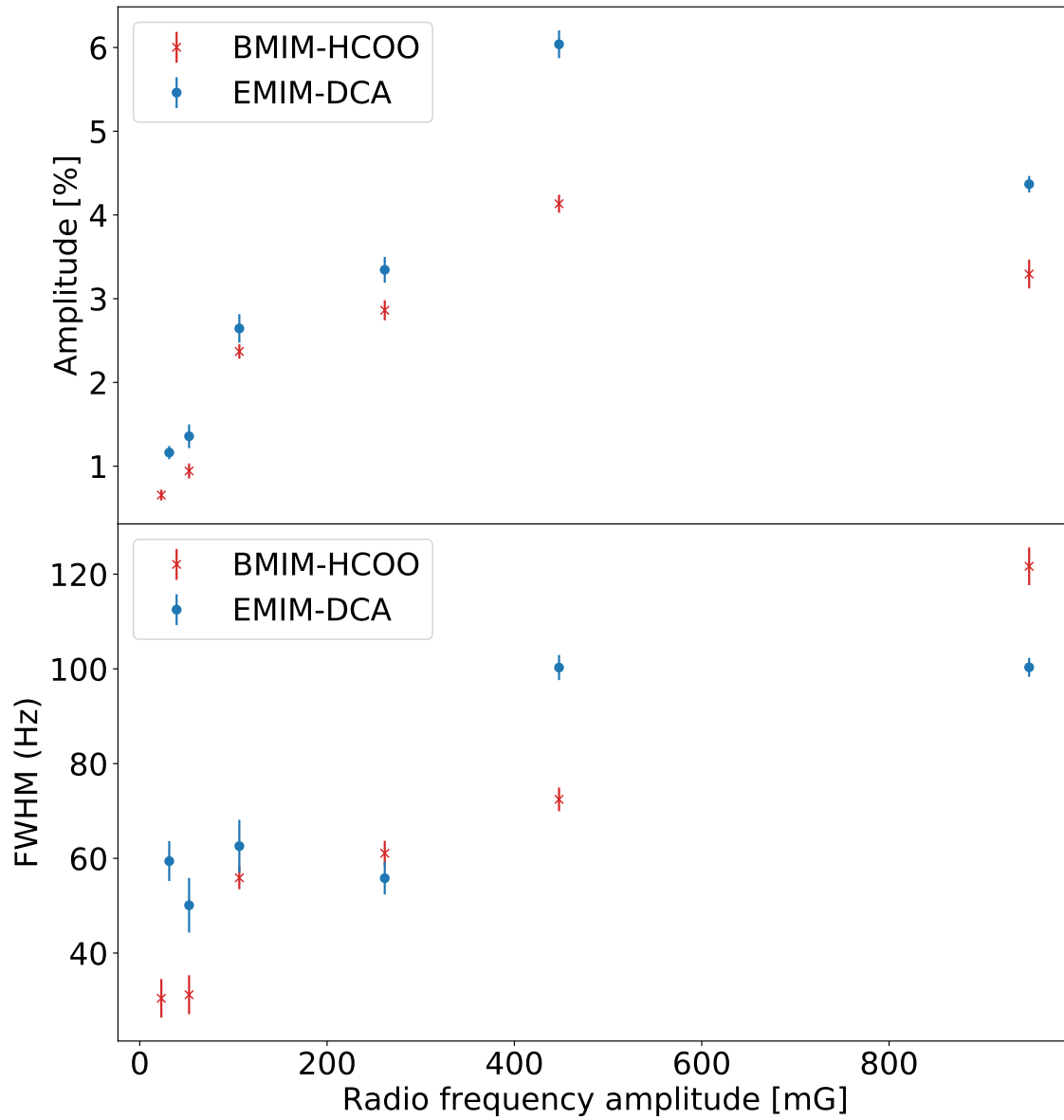
FIGURE 6.15: Amplitude and FWHM of the ^{26}Na NMR resonance as function of RF amplitude from samples of BMIM-HCOO and EMIM-DCA.

Field homogeneity and stability improvements

Two facets of the magnetic field are important for an NMR measurement, spatial homogeneity and the temporal stability of the field. A homogenous magnetic field ensures that the entire sample will resonate at the same Larmor frequency, thus a non-homogenous field will lead to a broadening of the NMR resonance. Furthermore, if the physical location of the sample within the magnetic field changes between measurements, e.g. when exchanging samples, there should be no shift in the Larmor resonance position in a homogenous field. Temporal stability ensures that the magnetic field remains constant for the duration of a measurement and between different measurements, in order to compare experimental data. To improve the quality and consistency of our data, the magnetic field from the 0.5 T magnet and the newly installed 1.2 T magnet were investigated, as shown in Fig. 6.16(a).

The field homogeneity between the magnet poles in the 0.5 T magnet is shown in blue within Fig. 6.16(a). The width of the sample is ≈ 8 mm, corresponding to a 10 ppm shift in the pole axis over the sample volume. When including the other two axes, the total ppm spread exceeded 30 ppm across the sample. To counteract the inhomogeneity of the field, shimming coils were added to each magnet pole. The shims added a perturbation to the primary B_0 magnetic field to increase the field homogeneity across the sample, and were wound by hand according to the specification in Ref [155]. The current through each coil was changed gradually until the field shift across the sample in 3 axes was reduced to 10 ppm with less than 3 ppm along the poles axis, orange in Fig. 6.16(a).

In mid-2018 the 0.5 T electromagnet was exchanged for a larger 1.2 T NMR electromagnet, which exhibited a broader homogenous region, see Fig. 6.16(b). New printed circuit board (PCB) shimming coils were also developed for use in conjunction with the 1.2 T magnet, to improve the spatial homogeneity across the sample to 7 ppm in the vertical and beam axes, and to ≈ 1 ppm in the pole axis, see Figure 6.16(c). The blue region
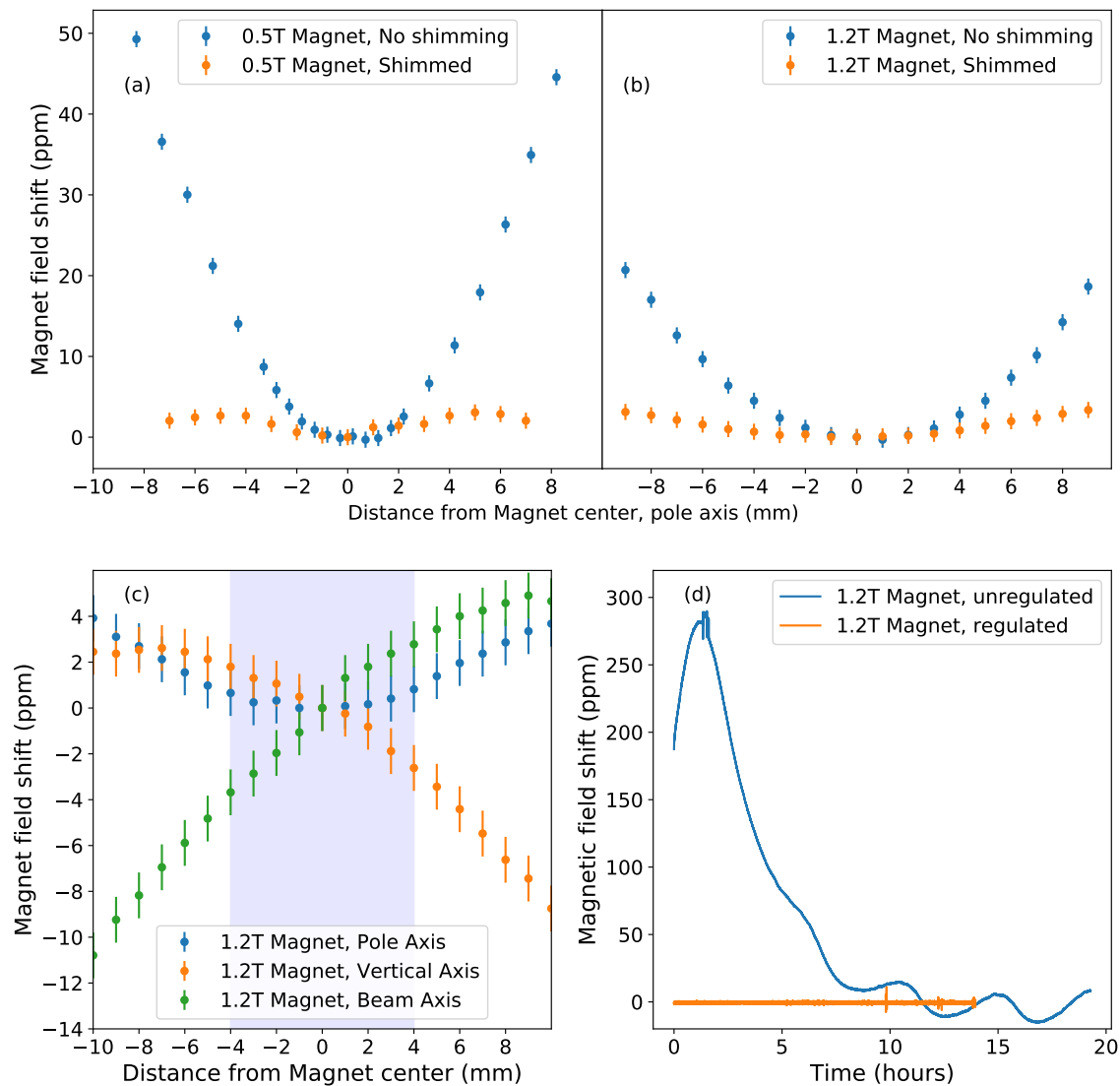
FIGURE 6.16: (a) The magnetic field shift of the 0.5 T magnet in ppm along the central axis between the poles. The reference magnetic field for the ppm shift is at 0 mm. The blue and orange points are before and after shimming, respectively. (b) The same as (a) but for the 1.2 T magnet. (c) The magnetic field variation of the 1.2 T magnet along all three axes after optimal shimming was performed. The shaded region indicates the expected size of the sample at the centre of the magnet. (d) The temporal drift of the 1.2 T magnet, before and after the installation of the stabilising probe.

indicates the area of the cross-section of the sample. By using a PCB instead of the previous hand-wound design, the shimming coil winding density was increased and had greater uniformity in shape across the coil. An example is shown in Fig. 6.17.

The temporal instability of the magnetic field was of a similar magnitude in both magnets, an example of an overnight measurement from the 1.2 T is shown in blue within Fig. 6.16(d). The field drift has a range of several hundred ppm and consisted of two components. The largest component occurred on a 24 hr period with the day and night cycle, related to the ambient temperature of the ISOLDE hall. A second component with an ≈ 5 hour periodic structure, correlated with the temperature of the magnet cooling water, which varied by several $^\circ$C. The field could be stabilised by either isolating the magnet and power supply from the environment, or by actively adjusting the current flowing through the magnet to counteract the environmental effects. The latter was chosen for simplicity and the advantage of gaining information about the absolute magnetic field strength throughout the duration of the measurements.

The temporal drift in the magnetic field was addressed using an active magnetic field stabilization feedback system. As an input, the system uses the resonance frequency from a custom ^{1}H NMR probe located just outside the primary RF coil (inside the vacuum chamber) 25 mm from the middle of the sample, see Fig. 6.17. The probe is a 3-mm diameter glass vial filled with 50 μL of water, diluted with iron to shorten the relaxation time into the ms range, allowing several measurements per second. The vial is surrounded by a copper coil acting as both a transmitter and receiver for the applied RF. A Free Induction Decay (FID) signal is recorded from the resonant pulsed excitation of the ^{1}H nuclei inside the probe, recorded every 200 ms. The FID is then processed by a custom LabVIEW 2017 program [156], which computes the Larmor frequency from a Fourier transform of the signal. A PID loop is used to adjust a variable resistor connected in parallel to the 1.2 T magnet, modifying the current flowing through the circuit and thus stabilizing the magnet to the chosen B-field value. A more detailed discussion of the system will presented in

the PhD thesis of Jared Croese (CERN, University of Geneva). Application of the feedback system reduced the temporal fluctuations to 1 ppm on a sub-second timescale. A comparison before and after the temporal stabilisation is shown in Fig. 6.16(d).

Development of an NMR Chamber for liquid samples
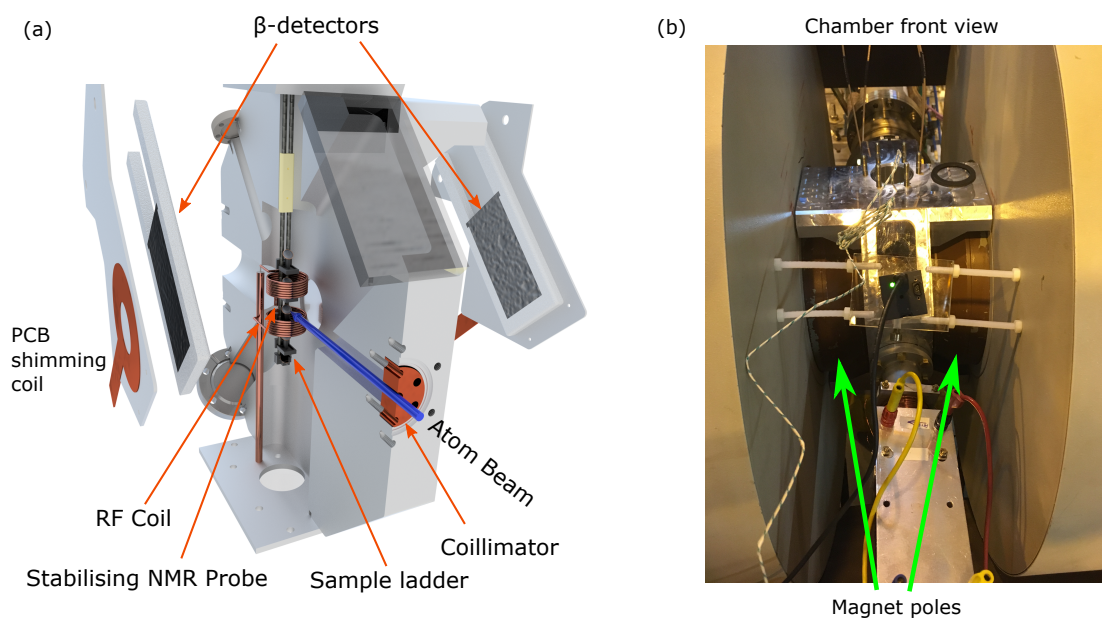
FIGURE 6.17: *β*-NMR liquid sample chamber, built for use with the 1.2 T magnet. (a) shows a CAD schemtic drawing of the chamber, (b) shows the chamber installed at the VITO beamline, resting on the poles of the magnet.

In order to accommodate the 1.2 T magnet, PCB shimming coils and NMR stabilisation system in the experimental setup, a new detection chamber was developed, see Fig. 6.17. The chamber was machined out of a single block of aluminium, with the outer edges shaped

to the dimensions of the magnet poles, see 6.17(b). Once secured in position, the center of the chamber would be perfectly aligned with the center of the magnetic field and the atom beam from VITO. In the front, the chamber has an exchangeable collimator that would reduce the beam size in accordance with the sample under investigation.

The RF coil was attached to a removable bottom plate, with the stabilising NMR probe attached to the connecting wire between the upper and lower parts of the RF coil. Co-axial feedthroughs for signals from both coils were integrated into the bottom plate. On either side of the RF coil were two circular β windows, consisting of 500 μm thick aluminium foil with a diameter of 40 mm. On the outside of each β window a detector pocket measuring 200 mm in width and 9 mm in depth accommodated two organic β scintillators as in the previous system. The detector closest to the β window was 2 mm thick, whilst the outer detector was 6 mm thick. To secure the β-detectors into the pocket, a 3 mm thick outer edge shimming plate was attached to either side of the chamber. The plates contained a 2 mm deep groove, machined to the dimension of the PCB coil.

Finally, a new sample delivery system was constructed, replacing the liquid capillary system with a sample ladder. Four samples would be placed into the chamber at any one time. Each sample holder consisted of a substrate on which the ionic liquid was placed, with a plastic tray underneath to catch any liquid that might spill onto the samples below. At the bottom of the ladder the NaF crystal was placed as a diagnostic measuring tool. The first experiments to include the 1.2 T magnet, shimming coils, stabilisation system and detection chamber took place in October 2018.

6.4 Precision measurement of the magnetic moment of ^{26}Na

To characterise the newly installed equipment at VITO, an experiment to measure EMIM-DCA, BMIM-HCOO and samples of each liquid containing DNA was performed in late 2018. To compliment the biological studies, it was proposed to attempt to remeasure the magnetic moment of ^{26}Na with far greater precision. The present value, 2.851(2) μ_N, was deduced in a collinear laser spectroscopy study [157]. As the magnetic field and resonance position are known with ppm precision in our experiments, it would be possible to improve the precision of the currently published magnetic moment of ^{26}Na, potentially by over two orders of magnitude.

Previous studies of nuclei using polarized β-NMR have relied on solid-state crystals. In the case of sodium, studies were performed on the neutron deficient nuclei $^{26-31}$Na using a cubic NaF crystal [104, 21], and produced resonances with the full width half maximum (FWHM) on the order of 10^{-4} of the resonance frequency [104]. In comparison, resonances from RTIL have widths that are more than two orders of magnitude narrower, as was shown in the previous part of this chapter.

Recall from Eqn. 3.25 in Sec. 3.3.1, that the magnetic moment can be determined using NMR if the nuclear spin, magnetic field and Larmor resonance frequency are known. The Larmor frequency is directly observable in β-NMR. Furthermore, due to the new NMR-based stabilisation system, the magnetic field was known throughout all the measurements, calculated from the RF resonance of the ^{1}H stabilising probe. As the probe was located 25 mm from the sample, a field correction was added to the measured field. It should be noted that the measured ^{26}Na and ^{1}H frequencies reflect the influence of their respective environments, i.e. the RTIL or water host and thus have to be corrected for this chemical shift.

Furthermore, the diamagnetic correction must also be included in order to precisely determine the magnetic moment. This correction factor is due to the currents induced

by the atomic electrons in the external magnetic field, and depends on the probe nucleus and the surrounding environment. Previously, it has been calculated theoretically with a precision of ≈ 1 %. As the correction factor is constant across an isotopic chain, we can instead consider the ratio of moments, R, between ^{26}Na and stable ^{23}Na as studied in the same environment.

In order to determine $\mu_I(^{26}$Na$)$, a reliable reference $\mu_I(^{23}$Na$)$ value is needed. In the Nuclear Data Tables [43], the values of $\mu_I(^{23}$Na$)$ based on ABMR and NMR experiments differ by 1.34×10^{-4} μ_N, which is much larger than their individual error bars. The above discrepancy stems from applying an obsolete diamagnetic correction [158] for the derivation of $\mu_I(^{23}$Na$)$ from the experiments. This inconsistency can be corrected using *ab initio* NMR shielding constants calculated for the species used in both experiments: a sodium atom in ABMR and an aqueous sodium ion in the NMR experiment.

Our recent β-NMR study of sodium isotopes includes new *ab initio* NMR shielding calculations for the Na$^+$ ion in various aqueous complexes [159]. These NMR shielding calculations have been used to correct the reference ^{23}Na magnetic moment from the original Atomic Beam Magnetic Resonance (ABMR) [160] and NMR experiments [161]. The previous literature values of $\mu_I(^{23}$Na$)$ are shown in Tab. 6.3 alongside the newly derived magnetic moments using the results of these calculations. Compared to the previous studies, agreement is seen between these two values with $\mu_I(^{23}$Na$) = +2.217500(7)$ μ_N used to derive the magnetic moment of ^{26}Na in this work (see below). Details of the shielding calculations can be found within [159] and the references therein.

At the time of investigation, it was not possible to obtain a conventional NMR signal from ^{23}Na at ISOLDE. Therefore, single $\frac{\pi}{2}$ RF pulse NMR studies were performed in a magnetic field of 7.05 T using a Bruker Avance DMX 300 MHz spectrometer at the Organic Chemistry Department of the University of Geneva (UNIGE). These data will form a part of the PhD thesis of Katarzyna Dziubinska-Kuhn (CERN, University of Leipzig).

TABLE 6.3: $\mu_I(^{23}Na)/\mu_N$ reference nuclear magnetic dipole moment from ABMR and NMR experiments. [a] using the original ABMR experiment [160] and NMR shielding of the sodium atom (637.1 ± 0.2) ppm, [b] using the standard NMR frequency ratio of ^{23}Na in NaCl water solution to proton in TMS [161] and NMR shielding of $Na^+(H_2O)_6$ (582.0 ± 2.6) ppm. See [159] for details of the NMR shielding calculations.

	Old reference $\mu_I(^{23}Na)/\mu_N$ [43]	New reference $\mu_I(^{23}Na)/\mu_N$
ABMR	+2.217522(2)	2.217495(2)[a]
NMR	+2.2176556(6)	2.217500(7)[b]

The ratio of the magnetic moments of ^{26}Na to ^{23}Na takes the following form:

$$R = \frac{\mu_I(^{26}Na)}{\mu_I(^{23}Na)} = \frac{v_{26}I_{26}}{v_{23}I_{23}} \frac{B_{23}}{B_{26}} \tag{6.8}$$

where I is the nuclear spin, B is the magnetic field at which ^{26}Na (B_{26}) and ^{23}Na (B_{23}) NMR was performed, v_L is the Larmor frequency, and μ_I is the nuclear magnetic moment.

For measuring the Larmor frequency of ^{26}Na, EMIM-DCA and BMIM-HCOO were chosen as the RTIL hosts as they produced resonances with the most desirable properties in the prior section. 20 μL of pure EMIM-DCA was prepared and deposited as a thin film onto a non-magnetic substrate, held at 45 degrees to the horizontal beam axis (see Fig. 6.17). The EMIM-DCA was obtained from a commercial company, with each sample containing an impurity of ≈ 1 μM of Na^+ [162]. For BMIM-HCOO, the sample was prepared by mixing BMIM-HCOO with purified water containing sodium chloride (NaCl). The resulting solution had a 0.5 M concentration of Na^+, of which 20 μL was placed onto a non-magnetic substrate. Due to the high viscosity of the liquids, the film remained on each substrate within a vacuum of 10^{-5} mbar for up to 24 h. An RF amplitude of 3000 mG was used resulting in a FWHM of < 50 ppm and resonance amplitudes of $\approx 3 - 4$ %, as shown in Fig. 6.18. The recorded Larmor frequencies are shown in Tab. 6.4.
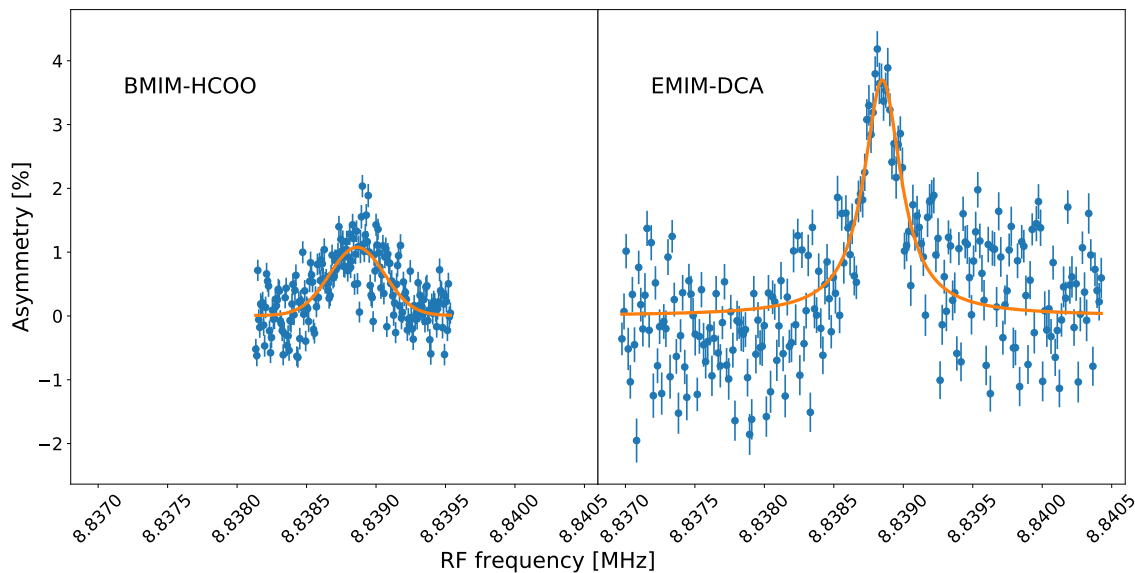
FIGURE 6.18: Typical β-NMR resonance from ^{26}Na in EMIM-DCA and BMIM-HCOO. The resonances are shown on the same scale axes for comparison. The magnetic field was locked to the same ^{1}H frequency for both samples.

During the ^{26}Na measurements, the ^{1}H stabilising NMR probe had a resonance frequency of 52008500(30) Hz. As the probe was located 25 mm from the liquid solution during the measurement (see Fig. 6.17), a correction offset of 1050(300) Hz (determined from a 3D magnetic field map of the system) was applied, producing a corrected frequency of 52009550(300) Hz.

^{23}Na and ^{1}H spectra at UNIGE were recorded using a basic pulsed-NMR scheme (single $\frac{\pi}{2}$ RF pulse) with samples at atmospheric pressure and room temperature. For the EMIM-DCA sample, NaCl was dissolved in 50 μL of purified water, giving a NaCl concentration of 12 μM. Next, 550 μL of EMIM-DCA was added to this solution and stirred at room temperature in open air conditions. The final concentration of NaCl in the mixed

solvent sample was $\approx 1 \ \mu M$, as in the ISOLDE sample. 200 μL of the mixed solution was sealed inside an 3-mm diameter NMR tube. This tube was placed inside a 5-mm diameter tube filled with D_2O, whose NMR signal was used to stabilise the magnetic field automatically during the measurements. For BMIM-HCOO, NaCl was dissolved in 200 μL of purified water, giving a 6 M concentration of NaCl. 550 μL of BMIM-HCOO was added to the solution, prepared in conditions identical to EMIM-DCA, with the resulting concentration of NaCl being 0.5 M. Previous conventional NMR studies at UNIGE with ^{23}Na showed that outgassing samples containing ^{23}Na would shift the ^{23}Na resonance by less than 0.5 ppm, smaller than the experimental uncertainty that we have assumed in the resonance location. Thus, outgassing was not carried out on these samples. The recorded resonance frequencies of EMIM-DCA and BMIM-HCOO (including the observed chemical shift of each liquid) are shown in Tab. 6.4.

^1H NMR resonances were also recorded from 3-mm tubes filled with H_2O placed inside 5-mm tubes filled with D_2O. The recorded Larmor frequency of ^1H, was 300131415(100) Hz. Since the frequency of ^1H in H_2O has been determined in each system the magnetic field can be calculated via a rearrangement of Eqn. 3.25:

$$B_{26} = \frac{\nu_{1H,1.2T} I_{1H} h}{\mu_{1H}}, B_{23} = \frac{\nu_{1H,7.05T} I_{1H} h}{\mu_{1H}} \tag{6.9}$$

where $\nu_{1H,1.2T}$ and $\nu_{1H,7.05T}$ correspond to the recorded NMR frequency of ^1H in the 1.2 T and 7.05 T, respectively. Applying the above to Eqn. 6.8 gives:

$$R = \frac{\nu_{26} I_{26}}{\nu_{23} I_{23}} \frac{\nu_{1H,7.05T}}{\nu_{1H,1.2T}} \tag{6.10}$$

The derived value of R for each measurement is shown in Tab. 6.4. The weighted average of R was determined to be $R = 1.284951(1)[8]$, or $R = 1.284951(8)$ with the uncertainties combined, see the inset of Fig. 6.19. By combining R, with the updated

TABLE 6.4: Larmor frequencies of ^{26}Na at 1.2 T and ^{23}Na at 7.05 T in BMIM-HCOO and EMIM-DCA, and the resulting ratio of the magnetic moments, R. Errors in round brackets are due to the statistical uncertainties in the resonance frequencies. For R this includes only the uncertainty of the ^{26}Na resonance frequency, while the square brackets are due to other contributions, including the uncertainty of the ^{23}Na resonance frequency.

Liquid host	$v(^{26}\text{Na})$ (Hz)	$v(^{23}\text{Na})$ (Hz)	R
BMIM-HCOO	8838818(14)	79390170(100)	1.284949(2)[8]
BMIM-HCOO	8838857(12)		1.284954(2)[8]
EMIM-DCA	8838841(10)	79390300(100)	1.284950(2)[8]
EMIM-DCA	8838849(13)		1.284951(2)[8]

$\mu_I(^{23}\text{Na}) = +2.217500(7)\,\mu_N$ from this work and [159], we obtain $\mu_I(^{26}\text{Na}) = +2.849378(20)\,\mu_N$. This agrees within the experimental uncertainty of the literature value, $\mu_I(^{26}\text{Na}) = +2.851(2)\,\mu_N$, as deduced from the hyperfine structure of the atomic ground state of ^{26}Na, using collinear laser spectroscopy [157]. Our relative uncertainty is on the order of 3 ppm, representing an increase in precision of over 2 orders of magnitude.

Magnetic moments which have been linked to ^{26}Na can also benefit from the improved precision of this measurement. This is the case $^{27-31}$Na, which were investigated using β-NMR in solid-state hosts at the collinear laser spectroscopy beamline at ISOLDE [104] and whose magnetic moments were referenced to that of ^{26}Na. Using the magnetic moment deduced in this work with the g-factors as derived in [104], the magnetic moments shown in Tab. 6.5 were obtained. We note here that the values in Tab. 6.5 have a precision in the 20 ppm range, an improvement of a factor of 50 as compared to the values deduced in [104] and up to 200 times more precise than the values tabulated in the latest compilation of nuclear magnetic dipole and electric quadrupole moments [43]. The present uncertainty in the moments of $^{27-31}$Na is dominated by the error of the resonance position in the original
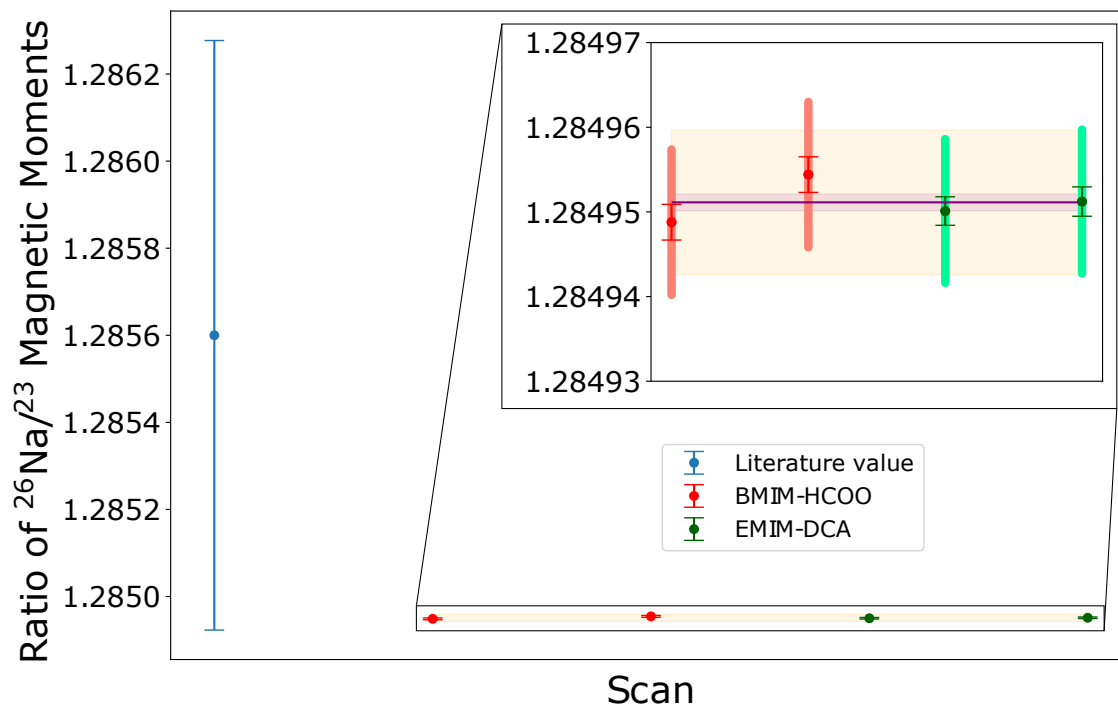
FIGURE 6.19: Ratio (R) of the magnetic moments of ^{26}Na and ^{23}Na. Left: literature value [157], right: present study. Thin error-bar lines correspond to statistical uncertainty in the ^{26}Na Larmor frequency and thick lines are the systematic uncertainties. The weighted average is represented by the purple line. The statistical uncertainty from all four measurements is indicated by the pink band, while the systematic uncertainty is shown by the broader orange band. For more details, see text.

solid-state β-NMR study. If new measurements in liquid-state hosts are performed, this uncertainty could be decreased even further to the ppm level.

The precise magnetic moments of $^{26-31}$Na presented in Tab. 6.5, together with that of ^{23}Na, provide a self-consistent set of isotopes with which to perform future β-NMR studies. These can be used to probe the chemical and biological processes on different

TABLE 6.5: Magnetic moments of $^{23,26-31}$Na determined in this work, compared to literature values [104], and other nuclear properties relevant for NMR. ^{a} Current NMR literature value quoted in the Nuclear Data Tables [161], ^{b} Corrected $\mu_I(^{23}$Na) based on our recent NMR experiment, see Table 6.3 ^{c} Based on our improved ratio of the magnetic moments of ^{26}Na to ^{23}Na^b

Isotope	I	$T_{1/2}$(ms)	μ_I(lit)/μ_N	μ_I(this work)/μ_N	$Q(mb)$
^{23}Na	3/2	stable	2.2176556(6)^a	2.217500(7)^b	+105.6(12)
^{26}Na	3	1071	2.851(2)	2.849378(20)^c	-5.3(2)
^{27}Na	5/2	301	3.894(3)	3.89211(11)	-7.2(3)
^{28}Na	1	31	2.420(2)	2.41843(9)	+39.5(12)
^{29}Na	3/2	44	2.457(2)	2.45534(8)	+86(3)
^{30}Na	2	48	2.069(2)	2.0681(5)	
^{31}Na	3/2	17	2.298(2)	2.29668(8)	

timescales and via different types of interactions, as each isotope has a different nuclear spin, half-life and electric quadrupole moment (see Tab. 6.5). For example, the quadrupole moments of ^{26}Na and ^{27}Na are respectively 20 and 15 times smaller compared to stable ^{23}Na. This should permit the observation of NMR signals in hosts which display a fast quadrupolar relaxation in ^{23}Na NMR, resulting in very broadened resonances.

The same approach can be applied to other isotopic chains, thus increasing the palette of nuclei available for NMR studies. In addition, when combined with hyperfine-structure measurements, their magnetic moments could be used to determine the Bohr-Weisskopf effect itself. This topic has seen a regained interest in the last few years, both for nuclear structure studies and for QED tests in heavy few-electron atoms, such as ^{209}Bi^{80+} [163].

7 Conclusion

This thesis presents results from two different spectroscopic studies employing lasers at the ISOLDE facility.

The first was a detailed spectroscopic study of ^{180,182}Au, performed using the RILIS, Windmill decay station and MR-ToF MS setups. Due to the pure and intense beam provided, complex fine-structure α decays have been identified and their properties, e.g. relative intensities and HF_α values were deduced. From the hfs structure observed, the magnetic moment has been extracted and a spin assignment of $I^\pi = (1^+)$ is proposed for ^{180}Au, with a $(\pi 3/2^-[532] \otimes \nu 5/2^-[512])$ configuration. The complementary hfs data for ^{182}Au was also analysed, which confirmed the $I^\pi = 2^+$ spin and proposes a $3/2^-[532]h_{9/2} \otimes 1/2^-[521]p_{3/2}$ configuration.

In the second approach, a review of recent developments at ISOLDE's new laser polarisation beamline has been presented. With the desire to perform laser-polarised β-NMR studies on biological samples in water-based host solutions, a prototype differential pumping system was developed and installed at the beamline. β-NMR resonances from ^{27}Na implanted into a NaF crystal were measured as a function of the pressure in the detection chamber, with resonances observed up to a pressure of 0.5 mbar. Furthermore, a detailed investigation of several vacuum-compatible liquid hosts has been performed. Ionic liquids BMIM-HCOO and EMIM-DCA, were identified as the most promising potential vacuum-compatible liquid-state hosts for future biological experiments with β-NMR.

Additionally, due to the improvement in β-NMR resolution offered by these liquid-state

hosts, the magnetic moment of a short-lived nucleus ^{26}Na has been measured with ppm precision for the first time. By combining this result with previous β-NMR measurements, the magnetic moments of $^{27-31}$Na have also been determined close to this precision. This approach can also be applied to other isotopes and chemical elements, paving the way for the precise determination of their magnetic moments and thus their use in biochemistry studies with β-NMR. This result is also relevant for other studies which would require an accurate knowledge of nuclear magnetic moments along isotopic chains, such as the determination of the distribution of magnetisation inside atomic nuclei interesting for nuclear-structure studies.

7.1 Outlook

The analysis of ^{180,182}Au presented in this thesis, is planned for a dedicated forthcoming publication, currently in the final stages of internal review. This is the second stage of an ongoing multistep process to analyse the combined laser and decay spectroscopy study of $^{176-198}$Au, which commenced with a hyperfine structure study of ^{179,177}Au [36]. A publication dedicated to α-decay spectroscopy of ^{176,177}Au^{g,m} and ^{179}Au is also in an advanced stage of preparation. The final part of this process will culminate in a separate discussion of the isotope shift and charge radii measurements of $^{176-198}$Au.

To expand upon the information about ^{180}Au disclosed in this work, a detailed investigation of the excitation level structure could compliment the previous studies of the β-decay from ^{180}Hg [112] and α-decay from ^{184}Tl [32]. A dedicated in-beam spectroscopy experiment at a facility such as Jyväskylä, with access to the RITU gas-filled separator and EUROGAM Ge-array could provide important information about the level structure built on the ground state and also aid in the search for a potential short-lived isomer not seen at ISOLDE. Such an investigation was recently carried out on neighbouring isotope ^{179}Au,

which revealed a previously unobserved 328(2) ns isomer, 89.5 keV above the ground state [164].

Further laser-spectroscopy studies of the iridium neutron deficient nuclei could lend support to the α-decay analysis presented in this work. Previously, $^{182-193}$Ir were investigated via resonant ionisation source laser spectroscopy at ISOLDE by the COMPLIS collaboration [165, 166]. In this experiment they measured the ground state spin, parity, magnetic moments and quadrupole moments of the neutron-deficient iridium isotopic chain. Extending these measurements further to ^{176}Ir and beyond using the combined Windmill-RILIS-MR-ToF setup, could inform on the ^{180}Au f.s. α-decay channels observed in this work. The predicted yield from the online ISOLDE database [167], indicates that isotopes as neutron deficient as ^{170}Ir could be accessible in future experiments at the facility.

As shown in this work, VITO provides an accurate method for measuring magnetic moments with ppm precision. This approach could be extended to other isotopic chains, in particular isotopes with proven polarisation schemes such as Rb, K or Mg [142]. If further laser polarisation schemes were developed, this method could be applied to other nuclei such as the Au isotopes presented in this thesis. During CERN's long shutdown, a new offline polarisation observation device is being developed in conjunction with an offline ion source. This will allow VITO to test new polarisation schemes for future experiments.

In parallel to the results on RTIL presented in this thesis, biological samples containing various structures of DNA were also studied. The analysis of these results is ongoing and will form part of the PhD theses of Jared Croese (CERN, University of Geneva) and Katarzyna Dziubinska-Kuhn (CERN, University of Leipzig). These data include relaxation time measurements of ^{26}Na implanted into folded and unfolded DNA G-quaduplex structures in conjunction with β-NMR measurements of the samples in assorted host environments [45]. To compliment this data, further offline measurements of stable ^{23}Na in RTIL and DNA are also ongoing.

Other nuclear structure studies can also benefit from the laser polarisation technique.

One example is a novel approach using the β-decay asymmetry parameter to determine the spin of states populated through β decay [168]. The β-decay asymmetry is measured in coincidence with either a γ ray of a specific energy or β-delayed neutron with a specific time of flight. From the measured β-decay asymmetry, the asymmetry parameter is determined which is sentive to the spin of the initial and final states of the β decay. Therefore, in addition to gaining information about the energy levels determined from the discrete energies of the neutrons and γ rays, one also obtains information about the spins of states. Development of such an experiment in conjuction with the VITO beamline has been proposed through a letter of intent, with further preparation for such an experiment ongoing [169].

Bibliography

[1]   K. Heyde et al., "Coexistence in odd-mass nuclei", *Phys. Rep.* 102(5), pp. 291 –393, 1983.

[2]   K. Heyde et al., "A shell-model description of 0+ intruder states in even-even nuclei", *Nucl. Phys. A* 466(2), pp. 189 –226, 1987.

[3]   K. Heyde and R. A. Meyer, "Monopole strength as a measure of nuclear shape mixing", *Phys. Rev. C* 37, pp. 2170–2175, 1988.

[4]   J. L. Wood et al., "Detailed nuclear structure studies far from stability", *Hyp. Int.* 75(1), pp. 51–58, 1992.

[5]   A. N. Andreyev et al., "A triplet of differently shaped spin-zero states in the atomic nucleus ^{186}Pb", *Nature* 405, pp. 430–433, 2000.

[6]   K. Heyde and J. L. Wood, "Shape coexistence in atomic nuclei", *Rev. Mod. Phys.* 83(4), pp. 1467–1521, 2011.

[7]   T. Otsuka and Y. Tsunoda, "The role of shell evolution in shape coexistence", *J. Phys. G: Nucl. Part. Phys.* 43(2), pp. 1–18, 2016.

[8]   B. A. Marsh et al., "Characterization of the shape-staggering effect in mercury nuclei", *Nat. Phys.* 14, pp. 1163–1167, 2018.

[9]   J. Bonn et al., "Sudden Change in The Nuclear Charge Distrubution of the very light Mercury Isotopes", *Phys. Lett.* 38B(5), pp. 308–311, 1972.

[10] J. Bonn et al., "Spins, moments and charge radii in the isotopic series ^{181}Hg-^{191}Hg", *Z. Phys. A* 276(3), pp. 203–217, 1976.

[11] G. Ulm et al., "Isotope shift of ^{182}Hg and an update of nuclear moments and charge radii in the isotope range ^{181}Hg-^{206}Hg", *Z. Phys. A* 325(3), pp. 247–259, 1986.

[12] T. Kühl et al., "Nuclear Shape Staggering in Very Neutron-Deficient Hg Isotopes Detected by Laser Spectroscopy", *Phys. Rev. Lett.* 39(4), pp. 180–183, 1977.

[13] H. De Witte et al., "Nuclear Charge Radii of Neutron-Deficient Lead Isotopes Beyond $N = 104$ Midshell Investigated by In-Source Laser Spectroscopy", *Phys. Rev. Lett.* 98, pp. 112502–1–112502–4, 2007.

[14] T. E. Cocolios et al., "Early Onset of Ground State Deformation in Neutron Deficient Polonium Isotopes", *Phys. Rev. Lett.* 106, pp. 052503–1–052503–4, 2011.

[15] F.F. Karpeshin and M.B. Trzhaskovskaya, "The theory of the Bohr–Weisskopf effect in the hyperfine structure", *Nucl. Phys.s A* 941, pp. 66–77, 2015.

[16] A. Bohr and V. F. Wiesskopf, "The Influence of Nuclear Structure on the Hyperfine Structure of Heavy Elements", *Phys. Rev.* 77(1), pp. 94–98, 1950.

[17] M. Stachura et al., "Toward Applications of β-NMR Spectroscopy in Chemistry and Biochemistry", *Nuclear Physics News* 25(2), pp. 25–29, 2015.

[18] W. Gins et al., "A new beamline for laser spin-polarization at ISOLDE", *Nucl. Instrum. Meth. A* 925, pp. 24–32, 2019.

[19] W. Gins, "Development of a dedicated laser-polarization beamline for ISOLDE-CERN", *Thesis* 2019.

[20] M. Kowalska et al., "New laser polarization line at the ISOLDE facility", *J. Phys. G: Nucl. Part. Phys.* 44, pp. 1–10, 2016.

[21] M. Kowalska, *Proposal to the ISOLDE and Neutron Time-of-Flight Committee: Interaction of Na ions with DNA G-quadruplex structures studied directly with Na beta-NMR spectroscopy*, 2017, pp. 1–9.

[22] C. Ekstrom, L. Robertsson, and G. Wannberg, "Nuclear ground-state spin of ^{185}Au and magnetic moments of ^{187,188}Au: Further evidence for coexisting nuclear shapes in this mass region", *Nucl. Phys. A* 348(1), pp. 25–44, 1980.

[23] K. Wallmeroth, "Sudden Change in the Nuclear Charge Distribution of Very Light Gold Isotopes", *Phys. Rev. Lett.* 58(15), pp. 1516–1519, 1987.

[24] U. Krönert et al., "Observation of strongly deformed ground-state configurations in ^{184}Au and ^{183}Au by laser spectroscopy", *Z. Phys. A* 331(4), pp. 521–522, 1988.

[25] K. Wallmeroth et al., "Nuclear shape transition in light gold isotopes", *Nucl. Phys. A* 493(2), pp. 224–252, 1989.

[26] F. Le Blanc et al., "Nuclear Moments and Deformation Change in $^{184}Au^{g,m}$ from Laser Spectroscopy", *Phys. Rev. Lett.* 79(12), pp. 2213–2216, 1997.

[27] G. Savard et al., "Laser spectroscopy of laser-desorbed gold isotopes", *Nucl. Phys. A* 512(2), pp. 241–252, 1990.

[28] J. Sauvage et al., "Low-spin states of doubly odd ^{184}Au", *Eur. Phys. A* 25(1), pp. 5–21, 2005.

[29] J. L. Wood et al., "Electric monopole transitions from low energy excitations in nuclei", *Nucl. Phys. A* 651(4), pp. 323–368, 1999.

[30] I. Romanski et al., "Time-resolved and time-integral on-line nuclear orientation measurements of neutron-deficient Hg−Au−Pt−Ir nuclei", *Hyp. Int.* 75(1), pp. 457–470, 1992.

[31] F. Ibrahim et al., "Low-spin states of doubly odd ^{182}Au", *Eur. Phys. A* 10(2), pp. 139–143, 2001.

[32] C. Van Beveren et al., "Related content α-decay study of ^{182,184}Tl", *J. Phys. G: Nucl. Part. Phys.* 43, pp. 025102–1–025102–22, 2016.

[33] J. G. Keller et al., "Cold Fusion in symmetric ^{90}Zr-Induced Reactions", *Nucl. Phys. A* 452, pp. 173–204, 1986.

[34] J. Wauters et al., "Alpha-decay study of ^{188}Pb and ^{180,182}Hg", *Z. Phys. A* 345, pp. 21–27, 1993.

[35] B. A. Marsh et al., "New developments of the in-source spectroscopy method at RILIS/ ISOLDE", *Nucl. Instrum. Meth. B* 317, pp. 550–556, 2013.

[36] J. G. Cubiss et al., "Change in structure between the I = 1 / 2 states in ^{181}Tl and ^{177,179}Au", *Phys. Lett. B* 786, pp. 355–363, 2018.

[37] G. Neyens, "Nuclear magnetic and quadrupole moments for nuclear structure research on exotic nuclei", *Rep. Prog. Phys.* 66, pp. 633–689, 2003.

[38] R. Neugart, *Nuclear moments and laser spectroscopy*, tech. rep., 1990, pp. 41–57.

[39] E. Arnold et al., "Nuclear spin and magnetic moment of ^{11}Li", *Phys. Lett. B* 197(3), pp. 311–314, 1987.

[40] W. Geithner et al., "Measurement of the magnetic moment of the one-neutron halo nucleus ^{11}Be", *Phys. Rev. Lett.* 83, pp. 3792–3795, 1999.

[41] G. Neyens et al., "Measurement of the spin and magnetic moment of ^{31}Mg: Evidence for a strongly deformed intruder ground state", *Phys. Rev. Lett.* 94, pp. 022501–1–022501–4, 2005.

[42] M. Ismail et al., "Islands of stability and quasi-magic numbers for super- and ultra-heavy nuclei", *Chin. Phys. C* 40(12), pp. 124102–1–124102–22, 2016.

[43] N. J. Stone, "Table of Nuclear Magnetic Dipole and Electric Quadrupole Moments", *Atomic Data And Nuclear Data Tables* 90(1), pp. 75–176, 2005.

[44] Jancso, A. and Correia, J. G and Gottberg, A. and others, "TDPAC and β-NMR applications in chemistry and biochemistry", *J. Phys. G: Nucl. Part. Phys.* 44(6), pp. 64003–1–64003–25, 2017.

[45] M Kowalska et al., "Addendum to P-521 to the ISOLDE and Neutron Time-of-Flight Committee Interaction of Na + ions with DNA G-quadruplex structures studied directly with Na beta-NMR spectroscopy", pp. 1–8, 2018.

[46] D. Szunyogh et al., "Direct observation of Mg^{2+} complexes in ionic liquid solutions by ^{31}Mg β-NMR spectroscopy", *Dalton Transactions* 47(41), pp. 14431–14435, 2018.

[47] T. Sugihara et al., "NMR detection of short-lived β-emitter ^{12}N implanted in water", *Hyp. Int.* 238(20), pp. 1–5, 2017.

[48] G. Wu and J. Zhu, "NMR studies of alkali metal ions in organic and biological solids", *Prog. Nucl. Mag. Res. Spec.* 61, pp. 1–70, 2012.

[49] B. Cheal and K. T. Flanagan, "Progress in laser spectroscopy at radioactive ion beam facilities", *J. of Phys. G: Nucl. Part. Phys.* 37, pp. 113101–1–13101–38, 2010.

[50] I. Berkes, "Magnetic moment measurement by nuclear orientation", *Hyp. Int.* 22(1-4), pp. 547–557, Mar. 1985.

[51] W. F. Rogers et al., "β-NMR magnetic moment measurement using on-line mass separation and tilted foil polarization", *Nucl. Instrum. Meth. A* 253(2), pp. 256–263, Jan. 1987.

[52] K. Krane, *Introductory Nuclear Physics*, John Wiley and Sons, 1988.

[53] P. Möller et al., "Nuclear ground-state masses and deformations: FRDM(2012)", *Atomic Data and Nuclear Data Tables* 109-110(2012), pp. 1–204, 2016, eprint: arXiv:1508.06294v1.

[54] M. G. Mayer, "On Closed Shells in Nuclei. II", *Phys. Rev.* 75, pp. 1969–1970, 1949.

[55] S.G Nilson, "Binding States of Individual Nucleons in Strongly Deformed Nuclei", *Dan. Mat. Fys. Medd 29* 16, pp. 1–48, 1955.

[56] S. Hilaire and M. Girod, *Hartree-Fock-Bogolioubov results based on the Gogny force*, Accessed: 2019-07-30, URL: http://www-phynu.cea.fr/science_en_ligne/carte_potentiels_microscopiques/carte_potentiel_nucleaire_eng.htm.

[57] J. Dechargé and D. Gogny, "Hartree-Fock-Bogolyubov calculations with the $D1$ effective interaction on spherical nuclei", *Phys. Rev. C* 21, pp. 1568–1593, 4 1980.

[58] M. Venhart et al., "New systematic features in the neutron-deficient Au isotopes", *J. Phys. G: Nucl. Part. Phys.* 44, pp. 074003–1–074003–20, 2017.

[59] K. Heyde, *Basic Ideas and Concepts in Nuclear Physics*, vol. 3, CRC Press, 2004.

[60] J. O. Rasmussen, "Alpha-Decay Barrier Penetrabilities with an Exponential Nuclear Potential: Even-Even Nuclei", *Phys. Rev.* 113, pp. 1593–1598, 1959.

[61] "The Isotope Shift in Hyperfine Structure", *Phys. Rev.* 41(5), pp. 459–470, 1932.

[62] A E Barzakh et al., "Hyperfine anomaly in gold and magnetic moments of I $^{\pi}$ = $11/2^-$ gold isomers", *Phys. Rev. C* 034308, pp. 1–9, 2020.

[63] S. Büttgenbach, "Magnetic hyperfine anomalies", *Hyp. Int.* 20(1), pp. 1–64, 1984.

[64] B. A. Marsh, V. N. Fedosseev, and P. Kosuri, "Development of a RILIS ionisation scheme for gold at ISOLDE, CERN", *Hyp. Int.* 171(2006), pp. 109–116, 2007.

[65] V. Fedosseev et al., "ISOLDE RILIS: New beams, new facilities", *Nucl. Instrum. Meth. B* 266(19-20), pp. 4378–4382, 2008.

[66]   B. Marsh, "Resonance ionization laser ion sources", *CAS-CERN Accelerator School: Ion Sources - Proceedings*, p. 245, 2013.

[67]   A. R. Vernon et al., "Simulation of the relative atomic populations of elements $1 \leq Z \leq 89$ following charge exchange tested with collinear resonance ionization spectroscopy of indium", *Spect. Act. B: Atom. Spec.* 153, pp. 61–83, 2019.

[68]   P. Campbell, I. D. Moore, and M. R. Pearson, "Laser spectroscopy for nuclear structure physics", *Prog. in Part. and Nucl. Phys.* 86, pp. 127–180, 2016.

[69]   C. Babcock et al., "Evidence for Increased neutron and proton excitations between $^{51-63}$Mn", *Phys. Lett. B* 750, pp. 176–180, 2015.

[70]   R. Neugart et al., "Collinear laser spectroscopy at ISOLDE: new methods and highlights", *J. Phys. G: Nucl. Part. Phys.* 44, pp. 1–21, 2017.

[71]   J. G. Cubiss et al., "Charge radii and electromagnetic moments of $^{195-211}$At", *Phys. Rev. C* 97, pp. 054327–1–054327–19, 2018.

[72]   T. E. Cocolios et al., "The Collinear Resonance Ionization Spectroscopy (CRIS) experimental setup at CERN-ISOLDE", *Nucl. Instrum. Meth. B* 317, pp. 565–569, 2013.

[73]   K. M. Lynch et al., "Decay-Assisted Laser Spectroscopy of Neutron-Deficient Francium", *Phys. Rev. X* 4, pp. 011055–1–011055–15, 2014.

[74]   R F Garcia Ruiz et al., "Unexpectedly large charge radii of neutron-rich calcium isotopes", *Nat. Phys.* 12, pp. 594–598, 2016.

[75]   R. F. Garcia Ruiz et al., "High-Precision Multiphoton Ionization of Accelerated Laser-Ablated Species", *Phys. Rev. X* 8, pp. 041005–1–041005–18, 2018.

[76]   C. S. Wu et al., "Experimental Test of Parity Conservation in Beta Decay", *Phys. Rev.* 105, pp. 1413–1415, 1957.

[77] G. F. Grinyer et al., "High precision measurements of ^{26}Na β- decay", *Phys. Rev. C* 71(4), pp. 1–13, 2005.

[78] K. Kura et al., "Structure of ^{28}Mg studied by β-decay spectroscopy of spin-polarized ^{28}Na: The first step of systematic studies on neutron-rich Mg isotopes", *Phys. Rev. C* 85(3), pp. 1–9, 2012.

[79] M. Balcı, *Basic P1sH- and P1sp3sC-NMR Spectroscopy*, Elsevier, 2005.

[80] E. Mobs, *The CERN accelerator complex*, URL: http://cds.cern.ch/record/2197559/files/?docname=CCC-v2017&version=all (visited on 01/21/2019).

[81] ISOLDE, *The ISOLDE Nuclear Facility*, URL: http://isolde.web.cern.ch/sites/isolde.web.cern.ch/files/3D%20Layout%20of%20ISOLDE-Jura%20side%20view.jpg (visited on 01/21/2019).

[82] L. Alvarez-Gaume, *Infinitely CERN, Memories from fifty years of research*, 2004.

[83] B. Jonson and A. Richter, "More than three decades of ISOLDE physics", 129, pp. 1–22, 2000.

[84] M. J. G. Borge and B. Jonson, "ISOLDE past, present and future" 2017.

[85] E. Kugler, "The ISOLDE facility", *Hyp. Int.* 129(1), pp. 23–42, 2000.

[86] M. J. G. Borge, "Highlights of the ISOLDE facility and the HIE-ISOLDE project", *Nucl. Instrum. Meth. B* 376, pp. 408–412, 2016.

[87] M. Borge and Y. Kadi, "ISOLDE at CERN", 9127 2016.

[88] CERN, "CERN Annual report 2017", p. 23, 2017.

[89] A. Gottberg, "Target materials for exotic ISOL beams", *Nucl. Instrum. Meth. B* 376, pp. 8–15, 2016.

[90] J. F. Baugh et al., "Precision Stark spectroscopy of sodium ^{2}P and ^{2}D states", *Phys. Rev. A* 58(2), pp. 1585–1588, 1998.

[91] V. Fedosseev et al., "Ion beam production and study of radioactive isotopes with the laser ion source at ISOLDE", *J. Phys. G: Nucl. Part. Phys.* 44, pp. 1–28, 2017.

[92] S. Rothe et al., "Laser ion beam production at CERN-ISOLDE : New features – More possibilities", *Nucl. Instrum. Meth. B* 376, pp. 91–96, 2016.

[93] J. Schell, P. Schaaf, and D. C Lupascu, "Perturbed angular correlations at ISOLDE : A 40 years young technique", *AIP Advances* 7(10) 2017.

[94] T. E. Cocolios et al., "Optimisation of clinical SPECT imaging with theragnostic radionuclide therapy Theragnostic applications of the terbium isotopes Figure CERN-MEDICIS", pp. 1–6, 2016.

[95] J. Sundberg, "Negative ion photodetachment studies at ISOLDE", *Thesis* 2016.

[96] R Catherall et al., "The ISOLDE facility", 12 2017.

[97] E. Mané et al., "An ion cooler-buncher for high-sensitivity collinear laser spectroscopy at ISOLDE", *Eur. Phys. A* 42(3), pp. 503–507, 2009.

[98] K. T. Flanagan et al., "Nuclear Spins and Magnetic Moments of ^{71,73,75}Cu: Inversion of $\pi 2p_{3/2}$ and $\pi 1f_{5/2}$ Levels in ^{75}Cu", *Phys. Rev. Lett.* 103(14), pp. 142501–1–142501–4, 2009.

[99] *X-ray instruments Associates*, Accessed: 2019-07-30, URL: http://www.xia.com.

[100] *IGOR software package, Wavemetrics*, Accessed: 2019-07-30, URL: https://www.wavemetrics.com.

[101] F Wienholtz et al., "Masses of exotic calcium isotopes pin down nuclear forces", *Nat. Lett.* 498(345), pp. 1–5, 2013.

[102] R.N. Wolf et al., "ISOLTRAP's Multi-Reflection Time-of-Flight Mass Separator/Spectrometer", *Int. Jour. Mass Spect.* 349, pp. 123–133, 2013.

[103]   Ch Borgmann et al., "On-line separation of short-lived nuclei by a multi-reflection time-of- flight device", *Nucl. Instrum. Meth. A* 686, pp. 82–90, 2012.

[104]   M. Keim et al., "Measurement of the electric quadrupole moment of $^{26-29}$Na", *Eur. Phys. J. A* 8(1), pp. 31–40, 2000.

[105]   *Delay and gate generator, Quantum Composer*, Accessed: 2019-07-30, URL: https://www.quantumcomposers.com/pulse-delay-generator.

[106]   A. Siivola, "Alpha-active gold isotopes", *Nucl. Phys. A* 109(1), pp. 231–235, 1968.

[107]   A. Siivola, "Alpha-Active Platinum Isotopes", *Nucl. Phys.* 84(2), pp. 385–397, 1966.

[108]   A.G. Demin et al., "New mercury isotopes", *Nucl. Phys. A* 106(2), pp. 337–349, 1967.

[109]   A. Rytz, "Recommended energy and intensity values of alpha particles from radioactive decay", *Atomic Data and Nuclear Data Tables* 47(2), pp. 205–239, 1991.

[110]   F. G. Kondev et al., "Interplay between octupole and quasiparticle excitations in ^{178}Hg and ^{180}Hg", *Phys. Rev. C* 62(4), p. 12, 2000.

[111]   J E Gaiser, "Charmonium Spectroscopy From Radiative Decays of the J/ψ and ψ'", Thesis, Aug. 1982.

[112]   J. P. Husson, C. F. Liang, and C. Richard-serre, "One-line γ ray spectroscopic investigation of the ^{180}Hg decay chain", *Le J. De Phys.* 38, pp. 2–6, 1977.

[113]   V. Manea et al., "Penning-trap mass spectrometry and mean-field study of nuclear shape coexistence in the neutron-deficient lead region", *Phys. Rev. C* 95(5) 2017.

[114]   Yu A. Litvinov et al., "Mass measurement of cooled neutron-deficient bismuth projectile fragments with time-resolved Schottky mass spectrometry at the FRS-ESR facility", *Nucl. Phys. A* 756(1-2), pp. 3–38, 2005.

[115] T. Kibédi et al., "Evaluation of theoretical conversion coefficients using BrIcc", *Nucl. Instrum. Meth. A* 589(2), pp. 202–229, 2008.

[116] S. Agostinelli et al., "Geant4 - a simulation toolkit", *Nucl. Instrum. Meth. A* 506(3), pp. 250 –303, 2003.

[117] J. Allison et al., "Recent developments in Geant4", *Nucl. Instrum. Meth. A* 835, pp. 186 –225, 2016.

[118] F.P. Hessberger et al., "Influence of energy summing of α-particles and conversion electrons on the shapes of α-spectra in the region of the heaviest nuclei", *Nucl. Instrum. Meth. A* 274(3), pp. 522 –527, 1989.

[119] J. Elseviers et al., "Shape coexistence in ^{180}Hg studied through the β decay of ^{180}Tl", *Phys. Rev. C* 84(3), pp. 1–8, 2011.

[120] J. G. Cubiss et al., "α -decay branching ratio of ^{180}Pt", *Phys. Rev. C* 101(1), pp. 1–4, 2020.

[121] BNL, "Evaluated Nuclear Structure Data File Search and Retrieval", *NNDC*, pp. –, 2019.

[122] A. Siivola, "Alpha-Active Iridium Isotopes", *Nucl. Phys. A* 92, pp. 476–480, 1967.

[123] U. Bosch et al., "The decay of the isotopes ^{176}Ir and ^{177}Ir", *Z. Phys. A* 366, pp. 359–360, 1990.

[124] P. M. Davidson et al., "Non-yrast states and shape co-existence in light Pt Isotopes", *Nucl. Phys. A* 657(1), pp. 219–250, 1999.

[125] M. Wang et al., "The AME2016 atomic mass evaluation (II). Tables, graphs and references", *Chin. Phys. C* 41(3), pp. 030003–1–443, 2017.

[126] K. Chrysalidis et al., "In-source laser spectroscopy of dysprosium isotopes at the ISOLDE-RILIS", *Nucl. Instrum. Meth. B* 2019.

[127] P. A. Vanden Bout et al., "Hyperfine-Structure Separations, Nuclear Magnetic Moments, and Hyperfine-Structure Anomalies of Gold-198 and Gold-199", *Phys. Rev.* 158, pp. 1078–1084, 4 1967.

[128] H. Dahmen and S. Penselin, "Measurement of the nuclear magnetic dipole moment of Au197 and hyperfine structure measurements in the ground states of Au^{197}, Ag^{107}, Ag^{109} and K^{39}", *Z Phys.* 200(4), pp. 456–466, 1967.

[129] G. Passler et al., "Quadrupole moments and nuclear shapes of neutron-deficient gold isotopes", *Nucl. Phys. A* 580(2), pp. 173 –212, 1994.

[130] F. D. Feiock and W. R. Johnson, "Atomic Susceptibilities and Shielding Factors", *Phys. Rev.* 187, pp. 39–50, 1 1969.

[131] A. Andreyev, A. Barzakh, P. Van-Duppen, et al., "β-delayed fission , laser spectroscopy and shape-coexistence studies Part II : " Delineating the island of deformation in the light gold isotopes by Part I : β-delayed fission, laser spectroscopy and shape-coexistence studies with astatine beams Section I . Results from the May ' s and October ' s 2012 campaigns and the goals of this Addendum", *CERN-P-319-ADD* 1, pp. 1–6, 2013.

[132] C. Bingham et al., "Alpha-decay rates for $^{181-186}$Au and $^{181-185}$Pt", *Phys. Rev. C* 51(1), pp. 125–135, 1995.

[133] P. G. Varmette et al., "Identification of ^{181}Hg and shape coexistence in odd-A Hg isotopes", *Phys. Lett. B* 410, pp. 103–109, 1997.

[134] G. Chen and H. Song, "Theoretical Calculation of Rotational Bands of ^{179}Pt in the Particle - Triaxial- Rotor Model", *Chin. Phys. Lett.* 22(1), p. 50, 2005.

[135] C Ekstrom and Y S Shishodia, "Hyperfine structure and nuclear magnetic moments of some neutron-deficient thallium isotopes", *Hyp. Int* 1, pp. 437–458, 1975.

[136] I. G. Lamm, "Shell model Calculations of Deformed Nuclei", *Nucl. Phys. A* 125, pp. 504–540, 1969.

[137] R. Bengtsson et al., "A systematic comparison between the Nilsson and Woods-Saxon deformed shell model potentials", *Phys. Script.* 39, pp. 196–220, 1989.

[138] G. D. Dracoulis, B. Fabricius, and R. A. Bark, "Intrinsic states and rotational bands in ^{177}Pt", *Nucl. Phys. A* 510, pp. 533–556, 1990.

[139] T. Kibédi et al., "Low-spin non-yrast states and collective excitations in ^{174}Os, ^{176}Os, ^{178}Os, ^{180}Os, ^{182}Os and ^{184}Os", *Nucl. Phys. A* 567(1), pp. 183–236, 1994.

[140] Wang H. et al., "Identification of New β-Delayed γ Rays and a Low-Spin Isomer in ^{176}Ir", *Chin. Phys. Lett.* 22(9), pp. 2211–2214, 2005.

[141] R. A. Bark et al., "Two-quasiparticle configurations, signature inversion, and the $\pi i_{13/2} \otimes \nu i_{13/2}$ band in ^{176}Ir", *Phys. Rev. C* 67, p. 014320, 1 2003.

[142] M. Kowalska, "Ground state properties of neutron-rich Mg isotopes – the " island of inversion " studied with laser and β -NMR spectroscopy", 2006.

[143] W. Gins et al., "Analysis of counting data: Development of the SATLAS Python package", *Comp. Phys. Comm.* 222, pp. 286 –294, 2018.

[144] A. Wong, R. Ida, and G. Wu, "Direct NMR detection of the "invisible" alkali metal cations tightly bound to G-quadruplex structures", *Biochem. and Biophys. Res. Comm.* 337(1), pp. 363–366, 2005.

[145] P. Šket, M. Črnugelj, and J. Plavec, "Identification of mixed di-cation forms of G-quadruplex in solution", *Nucl. Acid. Res.* 33(11), pp. 3691–3697, 2005.

[146] P. Šket and J. Plavec, "Tetramolecular DNA Quadruplexes in Solution : Insights into", *J. Am Chem. Soc.* 132(15), pp. 12724–12732, 2010.

[147] N. A. Lange, *Handbook of Chemistry.* 2005, pp. 20–29.

[148] D. J. Hucknall, *Vacuum Technology and Applications*, Butterworth-Heinemann, 1991, pp. 7–17.

[149] A. Chambers, *Modern Vacuum Physics*, Chapman & Hall/CRC, 2005, p. 113.

[150] M. Bier and S. Dietrich, "Vapour pressure of ionic liquids", *Mol. Phys.* 108(2), pp. 211–214, 2010.

[151] K. N. Marsh, J. A. Boxall, and R. Lichtenthaler, "Room temperature ionic liquids and their mixtures - A review", *Fluid Phase Equilibria* 219(1), pp. 93–98, 2004.

[152] C. P. Slichter, "Electric Quadrupole Effects", *Principles of Magnetic Resonance*, Berlin, Heidelberg: Springer Berlin, 1990, pp. 485–502.

[153] G. Meier, E. Sackmann, and E. G. Grabmaier, *Applications of Liquid Crystals*, 1st ed., Grabmaier Springer Science and Business Media, 2012, pp. 21–81.

[154] Graham, A., *Annual Reports on NMR Spectroscopy*, 1st ed., Elsevier, 2006, pp. 1–53.

[155] H. H. Ginthard and J. J. Primas, *Generating of homogeneous static magnetic fields*, 1960.

[156] C. Elliott et al., "National Instruments LabVIEW: A Programming Environment for Laboratory Automation and Measurement", *J. Lab. Autom.* 12(1), pp. 17–24, 2007.

[157] F. Touchard et al., "Electric quadrupole moments and isotope shifts of radioactive sodium isotopes", *Physical Review C* 25(5), pp. 2756–2770, 1982.

[158] P. Raghavan, "Table of nuclear moments", *At. Data and Nucl. Data Tables* 42, p. 189, 1989.

[159] R. D. Harding et al., "Magnetic moments of short-lived nuclei with part-per-million accuracy: Paving the way for applications of β-detected NMR in chemistry and biology", *preprint*, pp. 1–11, 2020, eprint: `arXiv:2004.02820`.

[160] A Beckmann, K D Böklen, and D Elke, "Precision measurements of the nuclear magnetic dipole moments of ^{6}Li, ^{7}Li, ^{23}Na, ^{39}K and ^{41}K", *Z Phys.* 270(3), pp. 173–186, 1974.

[161] R. K. Harris et al., "NMR Nomenclature. Nuclear Spin Properties and Conventions for Chemical Shifts", *Pure Appl. Chem.* 73(11), pp. 1795–1818, 2001.

[162] *1-Ethyl-3-methylimidazolium dicyanamide, Sigma-Aldrich*, Accessed: 2019-07-30, URL: `https://www.sigmaaldrich.com/catalog/product/sial/00796?lang=en&region=GB`.

[163] L. V. Skripnikov et al., "New Nuclear Magnetic Moment of ^{209}Bi: Resolving the Bismuth Hyperfine Puzzle", *Phys. Rev. Lett.* 120(9), p. 93001, Feb. 2018.

[164] M. Venhart et al., "Shape coexistence in odd-mass Au isotopes: Determination of the excitation energy of the lowest intruder state in ^{179}Au", *Phys. Lett. Sect. B* 695(1-4), pp. 82–87, 2011.

[165] D. Verney et al., "Nuclear moments of neutron deficient iridium isotopes from laser spectroscopy", *Hyp. Int.* 127(1), pp. 79–82, 2000.

[166] J. Sauvage et al., "COMPLIS experiments: COllaboration for spectroscopy Measurements using a Pulsed Laser Ion Source", *Hyp. Int.* 129(1), pp. 303–317, 2000.

[167] J. Ballof et al., "The upgraded ISOLDE yield database – A new tool to predict beam intensities", *Nucl. Instrum. Meth. B (submitted)*, pp. 1–6, 2019.

[168] Y. Hirayama et al., "Study of ^{11}Be structure through β-delayed decays from polarized ^{11}Li", *Phys. Lett. B* 611(3), pp. 239 –247, 2005.

[169] M Madurga et al., "Commissioning of a beta-decay spectroscopy station at VITO", *Lett. of Int.* Pp. 1–9, 2017.